

AD-A254 349



(2)

PL-TR-92-2086

ANALYSIS AND MODELING OF THE CRRES SATELLITE DATA

J. N. Bass
C. A. Hein
C. E. Jordan
R. P. Vancour

Radex, Inc.
Three Preston Court
Bedford, MA 01730

March 20, 1992

DTIC
SELECTED
JUL 30 1992
SBD

Scientific Report No. 10

Approved for public release; distribution unlimited



PHILLIPS LABORATORY
AIR FORCE SYSTEMS COMMAND
HANSOM AIR FORCE BASE, MASSACHUSETTS 01731-5000

92 7 28 047

92-20404



"This technical report has been reviewed and is approved for publication"

Edward C. Robinson
EDWARD C. ROBINSON
Contract Manager
Data Analysis Division

Robert E. McInerney
ROBERT E. MCINERNEY, Director
Data Analysis Division

This report has been reviewed by the ESD Public Affairs Office (PA) and is
ebleasable to the National Technical Information Service (NTIS).

Qualified requestors may obtain additional copies from the Defense Technical
Information Center. All others should apply to the National Technical
Information Service.

If your address has changed, or if you wish to be removed from the mailing
list, or if the addressee is no longer employed by your organization, please
notify GL/IMA, Hanscom AFB, MA 01731. This will assist us in maintaining a
current mailing list.

Do not return copies of this report unless contractual obligations or
notices on a specific document requires that it be returned.

REPORT DOCUMENTATION PAGE

**Form Approved
OMB No. 0704-0188**

Public reporting burden for this collection of information is estimated to average 1 hour per response, including the time for reviewing instructions, searching existing data sources, gathering and maintaining the data needed, and completing and reviewing the collection of information. Send comments regarding this burden estimate or any other aspect of this collection of information, including suggestions for reducing this burden, to Washington Headquarters Services, Directorate for Information Operations and Reports, 1215 Jefferson Davis Highway, Suite 1204, Arlington, VA 22202-4302, and to the Office of Management and Budget, Paperwork Reduction Project (0704-0188), Washington, DC 20503.

1. AGENCY USE ONLY (Leave blank)			2. REPORT DATE 20 March 1992		3. REPORT TYPE AND DATES COVERED Scientific Report No. 10		
4. TITLE AND SUBTITLE Analysis and Modeling of the CRRES Satellite Data			5. FUNDING NUMBERS PE 62101F PR 7659 TA 05 WU AB Contract F19628-89-C-0068				
6. AUTHOR(S) J. N. Bass, C. A. Hein, C. E. Jordan, R. P. Vancour			8. PERFORMING ORGANIZATION REPORT NUMBER RXR-92031				
7. PERFORMING ORGANIZATION NAME(S) AND ADDRESS(ES) RADEX, Inc. Three Preston Court Bedford, MA 01730			10. SPONSORING / MONITORING AGENCY REPORT NUMBER PL-TR-92-2086				
9. SPONSORING / MONITORING AGENCY NAME(S) AND ADDRESS(ES) Phillips Laboratory Hanscom AFB, MA 01731-5000 Contract Manager: Edward C. Robinson/GPD							
11. SUPPLEMENTARY NOTES							
12a. DISTRIBUTION / AVAILABILITY STATEMENT Approved for Public Release Distribution Unlimited			12b. DISTRIBUTION CODE				
13. ABSTRACT (Maximum 200 words) The radiation belts consist of energetic charged particles trapped by the Earth's magnetic field which consists of an internal field and an external field. The external field dominates the non-dipole portions of the internal field at and above geosynchronous altitude. External field modeling usually begins with models of the various current systems from which the field is derived. CRRES data provides for a generation of new models of the radiation belts. A Strawman proposal was developed for the CRRES static radiation belt model Product Associated Data Base. Several groups of models were studied in preparation for working with the CRRES data. The models and software to run them constitute a suite of routines divided into five categories. A B_{MIN} survey data base was constructed to study the effects of magnetic latitude and local time at B_{MIN} . The behavior of the PROTEL instrument on CRRES was modeled in its hostile environment to evaluate its performance. Predictions of the developed Contamination Code compared very well with the results from the Harvard Cyclotron experiments. The CRRES Dosimeters were modeled for an isotropic, a mirror plane and the $\sin^N \alpha$ pitch angle distributions.							
14. SUBJECT TERMS Radiation belt models, Magnetic field models, Magnetospheric dynamics, Energetic particles, CRRES satellite					15. NUMBER OF PAGES 110		
					16. PRICE CODE		
17. SECURITY CLASSIFICATION OF REPORT Unclassified		18. SECURITY CLASSIFICATION OF THIS PAGE Unclassified		19. SECURITY CLASSIFICATION OF ABSTRACT Unclassified		20. LIMITATION OF ABSTRACT Unlimited	

TABLE OF CONTENTS

<u>Section</u>	<u>Page</u>
1.0 STATIC RADIATION BELT MODELING STUDIES	1
1.1 Modeling in the Near-Geosynchronous Region	1
1.1.1 General Considerations	1
1.1.1.1 Model Overview	2
1.1.1.2 Model L Values and Drift Orbits	4
1.1.1.3 Third Adiabatic Invariant	6
1.1.2 Magnetic Field Model Selection	11
1.1.2.1 Strawman Models	11
1.1.2.2 Existing Models	18
1.1.2.2.1 Constant B Equatorial Contours	18
1.1.2.2.2 Polar Cap Equatorial Projections	18
1.1.3 Dosage Calculations	18
1.2 Product-associated Data Base Design	24
1.2.1 Strawman Proposal	24
1.2.1.1 Spatial Binning	24
1.2.1.2 Sorting Geographic Bins into L Bins	25
1.2.1.3 Pitch Angle Binning	25
1.2.1.4 Format	26
1.2.2 L vs Pitch Angle	26
1.3 Software	28
1.3.1 Software Library	28
1.3.2 Other Developments	45
1.3.2.1 Conversion of Observed Pitch Angles to Equatorial	45
1.3.2.1.1 Subroutine BFLDSM	46
1.3.2.1.2 CRRES Coordinate Transformation Software Library	49
1.3.2.2 L vs Pitch Angle for Ephemeris	50
1.3.2.3 Adiabatic Invariants and Dipole-Equivalent Invariants	50
1.3.2.3.1 Equivalent Parameters	52
1.3.2.3.2 Software	52
1.4 References	55
2.0 DYNAMIC MAGNETIC FIELD MODELS	57
2.1 Models Published Before 1989	57
2.1.1 Model Derivation and Description	58
2.1.1.1 Olson-Pfizer Tilt Dependent Model	58
2.1.1.1.1 Model Derivation	59
2.1.1.2 Olson-Pfizer Dynamic Model	59
2.1.1.3 Mead-Fairfield Model	60

Table of Contents (cont'd)

<u>Section</u>		<u>Page</u>
2.1.1.4	Tsyganenko-Usmanov and Tsyganenko Models	60
2.1.1.4.1	Ring Current Model	61
2.1.1.4.2	Tail Current Models	61
2.1.1.4.3	Magnetopause Current Models	61
2.1.1.4.4	Model Derivation	62
2.1.1.5	Stern Parabolic Magnetopause-Stretched Magnetopause Model	62
2.1.1.5.1	Model Derivation	62
2.1.2	Computation Times	63
2.1.3	L Parameter Comparisons	63
2.1.4	Models vs Data	66
2.1.4.1	Comparisons of Models with SCATHA Data	71
2.1.4.2	Midnight Equatorial Field Strength Depression	75
2.1.5	Summary	77
2.2	Models Published in 1989 or Later	78
2.2.1	Tsyganenko 1989 Model	78
2.2.2	Hilmer-Voigt Model	78
2.3	References	81
3.0	EPHEMERIS STUDIES	84
3.1	Magnetic Latitude and Local Time at Bmin	84
3.2	B/B ₀ vs L and Magnetic Latitude	87
4.0	INSTRUMENT MODELING	90
4.1	PROTEL Contamination Code	90
4.1.1	Motivation	90
4.1.2	Methodology	91
4.1.2.1	Physical Assumptions	91
4.1.2.2	Janni Range-Energy Tables	91
4.1.2.3	Ray Tracing of PROTEL HEH	91
4.1.2.4	Monte Carlo Technique	92
4.1.3	Results	92
4.1.3.1	Harvard Accelerator Experiment	92
4.1.3.2	Contamination Counts	95
4.2	Dosimeter	95
4.2.1	Motivation	95
4.2.2	Methodology	96
4.2.2.1	Physical Assumptions	97
4.2.2.2	Path Length Distribution Computations	98
4.2.3	Results	100
4.3	References	102

List of Figures

<u>Figure</u>	<u>Page</u>
1. Baseline magnetosphere model overview	3
2. Differences between equatorial L-shell value computed for various models and the dipole L-shell value L_d	5
3. Equatorial traces of drift shells of particles crossing the midnight equator of $6.6 R_E$, with pitch angles 40° and 90°	7
4. Third invariant	8
5. Measured SCATHA proton distributions	10
6. Comparison of measured and Mead-TU model magnetic field magnitudes for SCATHA satellite, 20 April 1979	13
7. Schulz-McNab source-surface model	14
8. Same as Figure 6, except for Schulz-TU model instead of Mead-TU model	15
9. Field line configuration for Mead-TU model in noon-midnight meridian	16
10. Same as Figure 9, except for Schulz-TU model	17
11. Equatorial constant B contours for 40° pitch angle particles as determined from the Hilmers-Voigt model	19
12. Flux predicted for the CRRES HEEF 2.0 to 2.5 MeV electron channel based on the NASA model AE8MAX, along with the measured data, before the March 1991 storm	20
13. Flux predicted for the CRRES HEEF 2.0 to 2.5 MeV electron channel based on the NASA model AE8MAX, along with the measured data, after the March storm	21
14. This shows the dose calculated at the center of the LoLet Dome 1 electrons summed over 10 orbits at a time	23
15. Deviation of L along internal field model lines of force	27
16. Deviation of L along a magnetic field line of force crossing the midnight equator at $1.5 R_E$	29
17. Same as Figure 16, except for $2 R_E$	30
18. Same as Figure 16, except for $3 R_E$	31
19. Same as Figure 16, except for $4 R_E$	32
20. Same as Figure 16, except for $5 R_E$	33
21. Same as Figure 16, except for $6 R_E$	34
22. Same as Figure 16, except for $7 R_E$	35
23. Same as Figure 16, except at noon instead of midnight	36
24. Same as Figure 17, except at noon instead of midnight	37
25. Same as Figure 18, except at noon instead of midnight	38
26. Same as Figure 19, except at noon instead of midnight	39
27. Same as Figure 20, except at noon instead of midnight	40
28. Same as Figure 21, except at noon instead of midnight	41
29. Same as Figure 22, except at noon instead of midnight	42
30. Predicted CRRES orbital parameters	43
31. Magnetic field line passing through a given vector location r and crossing the Equator at r_e	47
32. Overview of software for computation of adiabatic invariants and dipole equivalent invariants	53

List of Figures (cont'd)

<u>Figure</u>	<u>Page</u>
33. Contours of constant $\Delta L = L - L_d$: internal magnetic field; $L_d = 3.2, 3.7, 4.2$, and 4.7	64
34. Same as Figure 33, but for $L_d = 5.2, 5.7, 6.2$, and 6.7	65
35. Same as Figure 33, but for internal model + Olson-Pfizer tilt dependent external model	67
36. Same as Figure 35, but for $L_d = 5.2, 5.7, 6.2$, and 6.7	68
37. Noon and midnight equatorial ΔL profiles for $K_p = 0$	69
38. Same as Figure 37, but for $20^\circ N$ magnetic latitude	70
39. Measured - model differences: 20 April 1979	72
40. Noon magnetopause standoff distance: 20 April 1979	73
41. Same as Figure 39, but for 21 April 1979	74
42. Averaged measured and model midnight equatorial magnetic field depression	76
43. Sample of a preliminary comparison of these models to CRRES data	79
44. The angle between the CRRES magnetometer measured field vectors and the model field vectors for part of 26 August 1990	80
45. Solar magnetic (SM) local time and orbit number for all cases of BMIN distance greater than $7 R_E$, orbits 1 - 450	85
46. SM latitude and radial distance for all cases of BMIN distance greater than $6 R_E$, orbits 1 - 450	86
47. CRRES B/B_0 vs. Dwell Chart - 1 Year Statistics	88
48. CRRES B/B_0 vs. Solar Magnetic Latitude at $L = 2.5$ (Orbits 1-510)	89
49. PROTEL HEH Response Function for the isotropic case for channel 10	93
50. Response Function for Mirror Plane Case, for two orientations of the mirror plane with respect to the PROTEL electron deflection magnet	94
51. Detector Geometry	98
52. Path Length Distribution for Detector 1 for $\lambda = 60$ degrees compared with Infinite Slab Path Length Distribution (smooth curve)	100
53. Path Length Distribution for Detector 4, $\lambda = 60$ degrees	101

List of Tables

<u>Table</u>	<u>Page</u>
1. Sample of the model dose tables produced for the CRRES SpaceRad dosimeter	22
2. External Magnetic Field Models	57
3. Vax 8650 Computation Times (sec/10000 calls)	63
4. Average Values for the Olson-Pfizer Dynamic Model	75
5. Fraction of PROTEL HEH Counts Due to Contamination	95
6. Physical and Geometric Parameters of the CRRES Dosimeter Detectors	97
7. Notation	97

ACKNOWLEDGEMENTS

The work described in this report required the involvement and guidance of a number of individuals at PL, and their interest and encouragement is gratefully acknowledged.

Sue Gussenhoven and Gary Mullen of the Space Particle Environment Branch have been involved throughout the projects, and provided essential support and the opportunity for many challenging studies.

Ed Robinson of PL/GPD both initiated and coordinated the activities as Contract Monitor. We also deeply appreciate the invaluable help and continuing interest of Bob McInerney, Director, Data Analysis Division.

Howard Singer of the Plasma Fields and Waves Branch provided magnetometer data. Robert Hilmer of Rice University, Space Physics and Astronomy Dept., Karl Pfister of McDonnell Douglas Corp., Space Systems Division and David Stern of NASA Goddard Space Flight Center have contributed model codes and revisions as necessary. Bob Filz of the Space Particle Environment Branch gave useful suggestions and assistance for development of the Protel contamination code and Dosimeter modeling software. We have also benefitted from helpful discussions with many other unnamed participants in the CRRES program.

DTIC QUALITY INSPECTED

Accession For	
NTIS CRA&I	<input checked="" type="checkbox"/>
DTIC TAB	<input type="checkbox"/>
Unannounced	<input type="checkbox"/>
Justification	
By _____	
Distribution/ _____	
Availability Codes	
Dist	Avail and/or Special
A-1	

1.0 STATIC RADIATION BELT MODELING STUDIES

1.1 Modeling in the Near-Geosynchronous Region

The radiation belts consists of energetic particles trapped by the Earth's magnetic field, which is the sum of two parts: that which we will call the "internal" magnetic field because it is due to sources (currents) in the Earth's interior, and that which we will call the "external" magnetic field because it is due to sources outside the Earth's surface. Existing radiation belt models incorporate only the internal field, consisting of a dominant dipole with higher order multipoles. However the significance of the external field increases with altitude. As we shall see, the external field dominates the non-dipole portions of the internal field at and above geosynchronous altitude. The external field introduces a significant noon-midnight asymmetry not present in the internal field. This results in noon-midnight asymmetries in the particle populations, notably in their pitch angle distributions. Local time dependent pitch angle distributions have been reported by *West* [1979] and *Mullen and Gussenhoven* [1983]. In addition, the external field contains a dependence on the time-varying tilt of the Earth's magnetic dipole toward the Earth-Sun line. Therefore, even in magnetically quiet times the total magnetic field is not truly static.

Models based on the internal field alone generally are adequate for engineering purposes, such as the study of radiation damage on a satellite. This is because the largest radiation dosage is at low altitudes where the internal field dominates. However, models based on the total (internal + external) field would be useful for scientific understanding of magnetospheric dynamics, and for the in-situ detection of substorms. The diffuse auroral zone in the ionosphere maps magnetically to the near-geosynchronous region at the equator. The two regions are coupled by region 2 field aligned currents. *Vasyliunas* [1970] derived a representation of the field aligned currents in isotropic plasma in terms of the equatorial plasma pressure gradient and magnetic field geometry. *Heinemann* [1990] has generalized this to anisotropic plasma. *Mullen and Gussenhoven* [1983] have observed that 20-400 kev ions contribute a substantial fraction to the total pressure in the near-geosynchronous region. *Baker, et. al.* [1978] and *Bass, et. al.* [1989] have observed variations in electron pitch angle distributions associated with substorm growth phase and onset. Model quiet pitch angle distributions might, therefore, provide a useful baseline against which to compare observed pitch angle distributions to detect and predict, in real time, the occurrence of substorms.

1.1.1 General Considerations

Following an overview of possible model construction and usage, we compare the L values computed from (internal + external) field models with values computed from an internal field model alone. This will illustrate the points made above concerning the significance of the external field above geosynchronous altitudes, the noon-midnight asymmetry it introduces, and its tilt dependence. It will be seen that the internal field can be truncated to the quadrupole terms. Then we investigate the dependence of the third adiabatic invariant on mirror point L, mirror point B, and the dipole tilt. If the dependence on dipole tilt is negligible, the particle model may be accurately defined with the energy and mirror point L and B as independent variables. Finally, we summarize the simplifications we conclude are justified in this modeling.

1.1.1.1 Model Overview

Figure 1 shows an overview of possible model construction and use. We neglect any non-inductive electric field and assume that the time variations in the magnetic field are sufficiently slow to insure constancy of the three adiabatic invariants:

$$\begin{aligned}\mu &= \frac{p^2}{2mB} \sin^2\alpha = \frac{p^2}{2mB_m} \\ J &= 2pI \\ \Phi &= \int \mathbf{B} \cdot d\mathbf{A}\end{aligned}\tag{1}$$

Here μ (magnetic moment), J , and Φ are the first, second, and third adiabatic invariants, respectively. The momentum of the particle is p , its mass is m , and its initial pitch angle is α . In the bounce motion of the particle's drift guiding center along a field line, B_m is the magnetic field magnitude at the mirror points, where the pitch angle is 90° . From constancy of the first adiabatic invariant, this is given by:

$$B_m = \frac{B}{\sin^2\alpha}\tag{2}$$

I is the integral of the bounce motion between the mirror points:

$$I = \int_A^{A'} \sqrt{1 - \frac{B}{B_m}} ds\tag{3}$$

where A and A' are the mirror points and ds is an element of length along the field line. The mirror point McIlwain L value L_m is a function of B_m and I , as specified by *McIlwain* [1961]. Its dependence on the pitch angle follows from the dependence of L on the mirror points in a non-dipole field. In the third adiabatic invariant Φ , the integral is over any surface enclosed by the drift shell of field lines containing the instantaneous locus of mirror points of common I and B_m (or L_m and B_m).

In a purely static field, with no electric field, the energy and, therefore, the momentum p are constants of the motion. Therefore, it follows that the mirror point magnetic field B_m , the bounce integral I , and the mirror point L value L_m are also constants. The drift shell, defined by I and B_m (or L_m and B_m), is fixed in time. From this, it follows that constancy of the third adiabatic invariant is not an independent condition. Thus, it seems convenient to select energy, L_m and B_m as the independent variables of the model. In this case, the third box in our figure may be eliminated, and the variables μ , J and Φ replaced by the variables L_m , B_m and E in subsequent boxes.

BASELINE MAGNETOSPHERE MODEL OVERVIEW

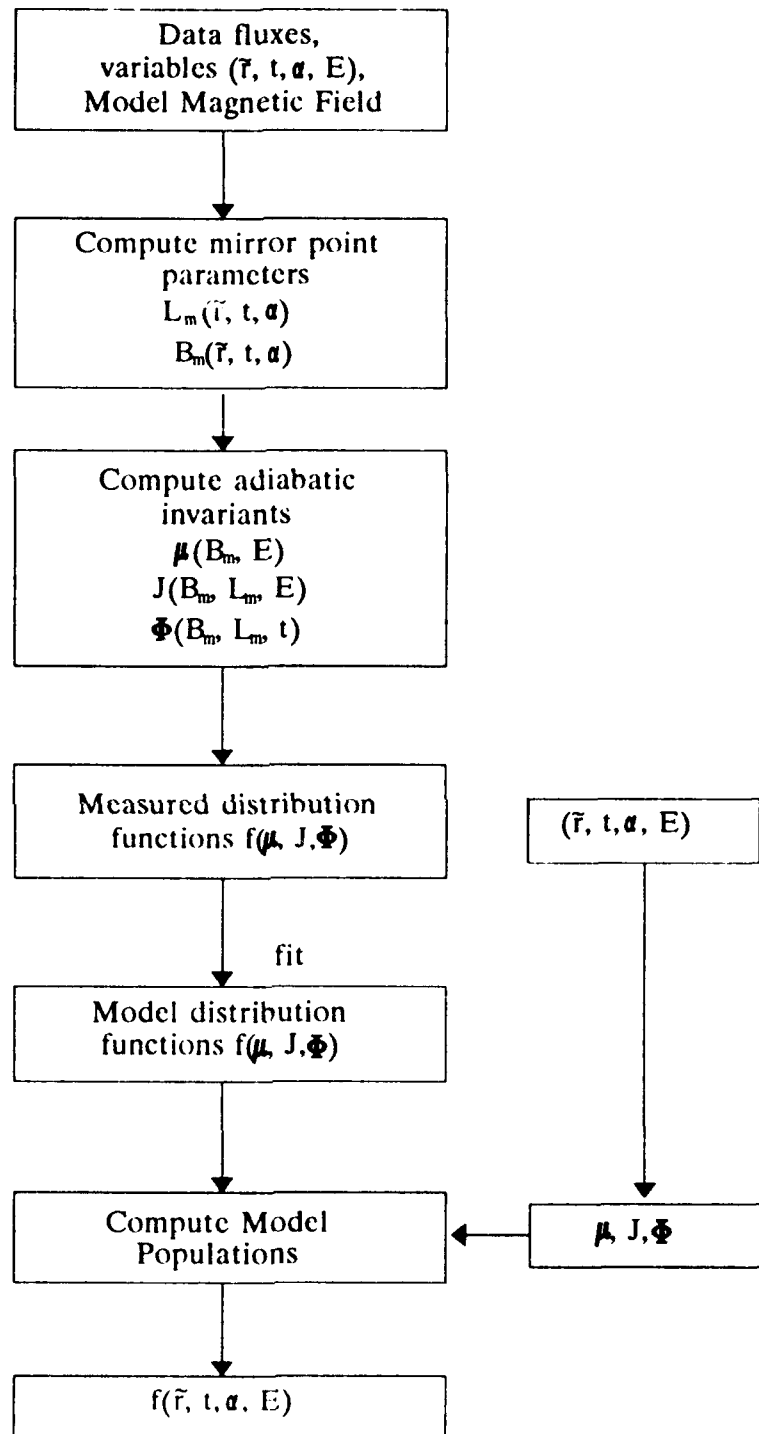


Figure 1. Baseline magnetosphere model overview

In a time varying field, the third invariant in general depends on time as well as on the mirror point parameters of the drift orbit. Therefore, it is necessary to change these mirror point parameters in order to preserve the constancy of the third invariant. This, in turn, requires a change of the particle's momentum and energy to preserve the first two adiabatic invariants. Physically, the particles are responding to an induction electric field due to the time derivative of the magnetic flux enclosed by the drift shell. However, if the dependence of the third invariant were sufficiently "small", these effects may be neglected: the third invariant would be approximately constant for fixed mirror point parameters, allowing these and the energy to remain constants. Physically, the variation of the particle's energy due to time variations in the magnetic field would be negligible.

If the time variation is periodic, as is the case for the dipole tilt, we may evaluate its maximum effect. This may then be compared with other sources of error, for instance, measurement error and magnetic field model-to-model differences.

1.1.1.2 Model L Values and Drift Orbits

Figure 2 illustrates, for four magnetic field models, the difference ΔL between the L value computed with the model and that computed with a pure dipole model. These are plotted vs L_d , the pure dipole L . Each model is the sum of the IGRF 1985 internal field model and the indicated external field model, except for the model designated "No Ext.", which is the IGRF 1985 alone. The external models used in the other three cases are the Tsyganenko 1989 model [Tsyganenko, 1989], the Hilmer-Voigt model [Hilmer, 1989], and the quiet Olson-Pfizer model [Olson and Pfizer, 1977]. The results are given at the equator for " $K_p = 0$ ". Actually, only the Tsyganenko model contains explicit K_p dependence. The Hilmer-Voigt model is the "super-quiet" case, while the Olson-Pfizer model is known to be accurate for quiet conditions. The IGRF 1985 model itself contains neither explicit nor implicit dependence on magnetic activity. The dipole reference L_d was computed assuming that the dipole is at the center of the Earth. In this case L_d is the distance in R_E from the center of the Earth. In all of the plots, the sun's magnetic longitude is 0° .

The IGRF 1985 results (solid lines) indicate the contribution of the non-dipole terms of the internal field to L . This is clearly smaller than the contributions due to the external field. The IGRF 1985 ΔL is nearly constant over the range shown, indicating that the contribution is dominated by the quadrupole terms. This follows from the fact that the contribution due to the n th degree internal terms should be:

$$\Delta L_n = L_d \left(\frac{\Delta L_n}{L_d} \right) \propto L_d (L_d^{-(n-1)}) = L_d^{2-n} \quad (4)$$

The proportionality follows from the fact that the strength of the n th degree contribution to the magnetic field varies with distance as r^{-n-2} . Thus, contribution of any multipole term relative to the dipole ($n=1$) should be proportional to $L_d^{-(n-1)}$. If, instead of the center of the Earth, we used the position of the offset (eccentric) dipole [Chapman and Bartels, 1940] as the coordinate origin, ΔL for the internal field would be less than 0.01 R_E for the entire range of the plots.

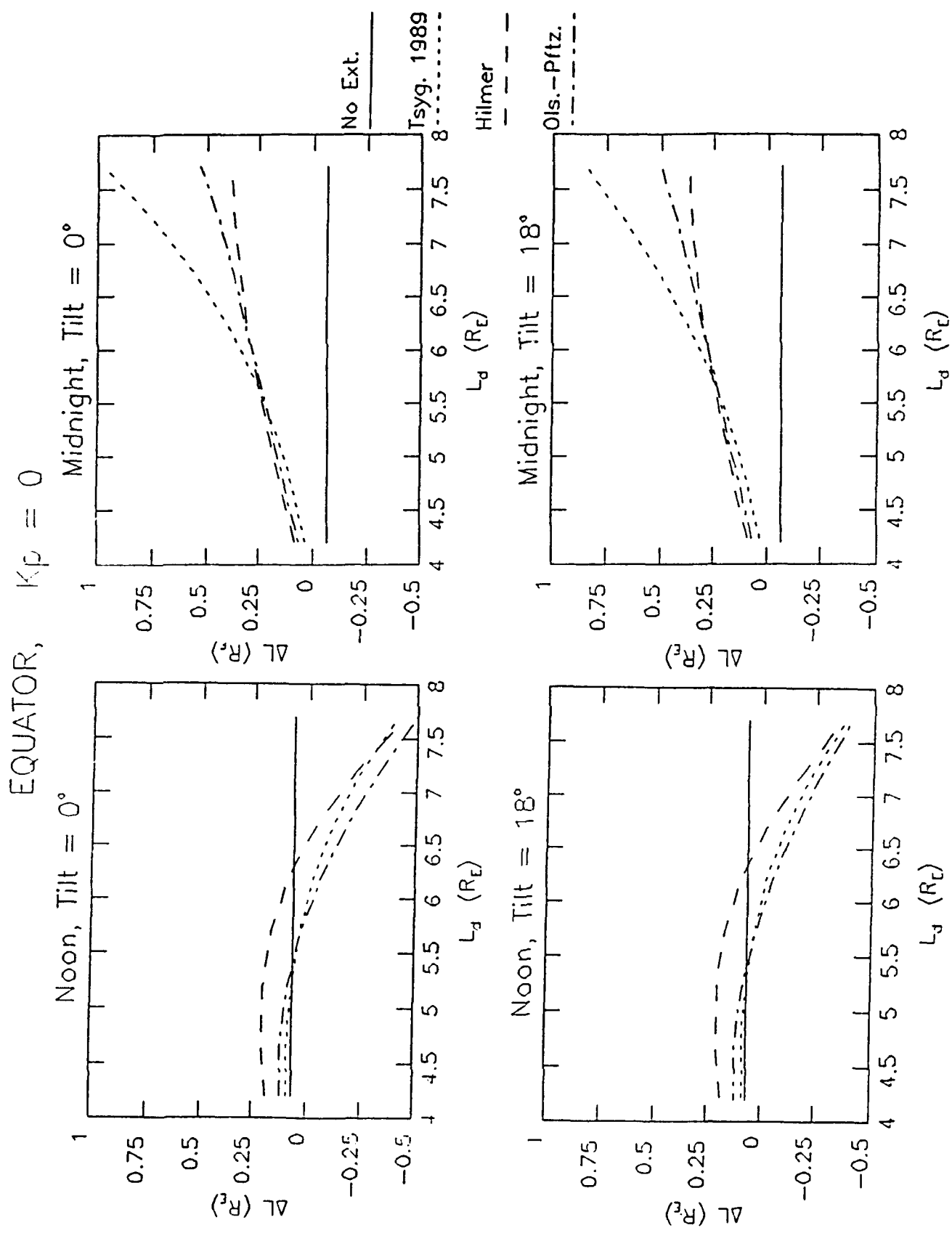


Figure 2. Differences between equatorial L-shell value computed for various models and the dipole L-shell value L_d .

Figure 3 shows a comparison of the equatorial crossings of the drift shells for particles with 90° and 40° equatorial pitch angles at geosynchronous altitude (6.6 R_E) at local midnight. We see that the particles which separate at local times other than midnight (drift shell splitting), for the equatorial crossing of the 40°, is nearly circular.

1.1.1.3 Third Adiabatic Invariant

If, for given values of a drift orbit's mirror point parameters, the third adiabatic invariant is independent of time, constancy of the mirror point parameters follows from constancy of the adiabatic invariants. Although the time-varying dipole tilt rules out strict time independence, the variations introduced may be sufficiently small that constant mirror point parameters may still be assumed. Therefore, it is useful to study the tilt-dependence of the third invariant.

Figure 4 shows, on the left hand panel, the L dependence of the third invariant for a particle with zero second adiabatic invariant (90° equatorial pitch angle) for the dipole field, and for the dipole + Tsyganenko 1989 magnetic field model at the lowest K_p level. In the case here of zero second adiabatic invariant:

$$B_m (I=0) = \frac{M}{L_m^3} \quad (5)$$

where M is the Earth's dipole moment. In the present case, M was derived from the IGRF 85 internal field model, updated to 1990. The right-hand panel of the figure shows dipole tilt dependence of the third invariant for L = 5, 6, 7 and 8 (for zero second invariant) as a percent difference from the value at zero tilt. These are plotted over the range of allowable positive tilt values (the figure for negative tilt would be the mirror image).

The left-hand panel shows that the external field contributes a nearly constant negative offset. This is due to the nature of the ΔB contribution of the external field to the total field. At small distances, inside all the drift shells plotted here, ΔB is large and negative at all local times. At larger distances, where the drift orbits are located, ΔB is much smaller in magnitude and becomes positive on the dayside as we approach the magnetopause, while remaining negative in the nightside tail. The large negative ΔB region is inside the orbits plotted here, making the same contribution to the flux enclosed by all of them. In the region where the orbits lie, ΔB is smaller in magnitude than the region inside, with some tendency toward cancellation of the day and night portions. Thus, the third invariant for these orbits is dominated by the contributions from their common inner region. The right-hand panel shows that the maximum variation magnitude due to tilt is ~2.5 %, at the maximum tilt. The variation increases with L except for a reversal between L=7 and L=8.

To gauge the impact of the dependence of the third invariant on dipole tilt, we look at two aspects: the dependence of a particle's L and energy on tilt that is required to preserve its adiabatic invariants, and the resulting tilt dependence of fluxes at fixed energy and L. From the theory of small perturbations:

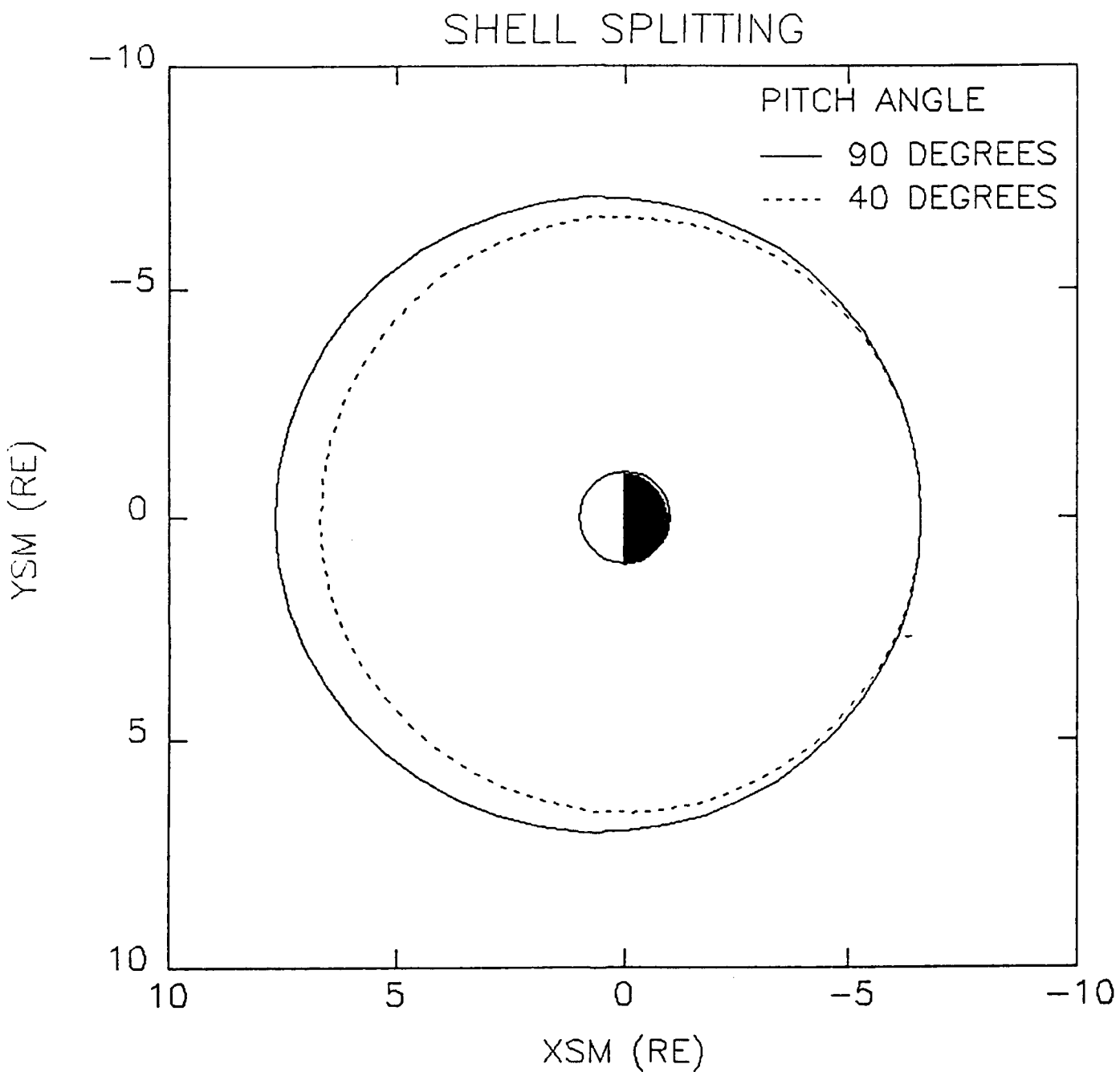


Figure 3. Equatorial traces of drift shells of particles crossing the midnight equator of $6.6 R_E$, with pitch angles 40° and 90° .

THIRD INVARIANT - DIPOLE + TSYGANENKO 1989

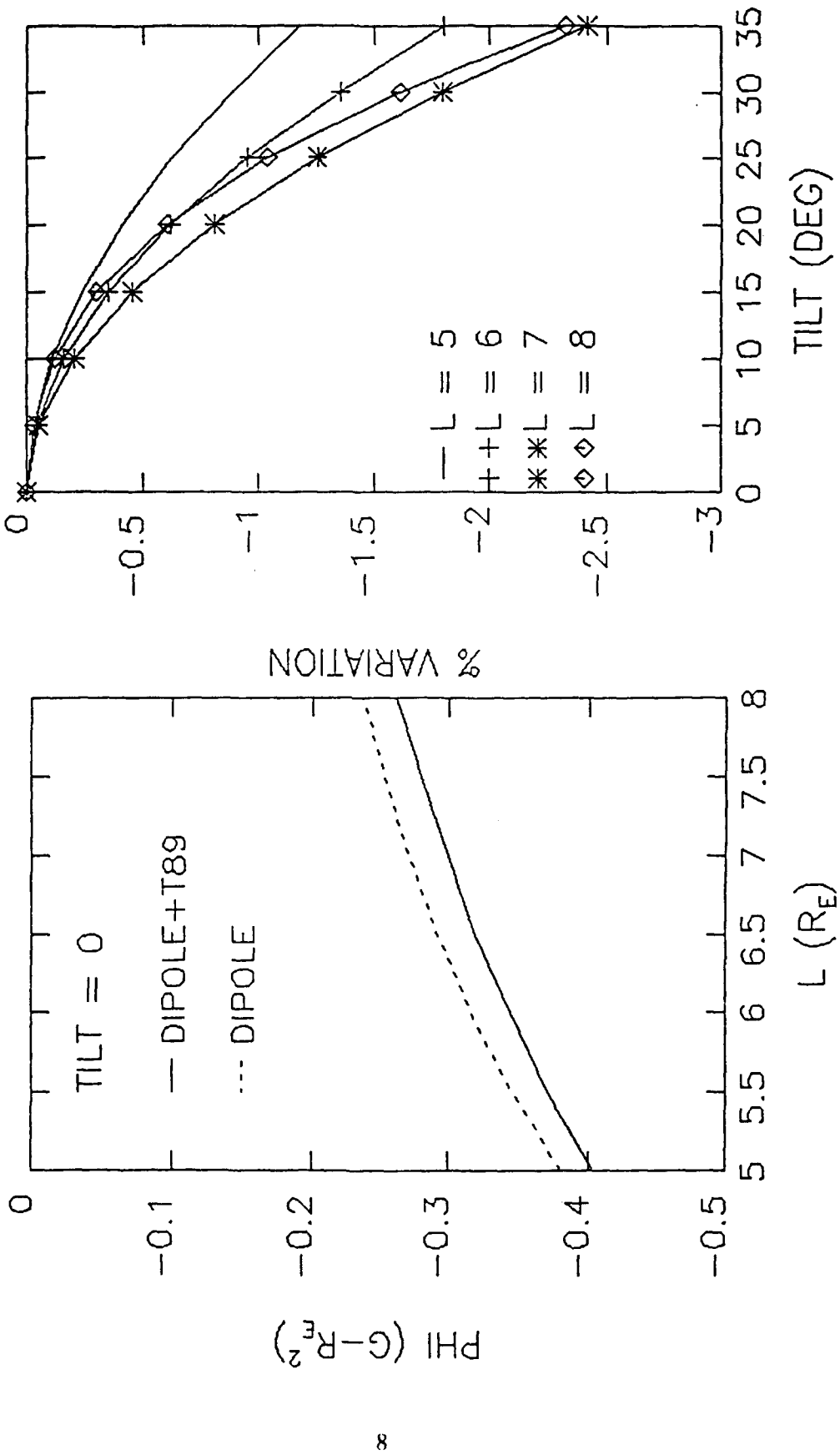


Figure 4. Third invariant. Left panel: comparison of dipole plus Tsyganenko 1989 model with dipole for zero tilt. Right panel: percent difference from zero tilt value for dipole plus Tsyganenko 1989 model.

$$\frac{\Delta L}{L} \approx - \left[\frac{\partial \ln |\Phi|}{\partial \ln L} \right]^{-1} \frac{\Delta \Phi}{\Phi} \approx \frac{\Delta \Phi}{\Phi} \quad (6)$$

$$\frac{\Delta E}{E} \approx \frac{\Delta B}{B} \approx \frac{3\Delta L}{L} \quad (7)$$

Equation (6) describes the adjustment in L that a particle must make to compensate for a change in the third adiabatic invariant at fixed L. The second approximate equality follows from the approximation that the partial is -1, as for a dipole, which seems justified by the left-hand panel of Figure 4. Equation (7) follows from the conservation of the first adiabatic invariant (non-relativistic particles), and the relationship (Equation (5)) between B and L for zero second invariant.

Given the maximum percent variation of the third invariant with tilt, ~2.5 %, we find that the maximum L adjustment of a particle is ~2.5 %, and the maximum energy adjustment is ~7.5%. The L adjustment is within the model-to-model differences indicated in Figure 2. The energy adjustment is within typical energy widths of the SCATHA particle detectors ,~100 % [Hanser, et. al., 1979], but exceeds those of some of the CRRES detectors [Gussenhoven, et. al., 1985].

Using the Liouville Theorem, we estimate the variation in the particle distribution function value at fixed E and L as:

$$\frac{\Delta f}{f} = - \frac{\partial \ln f}{\partial L} L \Delta \ln L - \frac{\partial \ln f}{\partial \ln E} \Delta \ln E \quad (8)$$

To get some feel of the partials of the distribution function f, we examined 1 MeV protons observed by the SCATHA SCS instrument on 20 April 1979. The left-hand panel of Figure 5 shows the observed (symbols) L dependence of the 1 MeV particle fluxes. They fit well the expression (solid line)

$$f=0.045 e^{-2.84(L-5)} \quad (9)$$

At L=7, the energy dependence of the proton population (right-hand panel, Figure 5) fits well the expression:

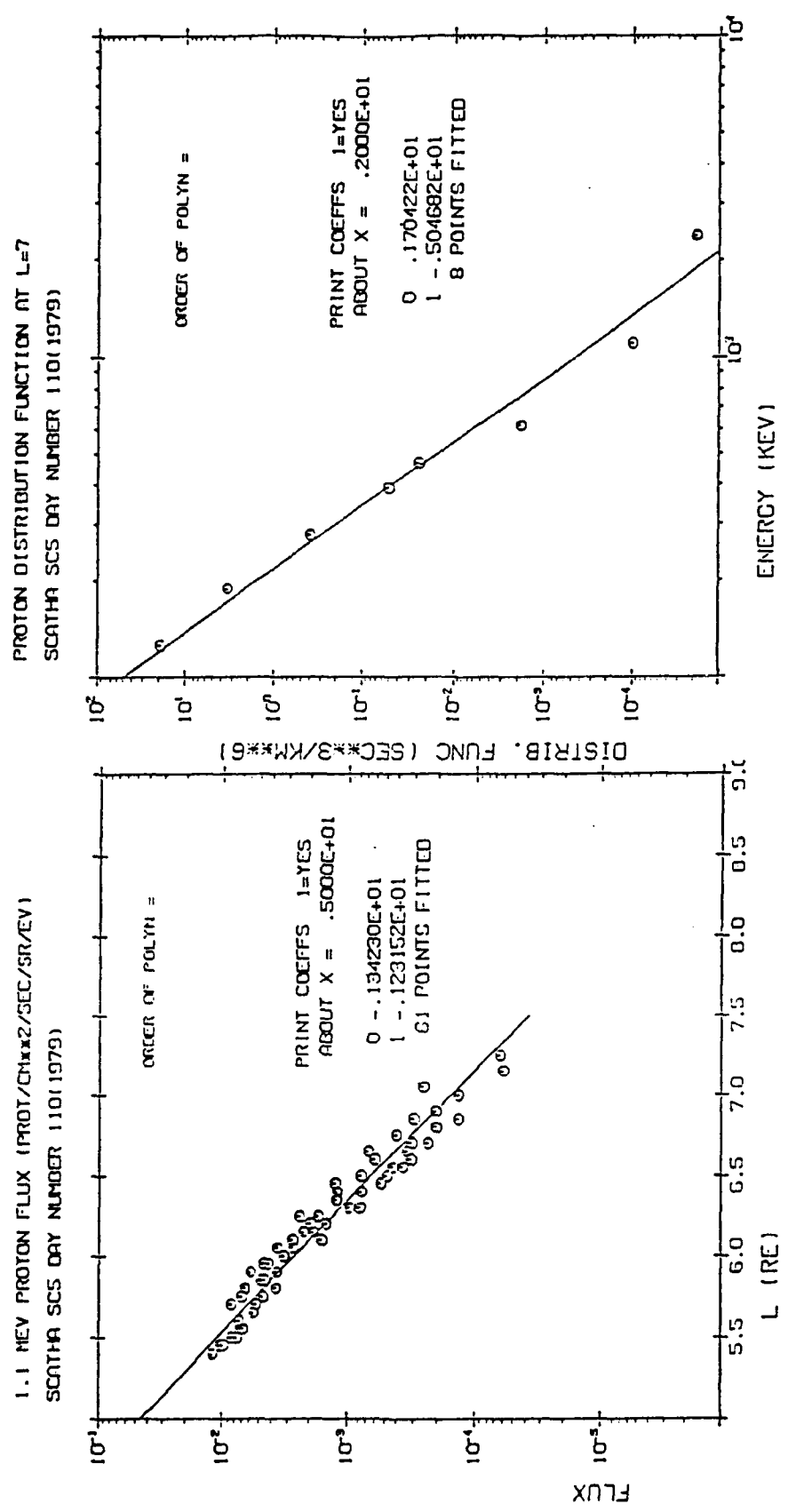


Figure 5. Measured SCATHA proton distributions. Left panel: radial distribution at $L = 7$. Right panel: energy distribution at 1.1 MeV.

$$f = 0.02 \left[\frac{E}{100 \text{ keV}} \right]^{-5.047} \quad (10)$$

Plugging these results into Equation (8), we find the maximum variation in particle fluxes at fixed L and E due to dipole tilt variation is ~11 %.

1.1.2 Magnetic Field Model Selection

1.1.2.1 Strawman Models

Modeling of the near-geosynchronous region has been attempted previously employing a Mead-type magnetic model (defined by only two coefficients) adjusted to best fit the measured magnetic field for the period in question [*RADEX, Inc.*, 1989]. This model has the advantage that the adiabatic invariants can be computed from simple analytic expressions. The calculations were based on the Pennington-Stern formulation, applicable to a field expressed as the gradient of a scalar potential, which itself is expressed as an expansion in internal and external spherical harmonics. The results are accurate through first order in the coefficients. Since the chosen model is independent of dipole tilt and other time-varying dynamic parameters, it is a truly static model. In this case, the third adiabatic invariant is strictly a function of the first two; therefore, we need be concerned only with conservation of the first two adiabatic invariants.

A major problem with this form of model is that it fails to account properly for the decay of the ring current portion of the field with distance, since the azimuthally symmetric part of the field in this model is spatially constant. Another possible problem with the original model is the lack of dependence on the dipole tilt relative to the Earth-Sun line. Although, as we have discussed previously, the third adiabatic invariant depends only moderately on the tilt at given values of the first two invariants, it is still necessary to represent the tilt variation in the field for accurate determination of the first two invariants. A third problem with the original model is that the internal part of the field includes only a dipole. We found in our magnetic field model studies, that the higher order terms produce a radially independent contribution to L which is in excess of $0.1 R_E$ in the region of the South Atlantic Anomaly. The Earth's rotation produces a small time variation which could impact the third invariant.

A model proposed here will hopefully remove these difficulties while retaining some of the simplifications of the Mead model. The first modification is that the ring current would be represented by a Tsyganenko form which is simple, analytic, azimuthally symmetric, and has the proper behavior at large distances. A sum of two such terms of opposite directions, a la Hilmer, could also be considered. The second modification is that the external spherical harmonics, which would continue to represent the tail and magnetopause portions of the field would contain tilt-dependent terms. These would be in the form of harmonics whose contributions to the z component of the field are antisymmetric with respect to the dipole equator. The third modification would be the addition of a quadrupole portion of the internal field. An analysis of the Pennington equations indicates that these terms produce the above-mentioned radially independent contribution to L, while higher multipoles yield contributions which vary as inverse

powers of the distance. By placing the origin at the offset dipole rather than at the Earth's center, we can eliminate some, but not all of this effect.

The calculations of the second and third adiabatic invariants may be done with the simplification, used in the earlier effort, that only first order contributions need be considered. Thus, contributions from each part of the field can be considered separately. The spherical harmonic contributions can be obtained from the Pennington-Stern theory, as before. This leaves the contribution of the ring current to the adiabatic invariants to be determined. This can be done by analytically fitting or numerically tabulating the invariants computed for a dipole + ring current field magnetic field, and subtracting the dipole portion. Both procedures are simplified by the independence of the ring current model on local time, longitude, and dipole tilt. Furthermore, if, consistent with the inclusion of first order perturbations only, we assume that the contributions are linearly proportional to the field strength parameter of the ring current, then we need only fit or tabulate the dependence on magnetic latitude, longitude, and the ring current length scale parameter.

Figure 6 shows a model constructed from a Tsyganenko-Usmanov ring current field, an internal field through the $n=2$ terms, and the two leading terms of the Mead model, for day 110 (1979). The Mead terms have been computed for the time-varying standoff distance on that day. The Tsyganenko term is for length scale parameter equal to $4 R_E$, and for magnetic field strength parameter -65 nT so that the net contribution of the Ring current and Mead magnetopause terms to the field at the Earth's surface is -40 nT when the standoff distance is $10 R_E$. Also shown are data (symbols) from the SCATHA magnetometer. There is an almost constant difference between the data and the model, with the model field consistently higher than the data. We would expect a tail field to reduce this disagreement, since it would produce a negative contribution in the inner magnetosphere.

Therefore, the source-surface model of *Schulz and McNab* [1986] has been explored. This model contains an external spherical harmonic representation of the tail and magnetopause fields which would be valid within the inner magnetospheric region S (Figure 7, originally Figure 1 of that paper). The two leading terms are identical in form to the two Mead model terms mentioned above. However, the coefficient of the symmetric term is smaller, and the coefficient of the asymmetric term is larger than the coefficients, used above, which represent only the magnetopause contribution. This results in an average decrease in the inner magnetospheric field, with a day-night asymmetry, which is exactly what one expects from a tail field. Figure 8 shows a comparison of the data with this revised model, where the ring current amplitude is readjusted to again give a total field depression of -40 nT at the Earth's surface for $10 R_E$ standoff distance. We see that there is much better agreement between this model ("Schulz-TU") and the data, than between the previous model ("Mead-TU") and the data. In Figures 9 and 10, the field line configurations are plotted for these models, for $10 R_E$ standoff distance and including the $n=2$ internal terms. Inside $10 R_E$, the Schulz-TU model looks quite reasonable. The divergence of the field lines outside this region does not correctly represent that model. A different formulation, which smoothly joins the field of the inner region S at the boundary between the two regions, is prescribed in the tail region T, as shown in Figure 7. The determination of the coefficients by Schulz and McNab was in the absence of a ring current field. Coefficients resulting from inclusion of such a field might improve the agreement with the data.

The results here are for zero dipole tilt, which is what Schulz and McNab considered. Considerations by *Stern* [1985] indicate that the field, in more general cases, may be represented by the form:

20 APRIL 1979 MAGNETIC FIELD BZ
MEAD-TU MODEL

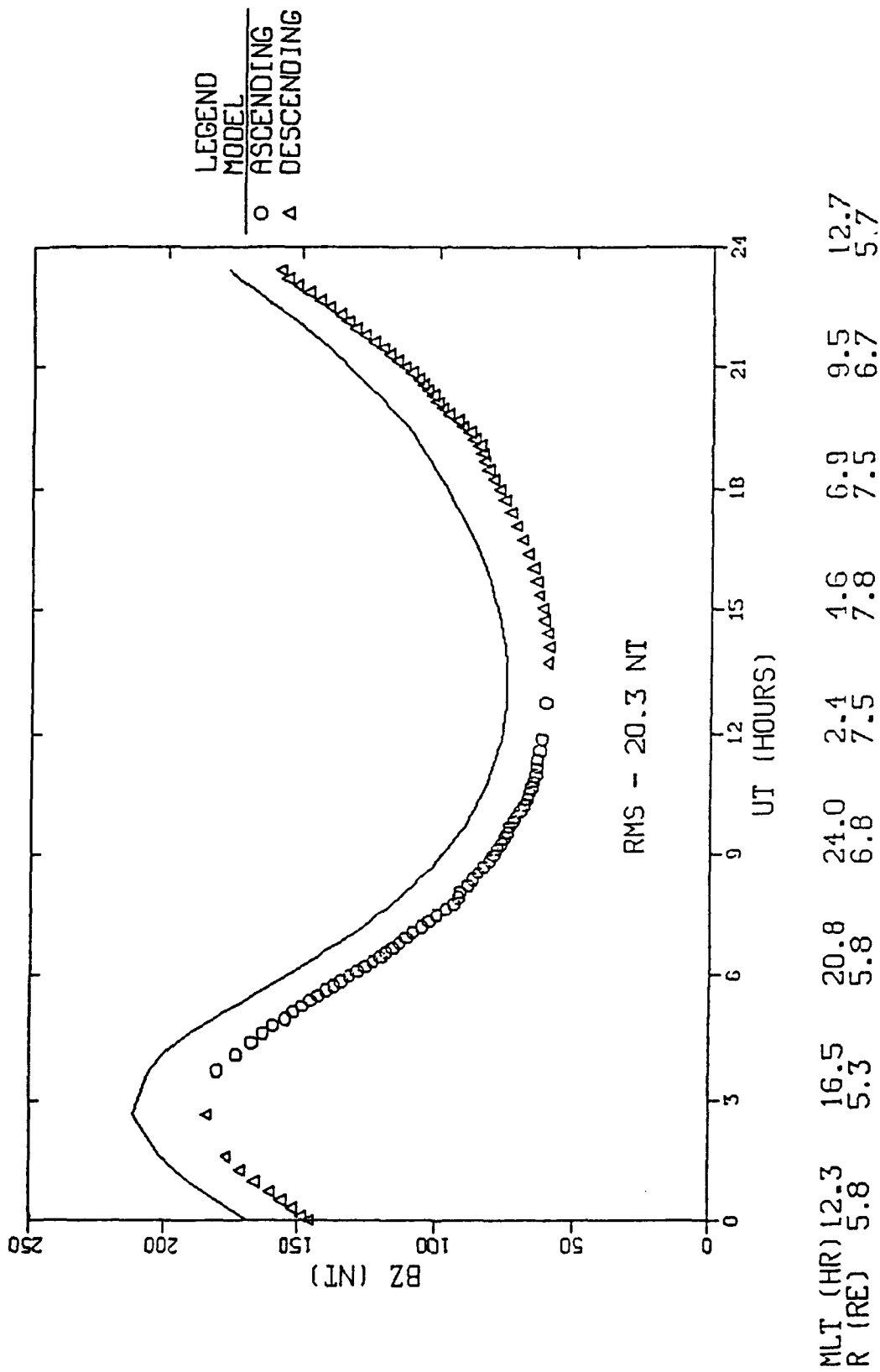


Figure 6. Comparison of measured and Mead-Tu model magnetic field magnitudes for SCATHA satellite, 20 April 1979.

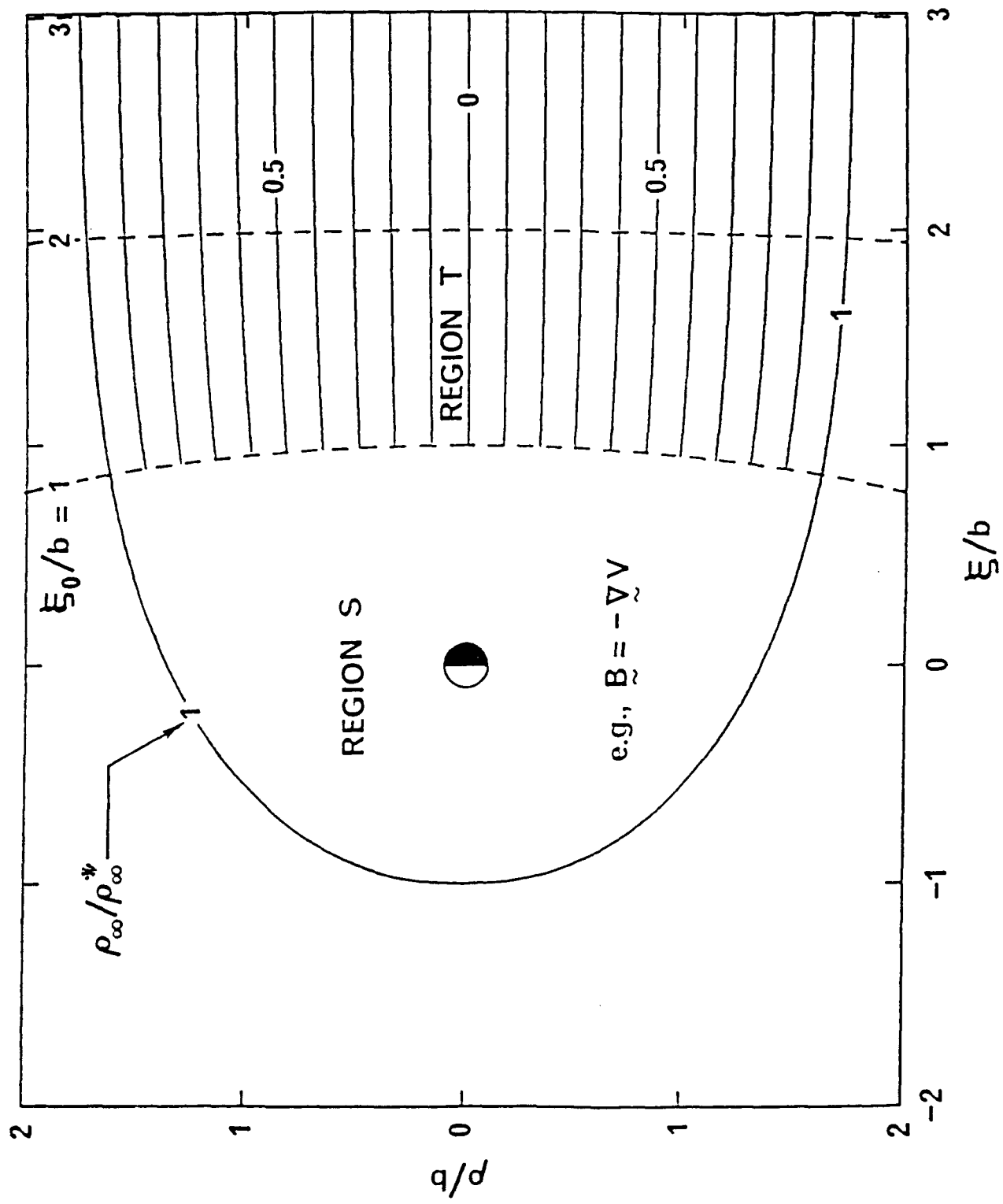


Figure 7. Schulz-McNab source-surface model (Figure 1 of Schulz and McNab [1986]).

20 APRIL 1979 MAGNETIC FIELD BZ
SCHULZ-TU MODEL

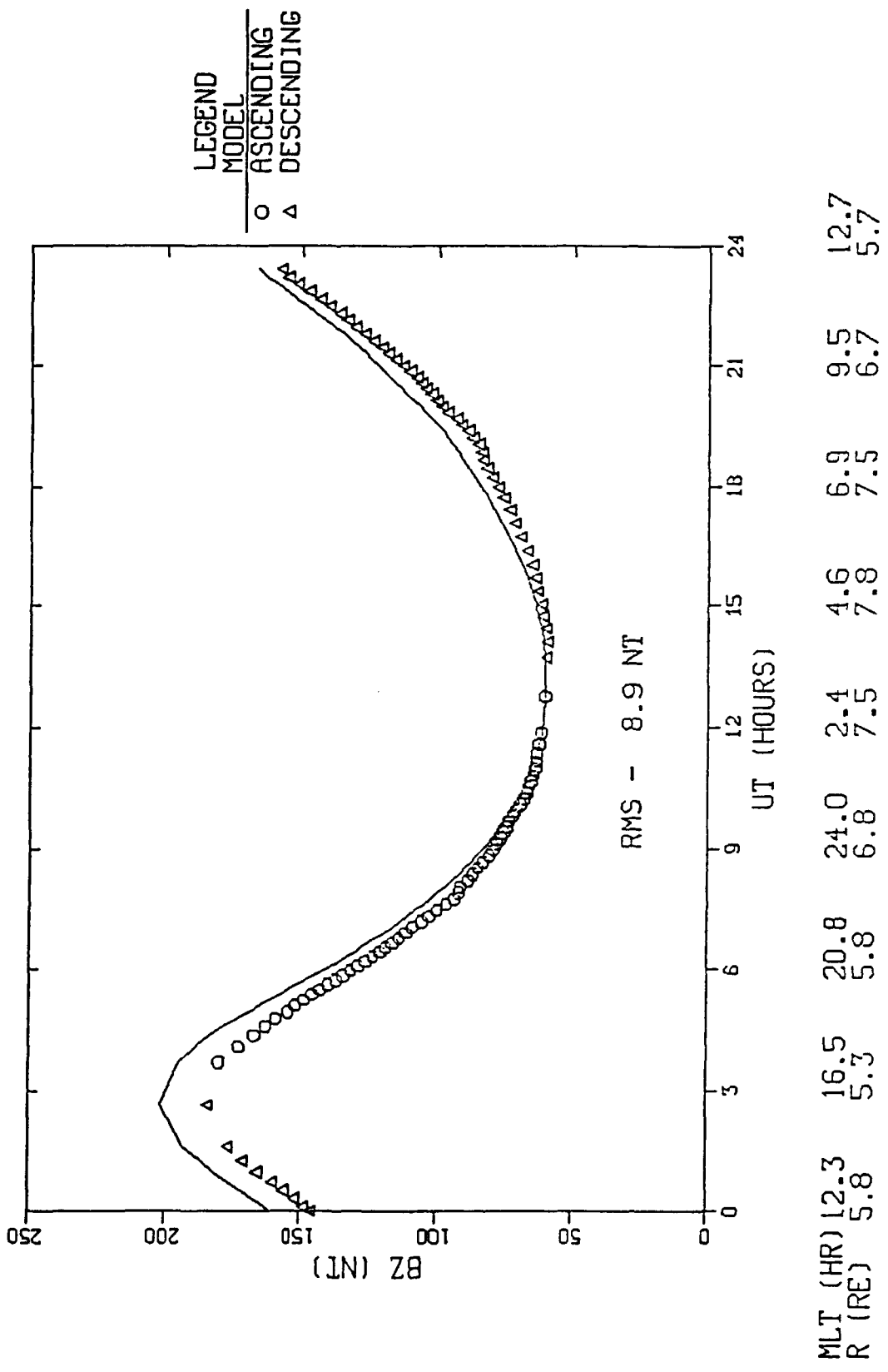


Figure 8. Same as Figure 6, except for Schulz-TU model instead of Mead-TU model.

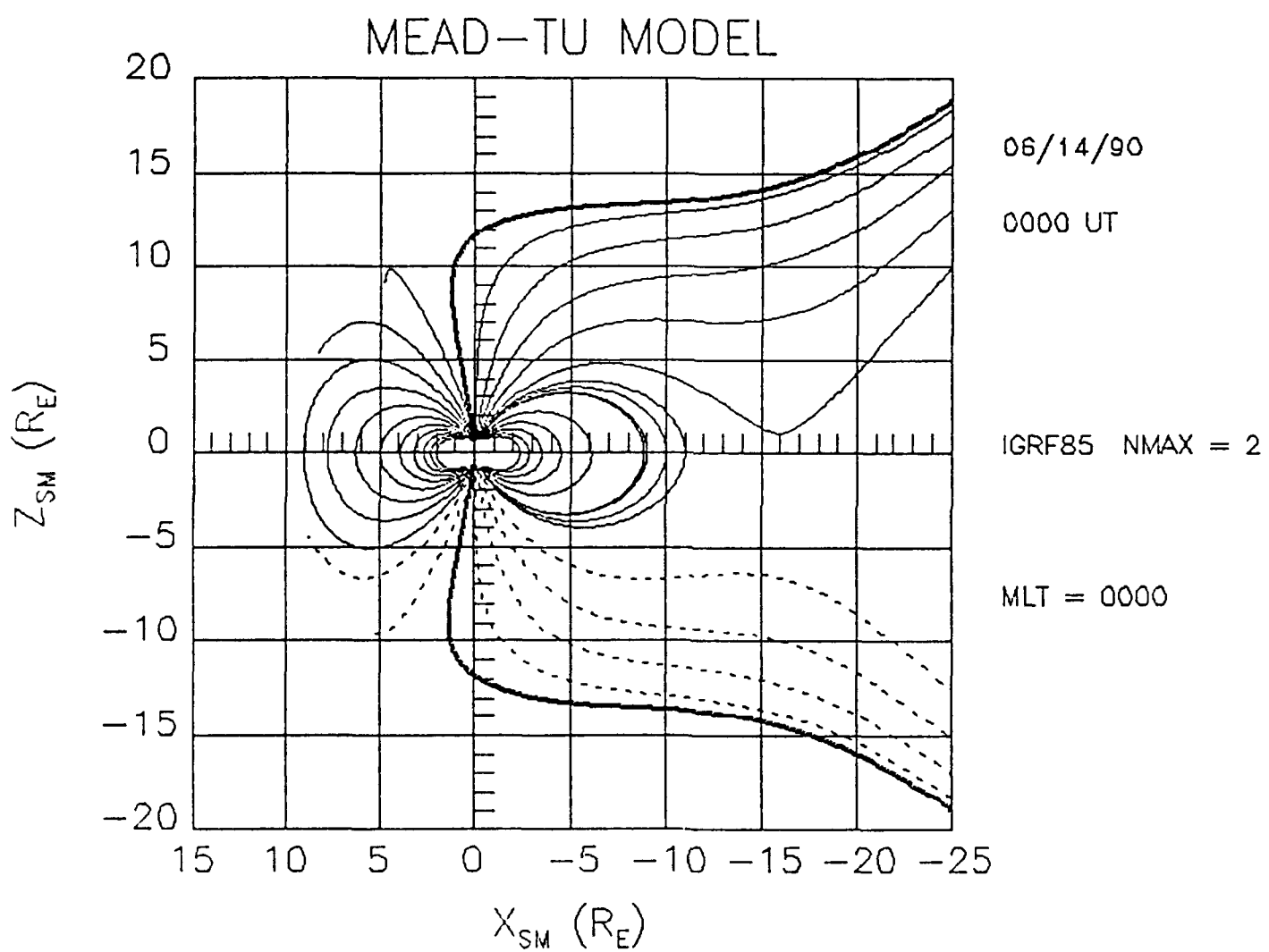


Figure 9. Field line configuration for Mead-TU model in noon-midnight meridian.

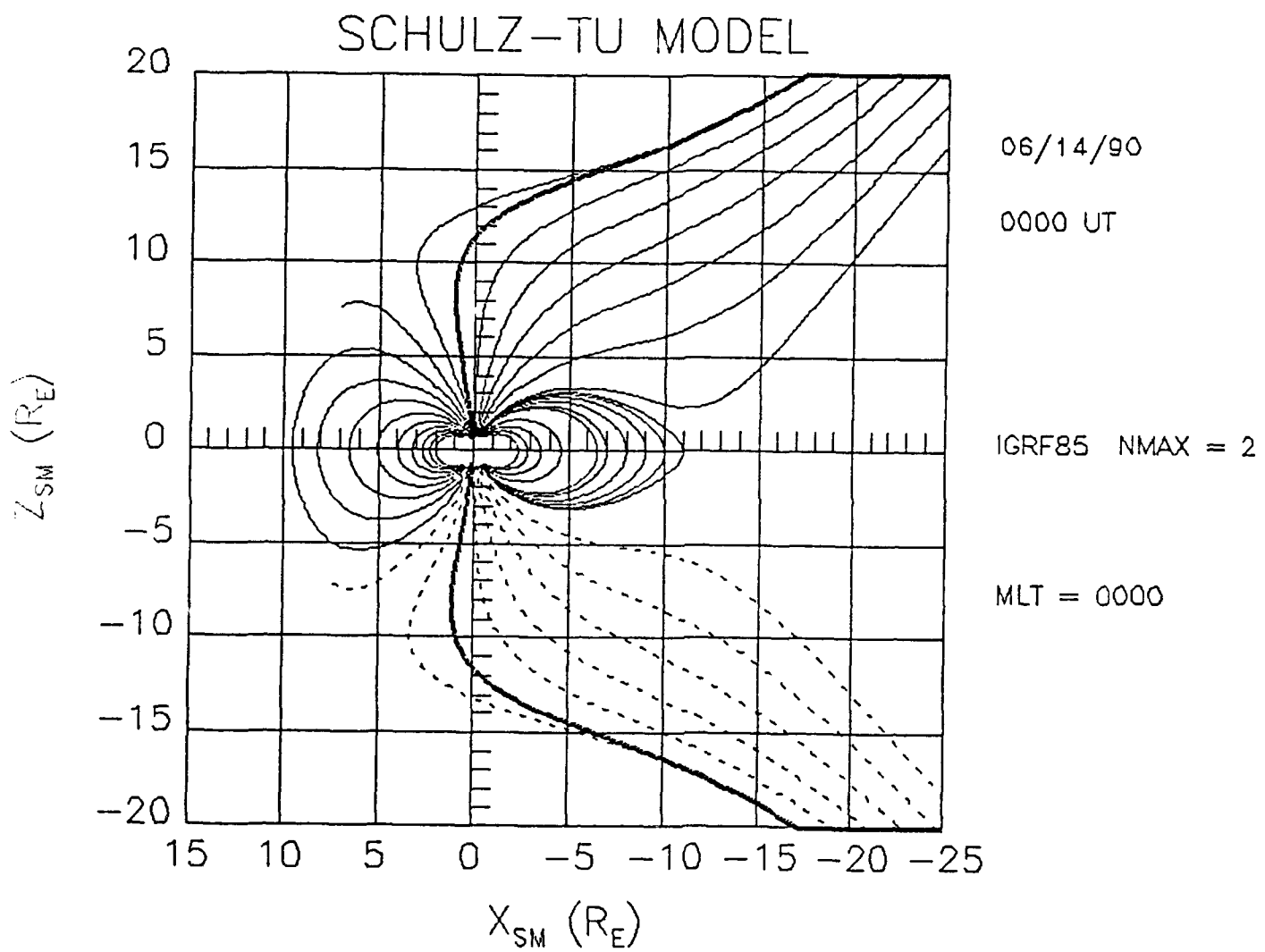


Figure 10. Same as Figure 9, except for Schulz-TU model.

$$B = B_0 \cos t + B_{90} \sin t \quad (11)$$

where t is the tilt angle, B_0 is the model obtained by Schulz and McNab for zero tilt, and B_{90} is the model they would obtain for 90° tilt. Thus, solutions would have to be obtained only for these two cases, the results of which could be superposed to produce the model for arbitrary tilt.

1.1.2.2 Existing Models

1.1.2.2.1 Constant B Equatorial Contours

In an effort to get a better handle on how to label, as well as, model the trapped particles, we needed to develop a better understanding of the correlation between particles at high latitude and low altitude with those at the equator. To this end, we made three sets of maps of constant equatorial B contours for 90°, 40° and 10°, respectively. Several different external field models were used with the IGRF 1980 internal field model, namely, Tsyganenko 1989, Hilmer-Voigt, Olson-Pfister Tilt-Dependent, Mead Asymmetric and Mead Symmetric. In addition, IGRF 1980 alone and the dipole were used for the SCATHA Day 110 (20 April 1979) scenario. Plots were produced of the B contours for each of the models (Figure 11) and for the B contours for a given model with the dipole B contours superposed.

1.1.2.2.2 Polar Cap Equatorial Projections

In addition to the equatorial constant B contours discussed above, there was also interest in mapping particles which mirror at 840 km and 100 km back to the equator and determining their constant B contours as well. The software was setup to do this (only slight modifications to the software were required from the previous work), however, no plots were ever generated. Due to other more pressing pre-launch work, this study was set aside.

1.1.3 Dosage Calculations

Before the CRRES launch, we were interested in simulating the data and creating some mock data files for several of the instruments (Figures 12 and 13), including the SpaceRad dosimeter. In order to do this, we slightly modified the Yates and Rothwell dosage code presently in use here at PL. This code takes a given orbit, computes the fluence from the NASA trapped radiation models, and then, calculates the dose deposited at the center of an aluminum sphere. We modified the default thickness and energy parameters to just include the specifications related to the dosimeter. Some prelaunch files were produced. Following the launch, we began to produce the model doses per orbit based on orbital parameters from the ephemeris files. In addition, we kept a cumulative total of each of the HiLET and LoLET channels (Table 1). Additionally, we produced plots of 10-orbit-sums of the dose (Figure 14). These tables and plots are regularly updated as new ephemeris files become available.

In addition to this regular work, two special cases for dosages were calculated. The dose/day over one week of the DMSP F7 orbit was calculated for both solar minimum and maximum conditions. Doses were also calculated using the AP8MAX model for the HiLET channels of the SpaceRad dosimeter.

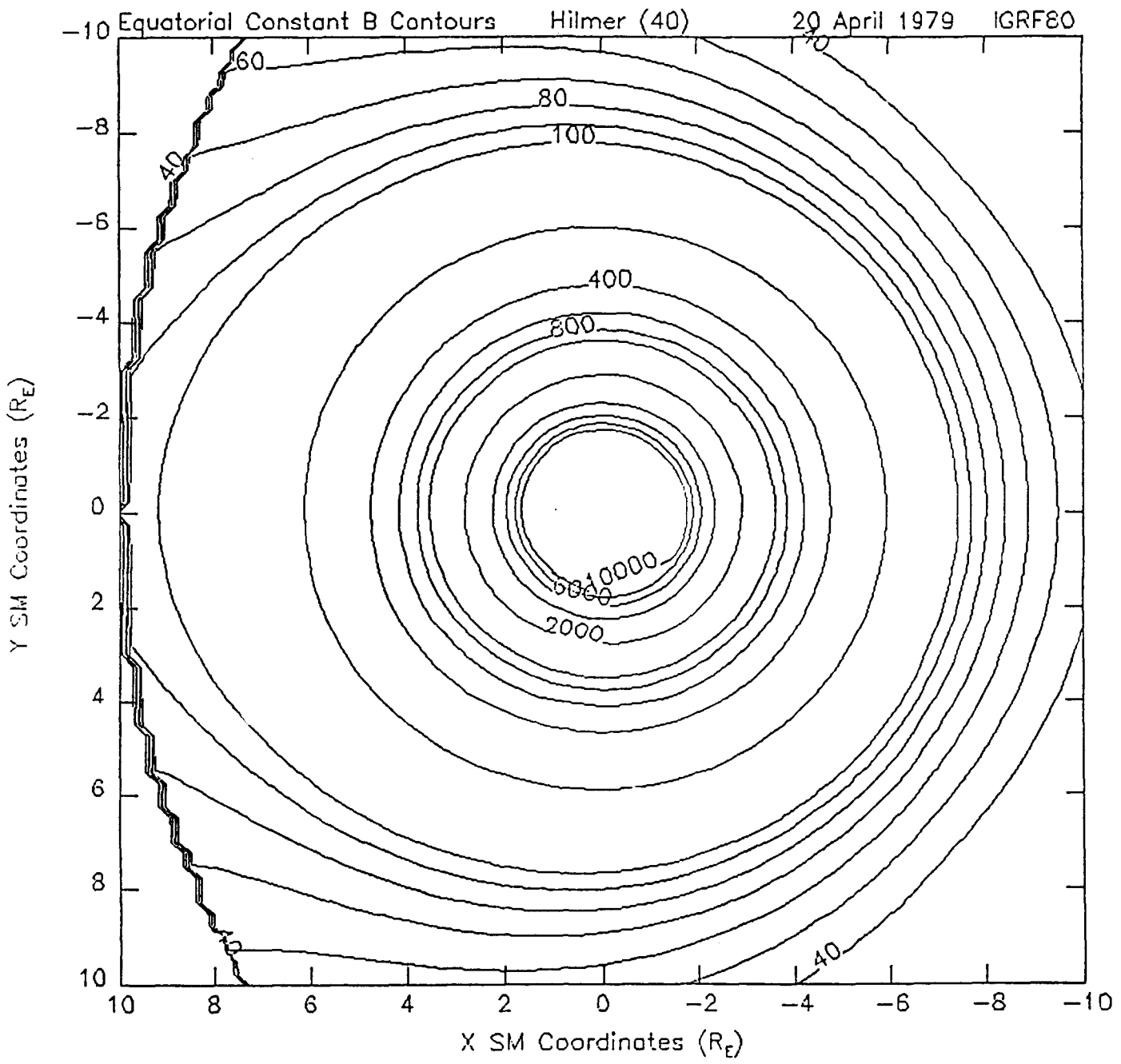


Figure 11. This shows the equatorial constant B contours for 40° pitch angle particles as determined from the Hilmer-Voigt model. The jagged edge is where the model is cut off due to the magnetopause.

2.0 to 2.5 MeV Electrons
28 July 1990

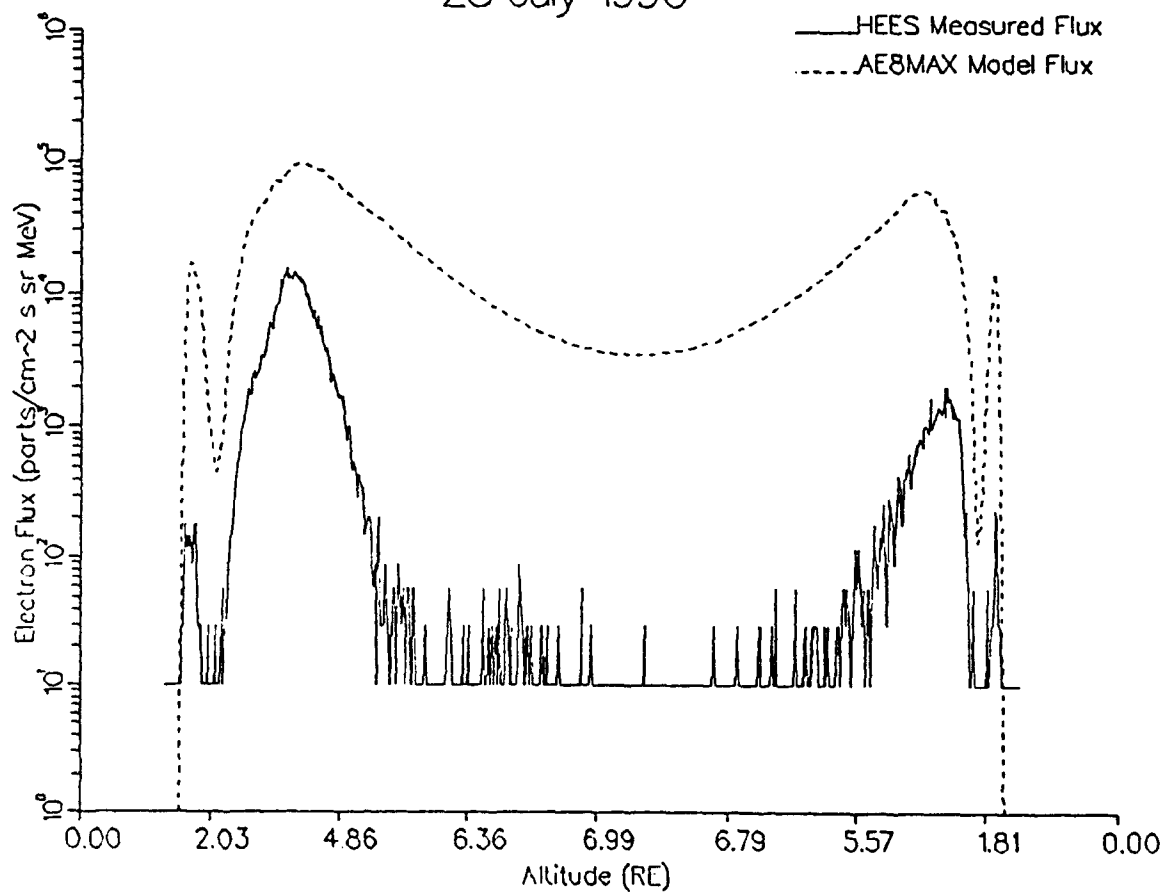


Figure 12. This figure shows the flux predicted for the CRRES HEEF 2.0 to 2.5 MeV electron channel based on the NASA model AE8MAX, along with the measured data, before the March 1991 storm. This is representative of the types of simulations which were run for various electron and proton instruments.

2.0 TO 2.5 MeV ELECTRONS
29 March 1991

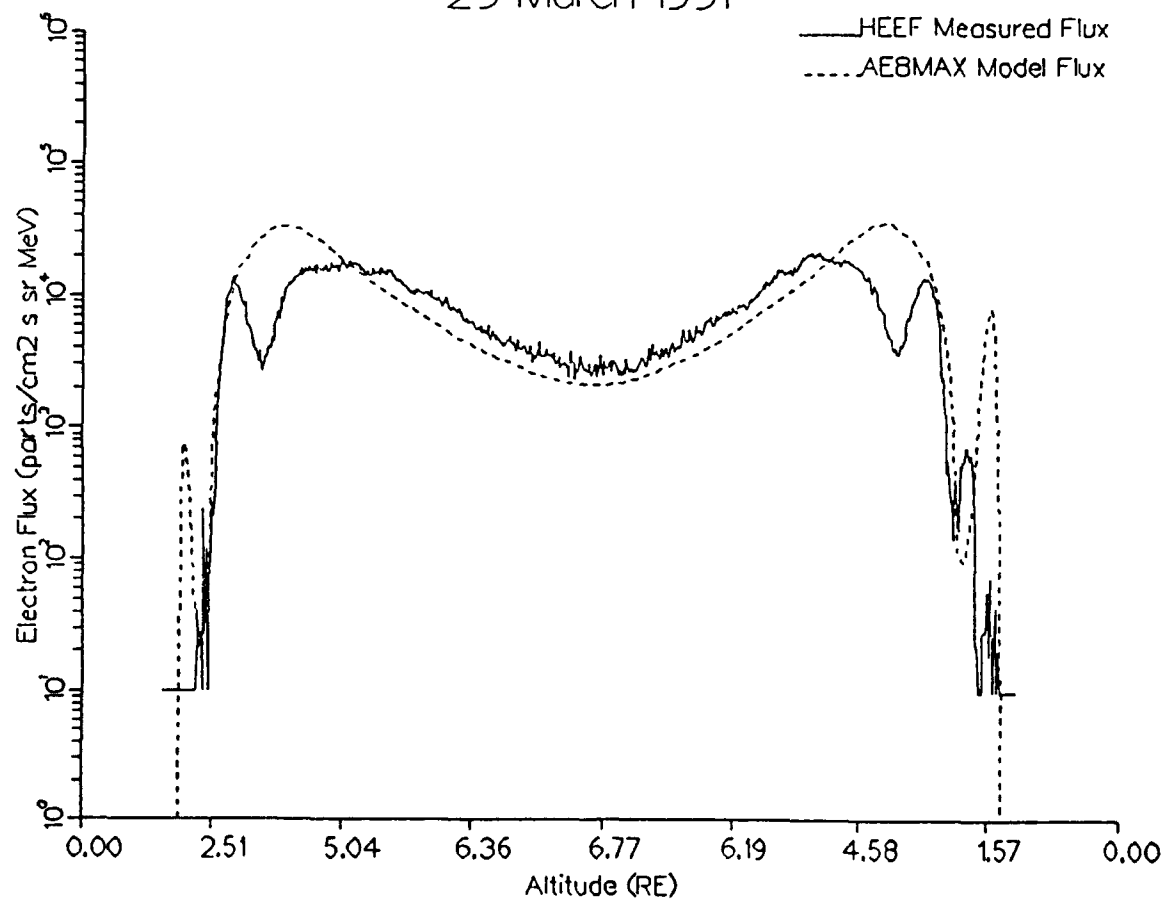


Figure 13. This figure shows the flux predicted for the CRRES HEEF 2.0 to 2.5 MeV electron channel based on the NASA model AE8MAX, along with the measured data, after the March storm. This is representative of the types of simulations which were run for various electron and proton instruments.

Table 1. This is a sample of the model dose tables produced for the CRRES SpaceRad dosimeter. The electron and proton fluences and dose for each of the HiLet and LoLet channels along with the cumulative dose through all orbits are given.

DEPTH DOSE PROFILES FOR THE DOSIMETER LOLET AND HILET CHANNELS USING AERMAX AND AP8MAC

Orbit Number	Omnidirectional Fluence (parts/cm ² sq)	Energy Range (MeV)	AL Dose Thickness (gm/cm ² sq)	Dose for Solid Sphere (Rads)	LoLet Dose	HiLet Dose	Cumulative Dose
0	5.250E+10	e	1.0- 11.25	.55	9.502E+02	9.502E+02	9.502E+02
0	5.967E+06	p	130.0-625.00	.55	3.506E-01	2.579E+01	2.611E+01
0	2.870E+09	e	2.5- 11.25	1.55	2.579E+01	2.341E-01	2.431E-01
0	5.625E+06	p	135.0-625.00	.55	3.174E-01	3.097E-01	3.077E-01
0	8.377E+06	e	5.0- 11.25	3.05	6.789E-03	6.789E-03	6.789E-03
0	5.303E+06	p	140.0-625.00	3.05	3.099E-01	2.431E-01	2.431E-01
0	4.447E+06	p	155.0-625.00	5.91	2.341E-01	1.770E+01	1.770E+01
0	5.584E+07	p	20.0-130.00	.55	1.770E+01	4.517E+00	4.517E+00
0	2.510E+07	p	35.0-134.50	1.55	4.517E+00	2.301E+00	2.301E+00
0	1.685E+07	p	51.0-140.50	3.05	2.301E+00	1.463E+00	1.463E+00
0	1.199E+07	p	75.0-155.50	5.91	1.463E+00	1.463E+00	1.463E+00
1	3.866E+10	e	1.0- 11.25	.55	7.059E+02	7.054E+02	1.666E+03
1	9.021E+06	p	130.0-625.00	.55	5.279E-01	1.935E+01	4.366E+01
1	2.115E+09	e	2.5- 11.25	1.55	1.907E+01	4.798E-01	4.798E-01
1	8.515E+06	p	135.0-625.00	1.55	4.798E-01	4.626E-01	7.703E-01
1	6.197E+06	e	5.0- 11.25	3.05	5.017E-03	4.576E-01	6.129E-01
1	8.038E+06	p	140.0-625.00	3.05	4.576E-01	3.698E-01	4.261E+01
1	6.767E+06	p	155.0-625.00	5.91	3.698E-01	2.471E+01	1.093E+01
1	8.011E+07	p	20.0-130.00	.55	2.471E+01	6.444E+00	5.644E+00
1	3.656E+07	p	35.0-134.50	1.55	6.444E+00	3.343E+00	3.544E+00
1	2.474E+07	p	51.0-140.50	3.05	3.343E+00	2.081E+00	2.081E+00
1	1.780E+07	p	75.0-155.50	5.91	2.081E+00	2.081E+00	2.081E+00
2	5.435E+10	e	1.0- 11.25	.55	9.960E+02	9.962E+02	2.662E+03
2	2.694E+06	p	130.0-625.00	.55	1.591E-01	2.757E+01	7.322E+01
2	3.029E+09	e	2.5- 11.25	1.55	2.752E+01	1.476E-01	9.144E-01
2	2.526E+06	p	135.0-625.00	1.55	1.476E-01	7.424E-03	1.441E-01
2	9.205E+06	e	5.0- 11.25	3.05	7.424E-03	1.367E-01	1.367E-01
2	2.369E+06	p	140.0-625.00	3.05	1.367E-01	1.103E-01	7.232E-01
2	1.957E+06	p	155.0-625.00	5.91	1.103E-01	8.759E+00	5.117E+01
2	2.799E+07	p	20.0-130.00	.55	8.759E+00	2.305E+00	2.305E+00
2	1.254E+07	p	35.0-134.50	1.55	2.305E+00	1.132E+00	1.132E+00
2	8.324E+06	p	51.0-140.50	3.05	1.132E+00	6.776E+00	6.776E+00
2	5.740E+06	p	75.0-155.50	5.91	6.955E-01	4.239E-01	4.239E-01
3	4.969E+10	e	1.0- 11.25	.55	9.072E+02	9.076E+02	3.570E+03
3	6.861E+06	p	130.0-625.00	.55	3.933E-01	2.471E+01	9.793E+01
3	2.702E+09	e	2.5- 11.25	1.55	2.471E+01	3.684E-01	1.270E+00
3	6.472E+06	p	135.0-625.00	1.55	3.684E-01	3.555E-01	3.555E-01
3	7.917E+06	e	5.0- 11.25	3.05	3.555E-01	3.491E-01	1.005E+00
3	6.105E+06	p	140.0-625.00	3.05	3.491E-01	2.817E-01	6.843E+01
3	5.130E+06	p	155.0-625.00	5.91	2.817E-01	1.756E+01	1.826E+01
3	5.662E+07	p	20.0-130.00	.55	1.756E+01	5.022E+00	5.671E+00
3	2.746E+07	p	35.0-134.50	1.55	5.022E+00	2.671E+00	9.447E+00
3	1.892E+07	p	51.0-140.50	3.05	2.671E+00	1.585E+00	1.585E+00
3	1.360E+07	p	75.0-155.50	5.91	1.585E+00	1.585E+00	1.585E+00

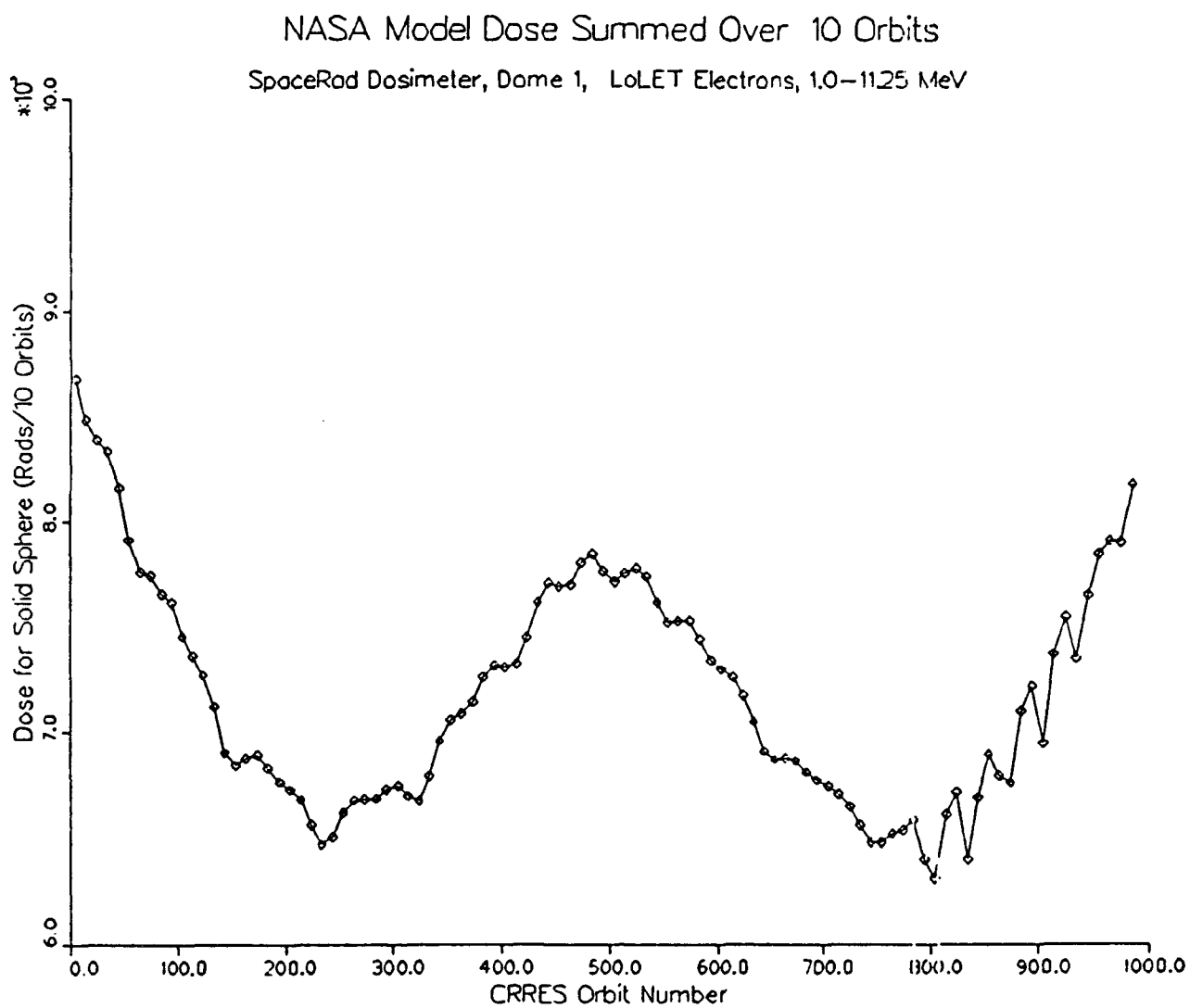


Figure 14. This shows the dose calculated at the center of the LoLet Dome 1 electrons summed over 10 orbits at a time.

Tables of these doses were based on one second fluences and were binned at 1/20 L-shell from L=1 to 3 R_E for 3 different values of B/B₀: 1.00, 1.35 and 2.24.

1.2 Product-associated Data Base Design

1.2.1 Strawman Proposal

A strawman proposal was developed for the CRRES static radiation belt model product-associated data base. This concentrated on the structure, including the binning scheme, as opposed to which instrument data will be used. Chief concerns were the following:

- The data base should be made as compact as possible. Thus, rather than including all selected data at instrument resolution, the data base should contain bin-pass averages.
- The selection of a spatial binning grid coordinate system: Proposals, presented at the Second CRRES-SPACERAD Science Team Meeting (March, 1990, San Diego) by Karl Pfister and AJ Vampola, specify, respectively, a geographic and an L-B binning grid. The advantage of the geographic grid is that no magnetic field model is required to define the coordinates. The principle disadvantage is that if we later choose to sort the geographic bin-passes with respect to an L-B or some other coordinate grid, an undesirable bin edge effect may appear since a geographic bin may straddle two or more bins in the other coordinate system.
- The dimensionality of the spatial binning: Should it be one-dimensional, as we used in the SCATHA analysis, or multi-dimensional? Although we expect the radial variable (altitude, geocentric distance, or L) to vary with time much more rapidly than the other coordinates, a pass through a single radial bin may occasionally extend over a significant range in one or more of the other variables (such as latitude or local time). Thus a breakup of this pass with respect to the other variables may be desired.
- Equatorial or observed pitch angle binning? The data within each spatial bin pass would, of course, be further sorted and averaged within pitch angle bins. Equatorial pitch angle binning has the same objection as the L-binning: a magnetic field model is required to transform from the observed pitch angle to the equatorial pitch angle.

1.2.1.1 Spatial Binning

Geographic bins are favored over L-B bins,to allow the user to later select his own variables with respect to which to sort the data. It is much easier to transform from geographic coordinates to some other coordinates than it is to transform from a B-L coordinate system. To alleviate the bin edge effects, bin-widths would have to be somewhat smaller than would be necessary if we were binning directly with the ultimate sorting parameters (B, L, etc.). The impact of smaller bin widths could be mitigated by using variable bin widths.

To aid in sizing the data base, the number of three-dimensional bins crossed by CRRES in one orbit was determined for the following scenarios:

Variable radial bin widths

$$\Delta r = 0.01, 1.0 \leq r < 2.0$$

$$\Delta r = 0.02, 2.0 \leq r < 6.0$$

$$\Delta r = 0.1, 6.0 \leq r \leq 10.0$$

Fixed radial bin width

$$\Delta r = 0.01$$

The units of r and Δr are R_E . In both cases the geographic latitude and longitude bin widths are fixed at 1° and 15° , respectively. The variable bin width scheme is similar to Al Vampola's proposal, except that the binning is in the geocentric radius r instead of in L , and the widths are 5 times as large. Using a model CRRES orbit based on preflight estimates of the initial conditions, it was found that 663 bins were crossed in the variable radial bin width case, as opposed to 1169 in the fixed radial bin width case. However, in the variable bin-width case, bins near apogee were found to extend up to 40 minutes in duration, making identification and separation of events from quiet periods difficult. Furthermore, local time extents were over one hour for the large apogee bin widths. For these reasons, it seems prudent to use the smaller fixed radial bin width.

As expected, the geocentric distance is the fastest changing variable; a 3-dimensional bin boundary crossing is most often a crossing of a radial bin boundary. Although we have chosen 15° (~1 hour in local time) longitude bins, the longitudinal interval within a 3-dimensional bin is generally much less than this, except near perigee. The latitudinal intervals within the 3-dimensional bins are considerably less than 1° .

1.2.1.2 Sorting Geographic Bins into L Bins

The geographic bins might later be assigned to L -bins. As mentioned earlier, there could be some ambiguity in such an assignment if a geographic bin straddles two or more L -bins. For the two binning cases mentioned above, the starting and ending L bin numbers of each geographic bin were found, assuming that the binning in L would be analogous to the binning in r . L was computed from the IGRF90 + Olson-Pfizer magnetic field model. It was found that the starting and ending L bins were equal for ~80 % of the geographic bins, thus permitting unambiguous assignment.

1.2.1.3 Pitch Angle Binning

For pitch angle sorting, the observed pitch angle is preferred rather than the equatorial pitch angle, since the latter must be computed from an assumed magnetic field model. For near-equatorial latitudes, the two variables are nearly the same. For higher latitudes, a pitch angle bin of a given width transforms into a narrower equatorial pitch angle bin. For example, in a dipole field, an 80° - 90° bin at 20° magnetic latitude transforms to 49.3° - 50.3° at the equator. Therefore, the equatorial pitch angle resolution for particles mirroring at the observation point should be excellent.

Since the angles α and $180^\circ - \alpha$ should be equivalent for static modeling, we should sort these into the same bin. Therefore, 5° pitch angle bins, centered at 5° multiples from 5° to 90° , are recommended, with an additional loss cone bin $0-2.5^\circ$. This would give us 19 bins in all. A single spin covers all pitch angles from β to $180^\circ - \beta$ twice, where β is the angle between the spin plane and the magnetic field vector. If we place supplementary angles (α and $180^\circ - \alpha$) in the same bin, then all accessible bins would be reached, at the 2 rpm spin rate, in ~7.5-15 sec.

1.2.1.4 Format

For each bin pass the data base would consist of the following:

Start, center and end times, and the geocentric coordinates at each;

For each pitch angle bin present:

- the central pitch angle;
- the total counts for each selected channel;
- the delta time for the counts for each channel;
- a data quality flag (contents TBD).

In addition, for each orbit, there would exist a small header file indicating the start and end times, the selected instrument channels, and any other pertinent information. There would also exist a separate informational file containing generally constant information about each of the detector channels that may be used in the data base, including its energy, and how to obtain the flux from the counts. This would not be issued for each orbit, but only a first time, plus any other time there are updates.

This format follows closely Karl Pfister's proposal. If we use Al Vampola's suggestion of 4 energy channels per decade, then we have 24 channels in all, 12 for protons and 12 for electrons. If we assign 16 bits to the counts and 16 bits to the delta time for each, and we assign 16 bits each to the pitch angle and quality flag, then the estimated size, in Megabytes (Mb), of the data base for one orbit (variable radial bin case) is

$$663 \times 25 \times 19 \times 4 \times 10^{-6} \approx 1.25 \text{ Mb}$$

The total per week (16 orbits) would be ~20 Mb. For the fixed radial bin specification, multiply these results by 1169/663 (=1.76). This leads to a weekly requirement of 35 Mb.

1.2.2 L vs Pitch Angle

Radiation belt populations have conventionally been organized by their shell parameter, introduced by McIlwain [1961], and commonly called L. It is often assumed that particles observed at a given location can be assigned an L value independent of pitch angle. However, L clearly depends on the mirror points of a particle and, therefore, on its pitch angle. McIlwain's study of L vs mirror point (Figure 15) shows that, for an internal magnetic field model, the variation is less than 1%. However, CRRES is encountering fields due to magnetospheric currents not included in the model used by McIlwain. Therefore, a brief study has been conducted of the variation of L along a field line for the IGRF85

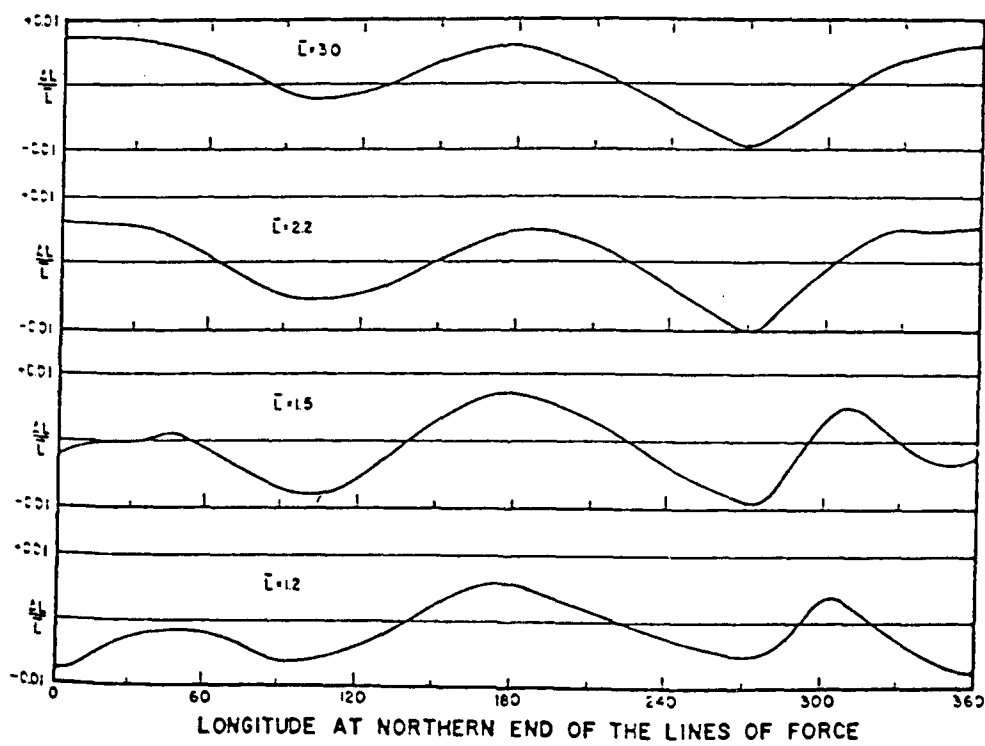


Figure 15. Deviation of L along internal field model lines of force, from *McIlwain* [1961].

(updated to 17 July 1990) + quiet Olson-Pfizer magnetic field model.

L has been calculated for field lines crossing the magnetic equator at $r_0 = 1.5, 2, 3, 4, 5, 6$, and $7 R_E$ from the offset dipole and at local times 0, 2, 4, 6, 8, 10, and 12 hr. The calculation was at the mirror points for equatorial pitch angles $5\text{-}90^\circ$ in steps of 5° . The orientation of the Earth was fixed such that the magnetic longitude of the sun is 0° . Figures 16 through 22 show the results for 0 hr MLT, and Figures 23 through 29 show the results for 12 hr MLT. The parameter plotted is

$$\Delta L/L_0 = [(L-L_0)/L_0] \times 100 \ (\%)$$

where L_0 is the equatorial L value (the value of L at minimum B). Thus L_0 is the L value for the specified equatorial pitch angle. Each figure indicates at the top, r_0 , L_0 , MLT, and the minimum B value, B_0 . For the smaller distances, the lowest pitch angles are excluded since the field line trace stops at the Earth's surface (the mirror points would, therefore, be below the surface).

Figures 16 and 17 are consistent with McIlwain's results that there is less than 1 % variation. Recalling that the Olson-Pfizer contribution is zero at distances $2 R_E$ and less, we are in fact dealing here with just the internal field. Figures 18 through 22, in which the external field is included, exhibit a similar shape which differ from that of Figures 16 and 17, with maximum deviations from 2% for $r_0 = 3 R_E$ to just over 10 % for $r_0 = 7 R_E$.

Figures 23 and 24 (for 12 hr), like Figures 16 and 17, are at distances where only the internal field contributes. Again the variations are less than 1%. The difference between Figures 23 and 24 and the corresponding midnight Figures 16 and 17 is really due to magnetic longitude variation, since at these distances, the magnetic field is independent of local time. From 3 to $7 R_E$ (Figures 25 through 29), the maximum variation again increases above 1 % but is not as high as at midnight. Unlike at midnight, the shapes of the curves at these larger distances vary noticeably with distance.

The largest variations shown here are extreme cases which may occur only rarely during the CRRES history when the apogee is simultaneously near midnight and the equator. A preflight orbital estimate (Figure 30) indicates that for a July 19 launch this could occur about 2 years after the launch, with a prior equatorial crossing of apogee 250 days from launch at 20 hours LT.

1.3 Software

1.3.1 Software Library

We have studied several groups of models in preparation for working with the CRRES data set. These models and the software required to run them constitute a whole suite of routines which will be valuable to CRRES researchers. Thus, we have made them available in a read only library on NOS/VE under :CRES.Jordan.CRRES.PLib for anyone to copy and use at will. There are five subdirectories in this catalog, grouping the software as follows:

$R_O = 1.5 \text{ RE}$
 $L_O = 1.48 \text{ RE}$
 $\Delta L (\% \text{ of } L_O)$
 $\text{MLT} = 0.0 \text{ HR}$
 $B_O = 9306.3 \text{ NT}$

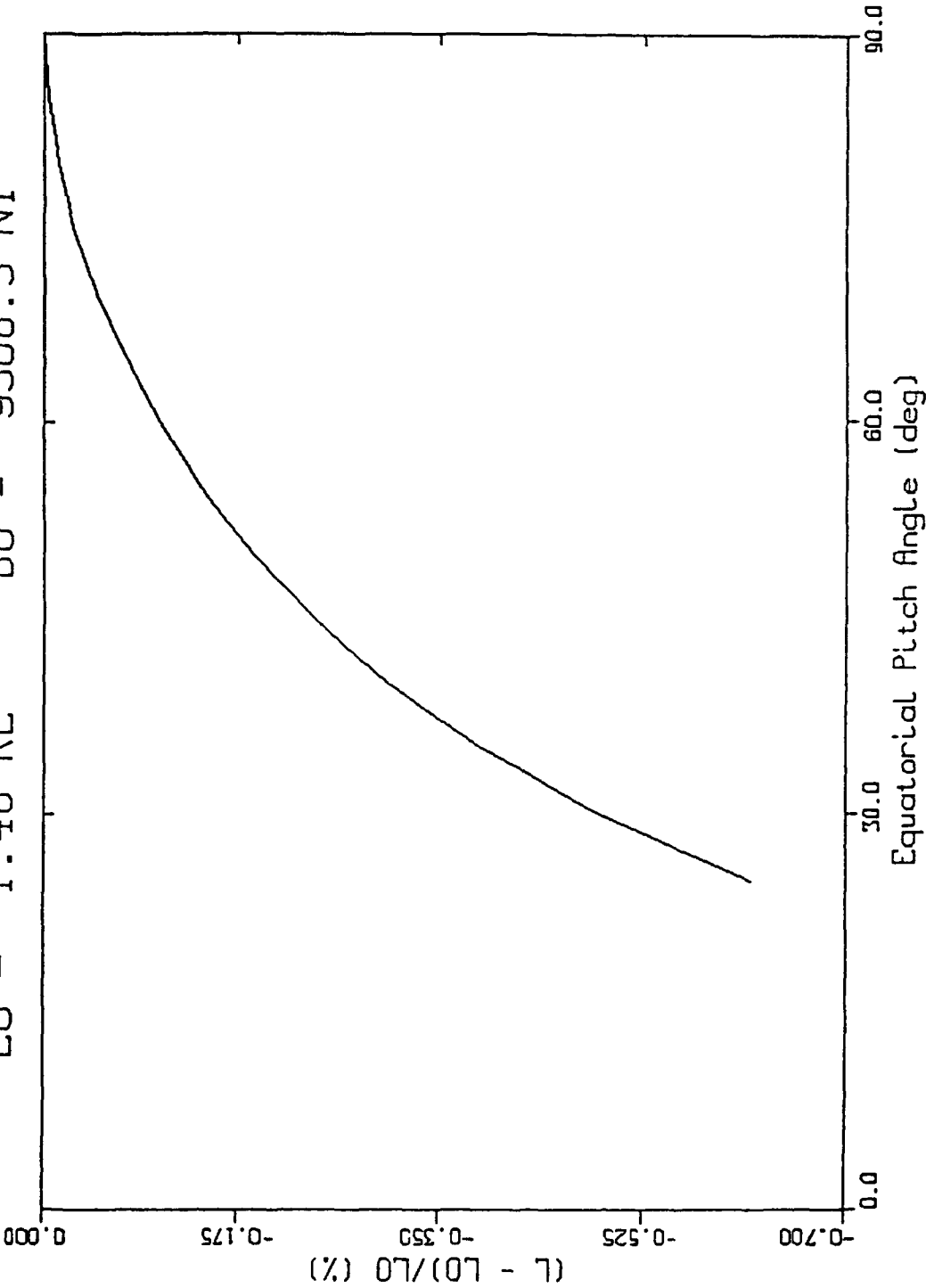


Figure 16. Deviation of L along a magnetic field line of force crossing the midnight equator at $1.5 R_E$. The IGRF85 and Olson-Pfitzer quiet model field is used.

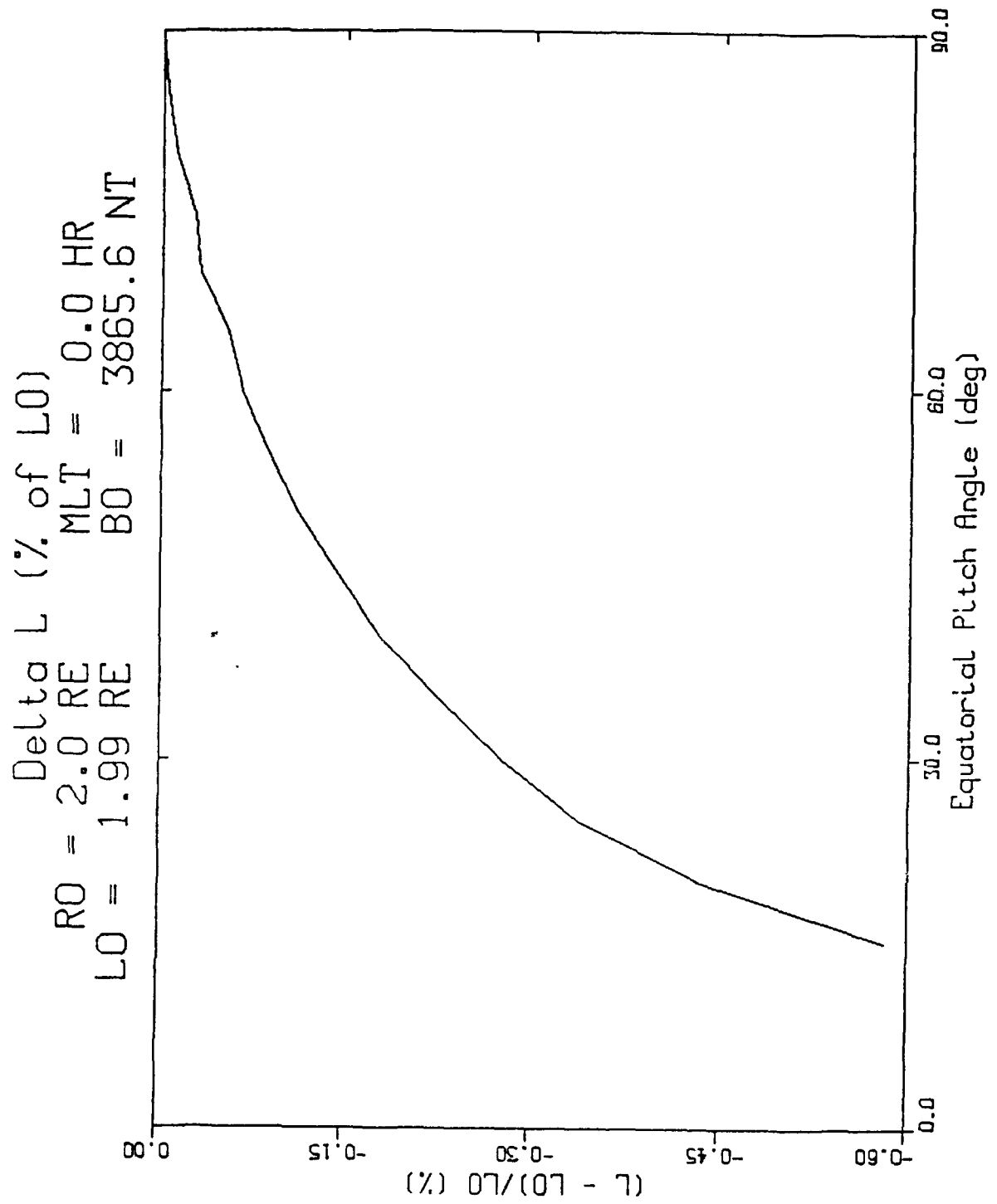


Figure 17. Same as Figure 16, except for 2 RE.

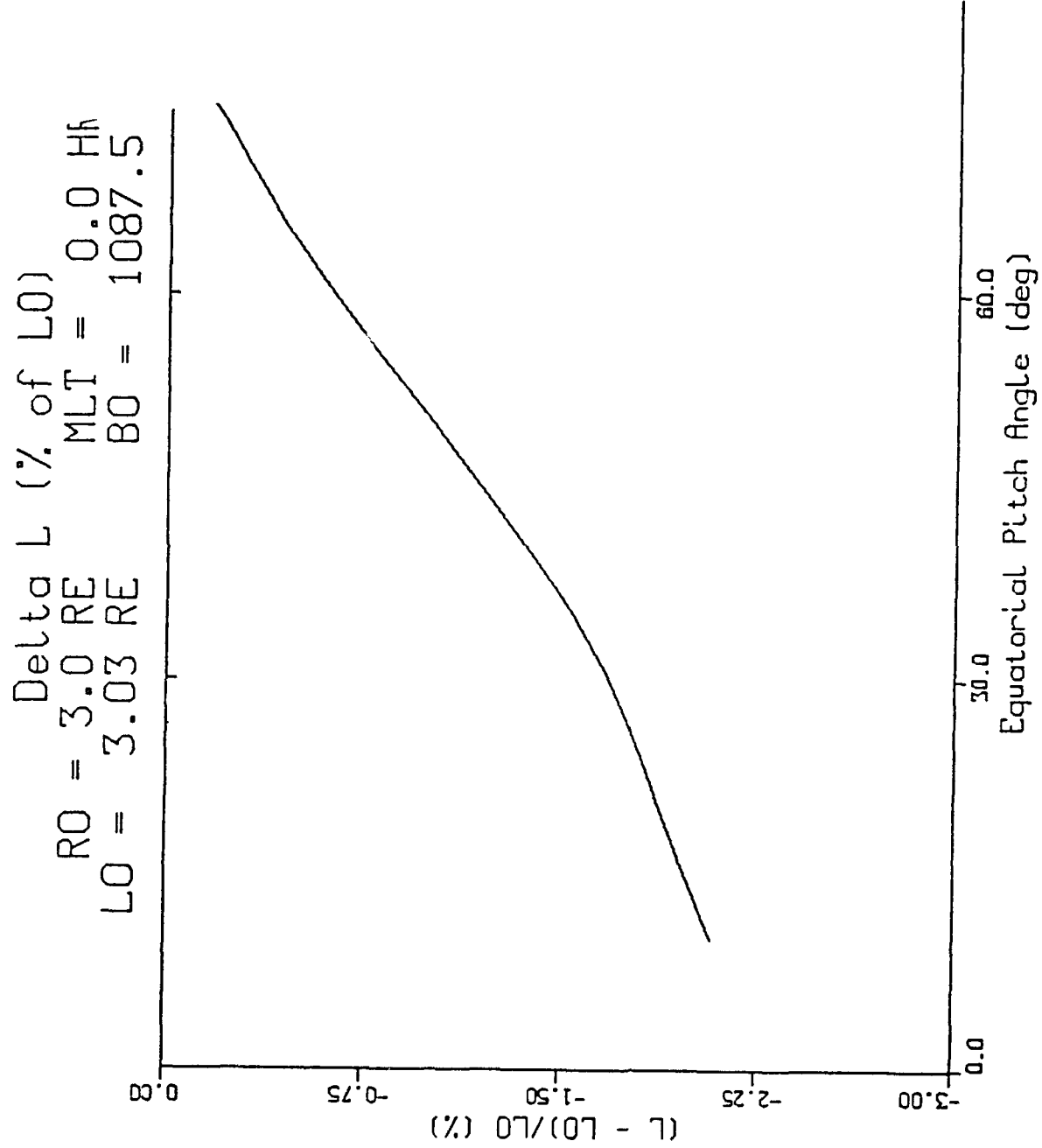


Figure 18. Same as Figure 16, except for $3 R_E$

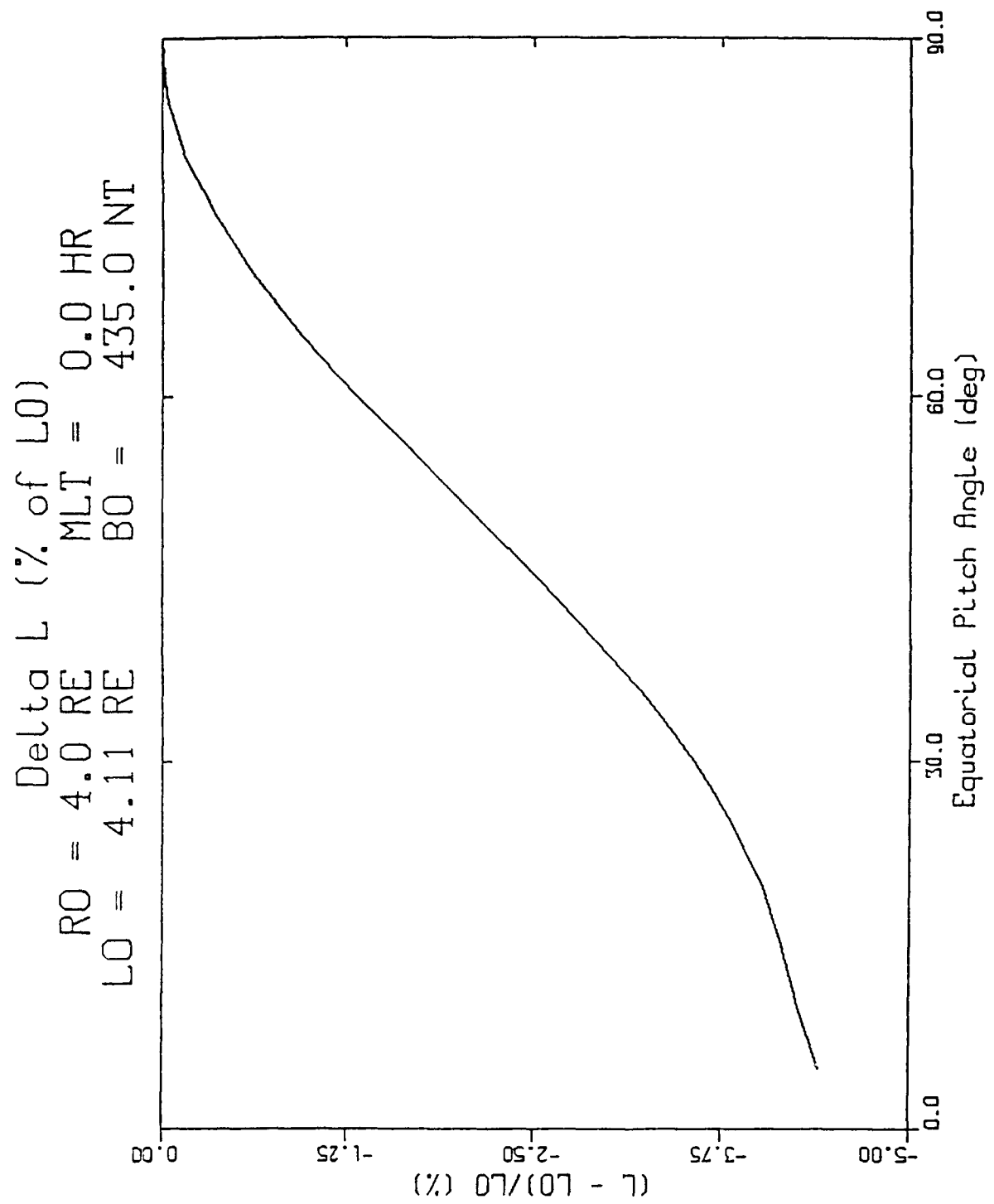


Figure 19. Same as Figure 16, except for $4 R_E$.

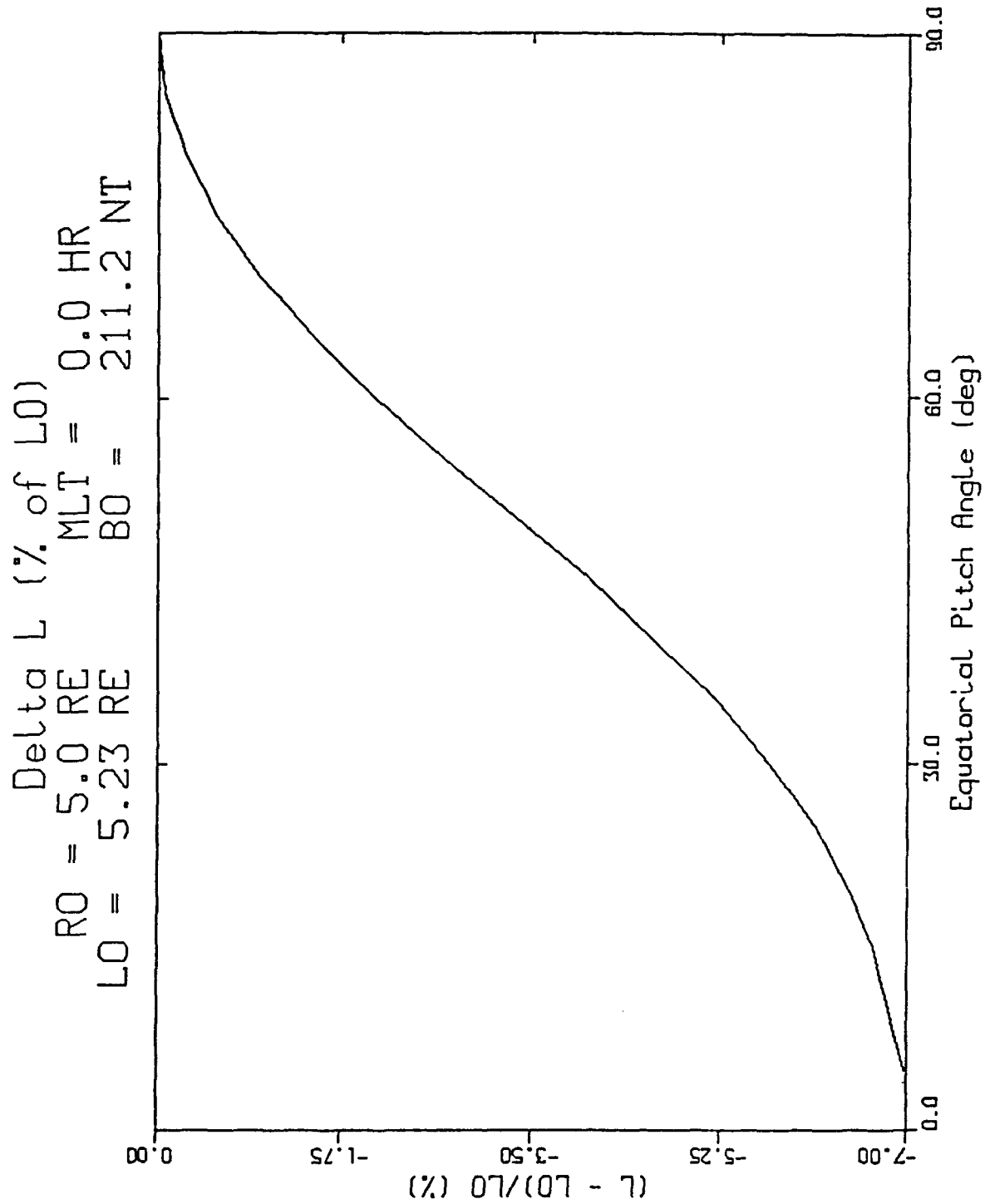


Figure 20. Same as Figure 16, except for $5 R_E$.

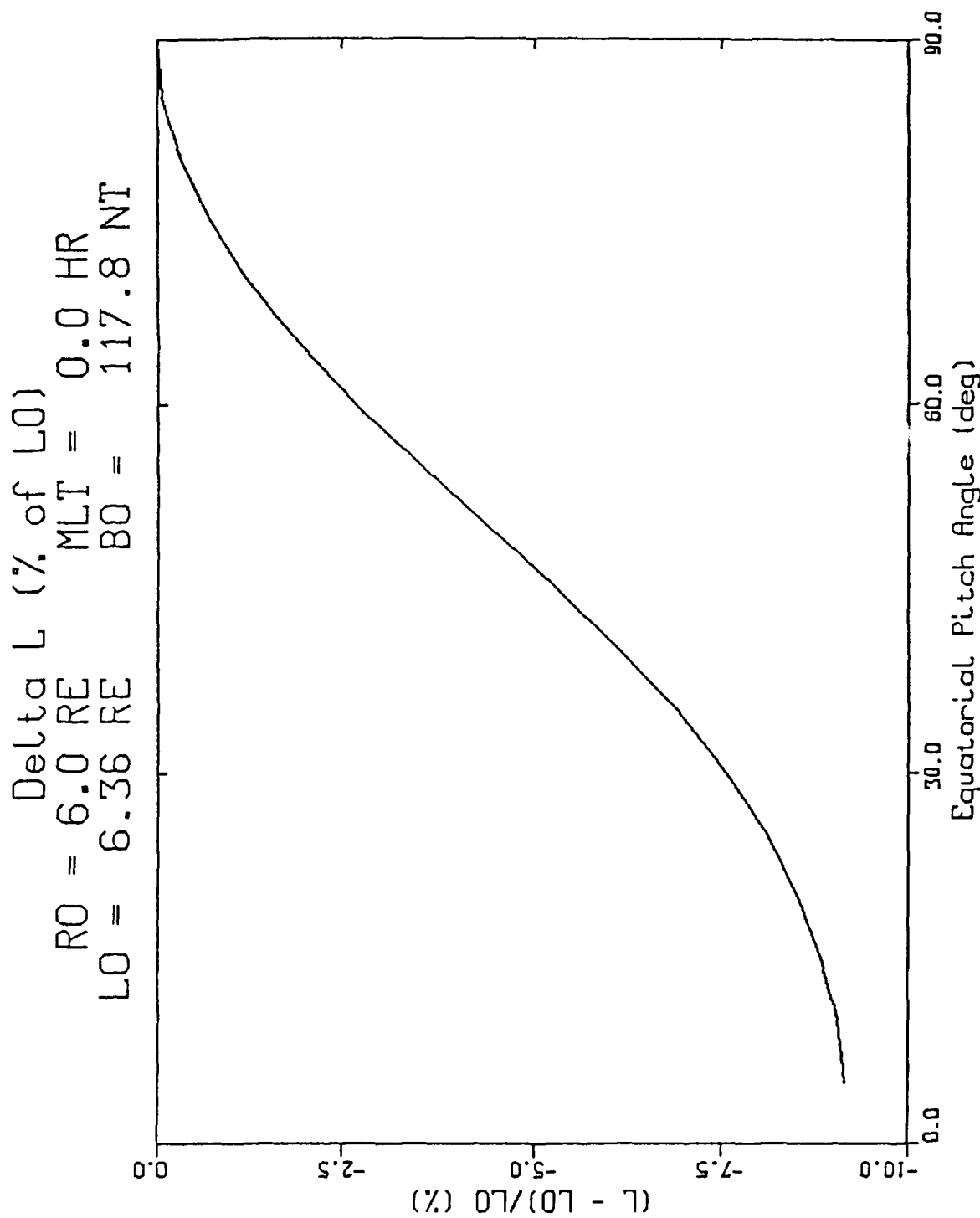


Figure 21. Same as Figure 16, except for 6 RE.

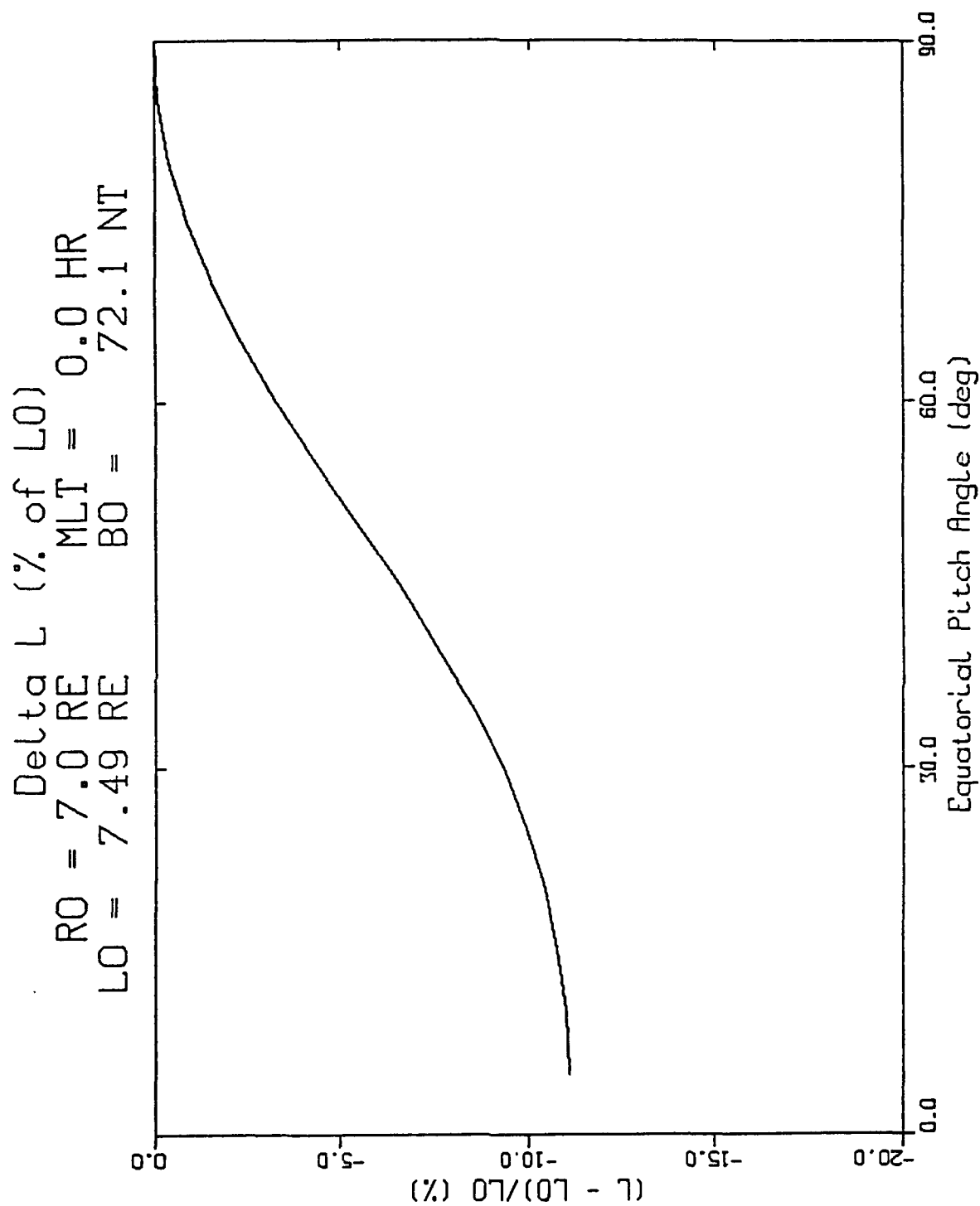


Figure 22. Same as Figure 16, except for $7 R_E$.

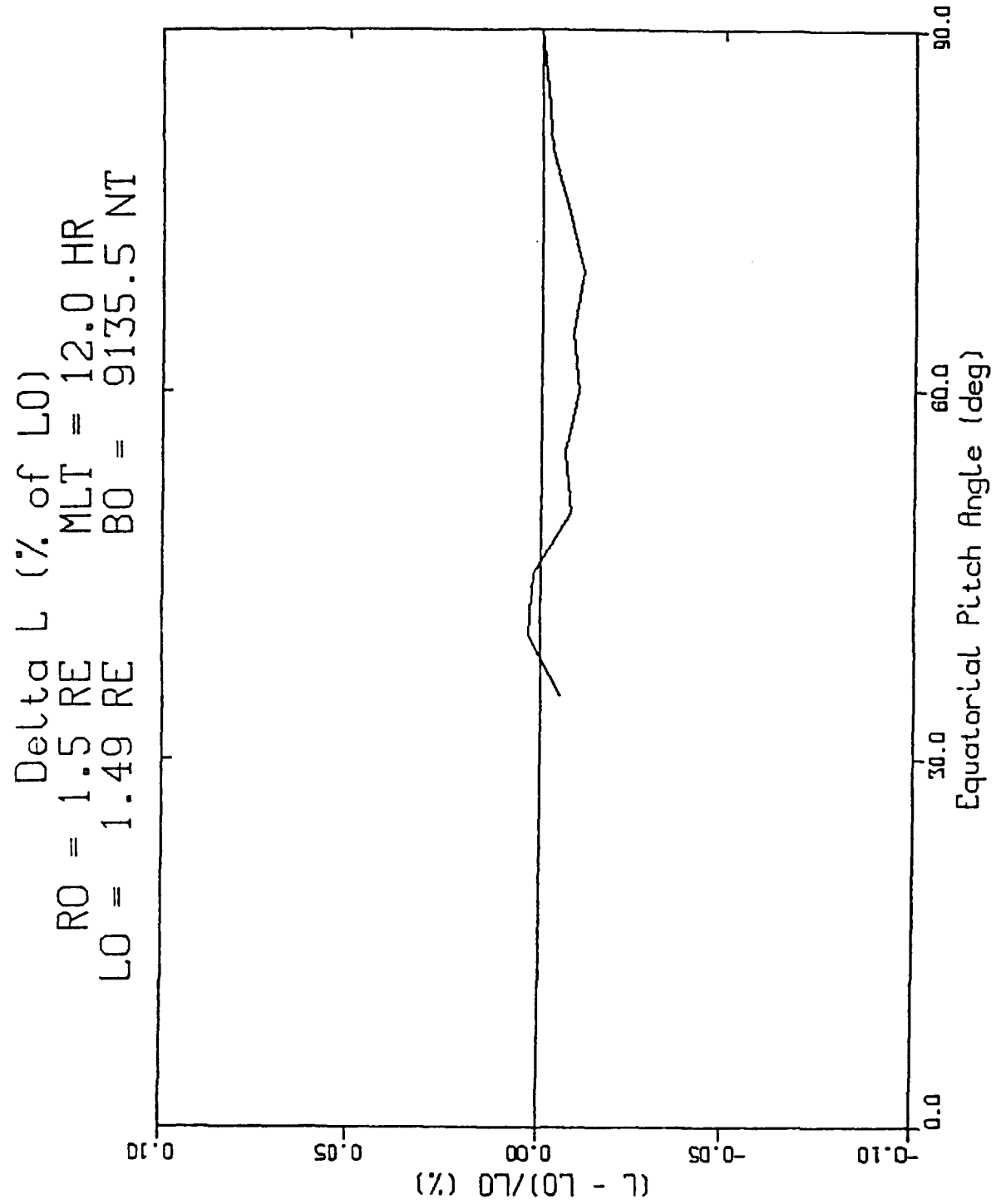


Figure 23. Same as Figure 16, except at noon instead of midnight.

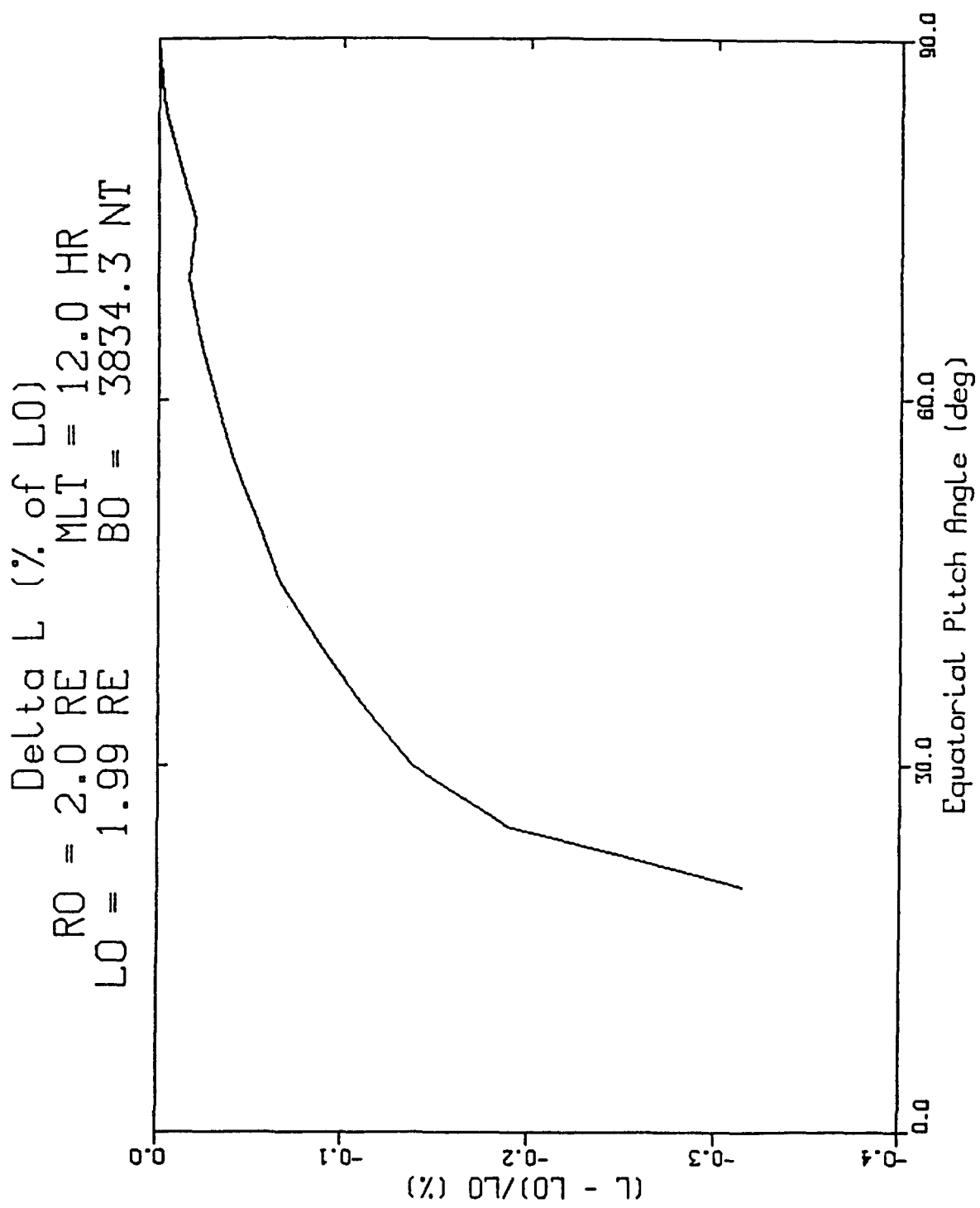


Figure 24. Same as Figure 17, except at noon instead of midnight.

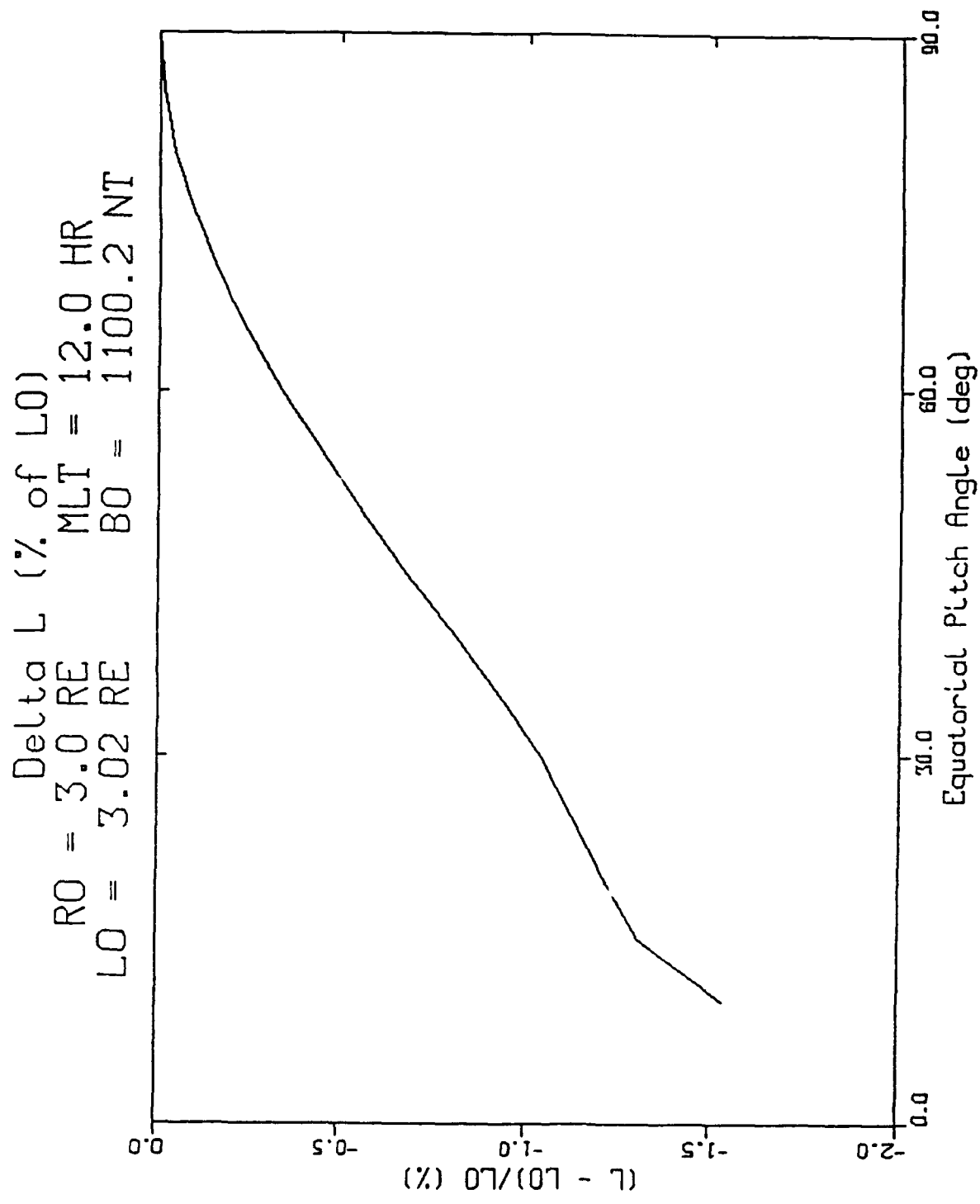


Figure 25. Same as Figure 18, except at noon instead of midnight.

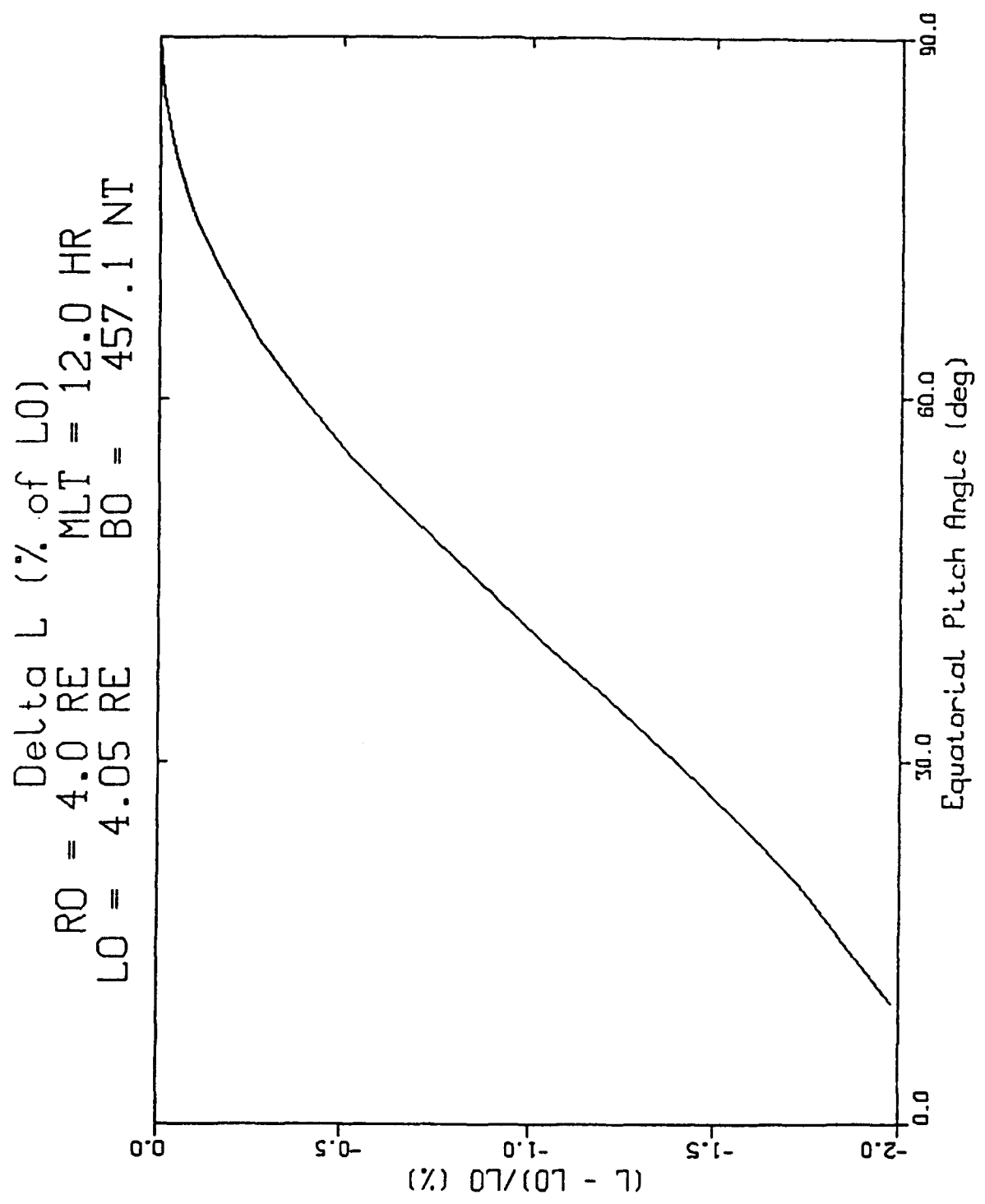


Figure 26. Same as Figure 19, except at noon instead of midnight.

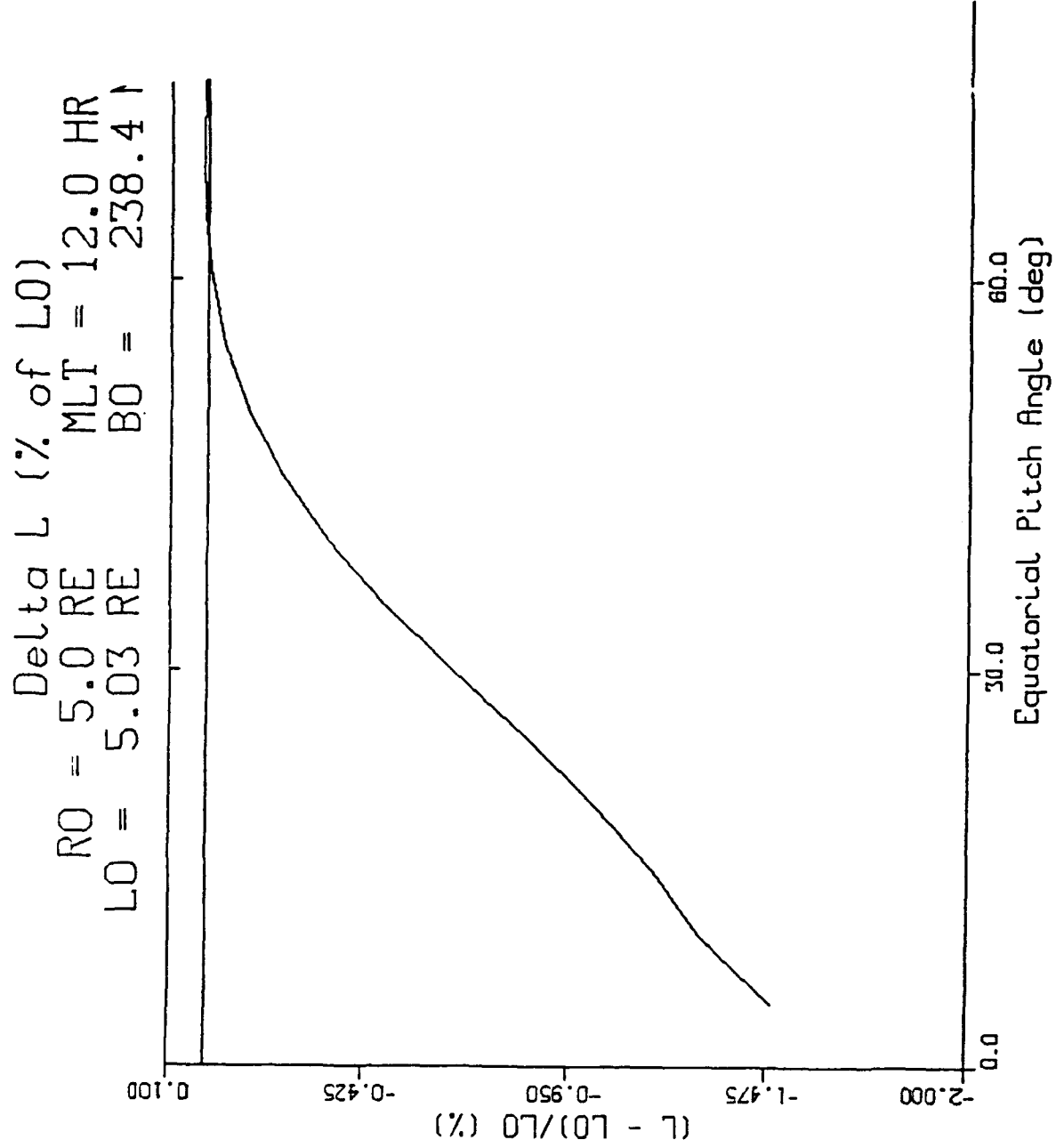


Figure 27. Same as Figure 20, except at noon instead of midnight.

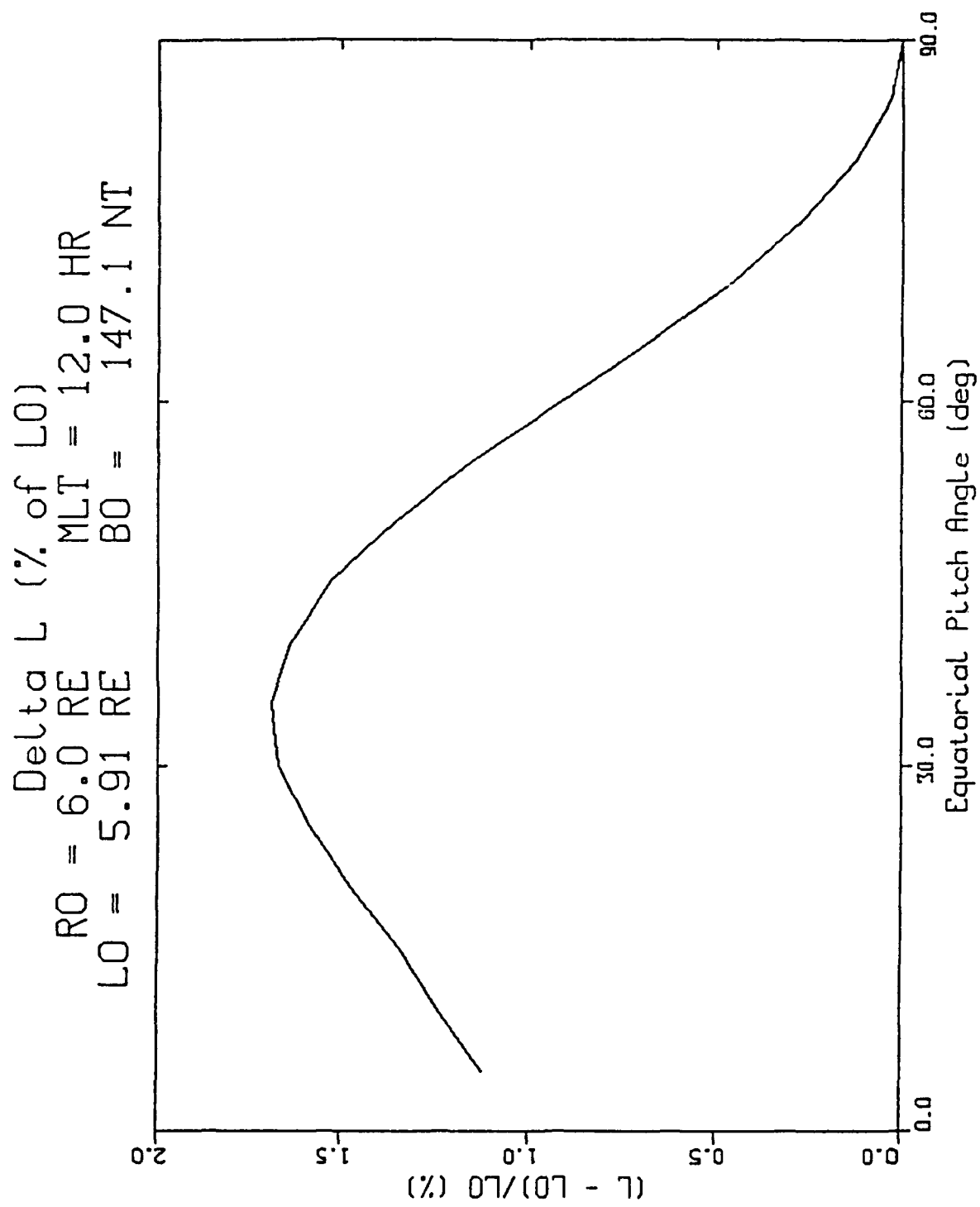


Figure 28. Same as Figure 21, except at noon instead of midnight.

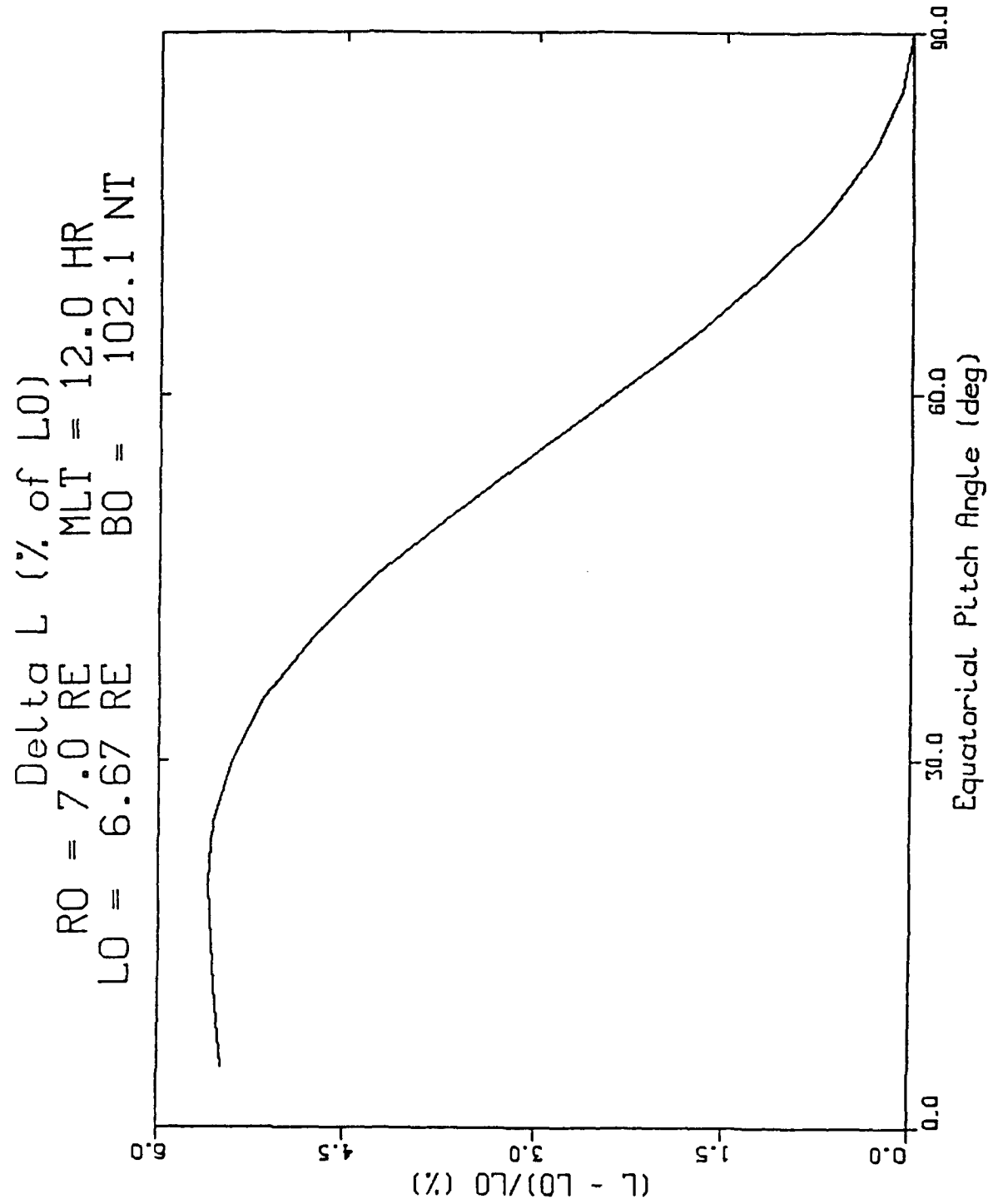


Figure 29. Same as Figure 22, except at noon instead of midnight.

89/12/18.

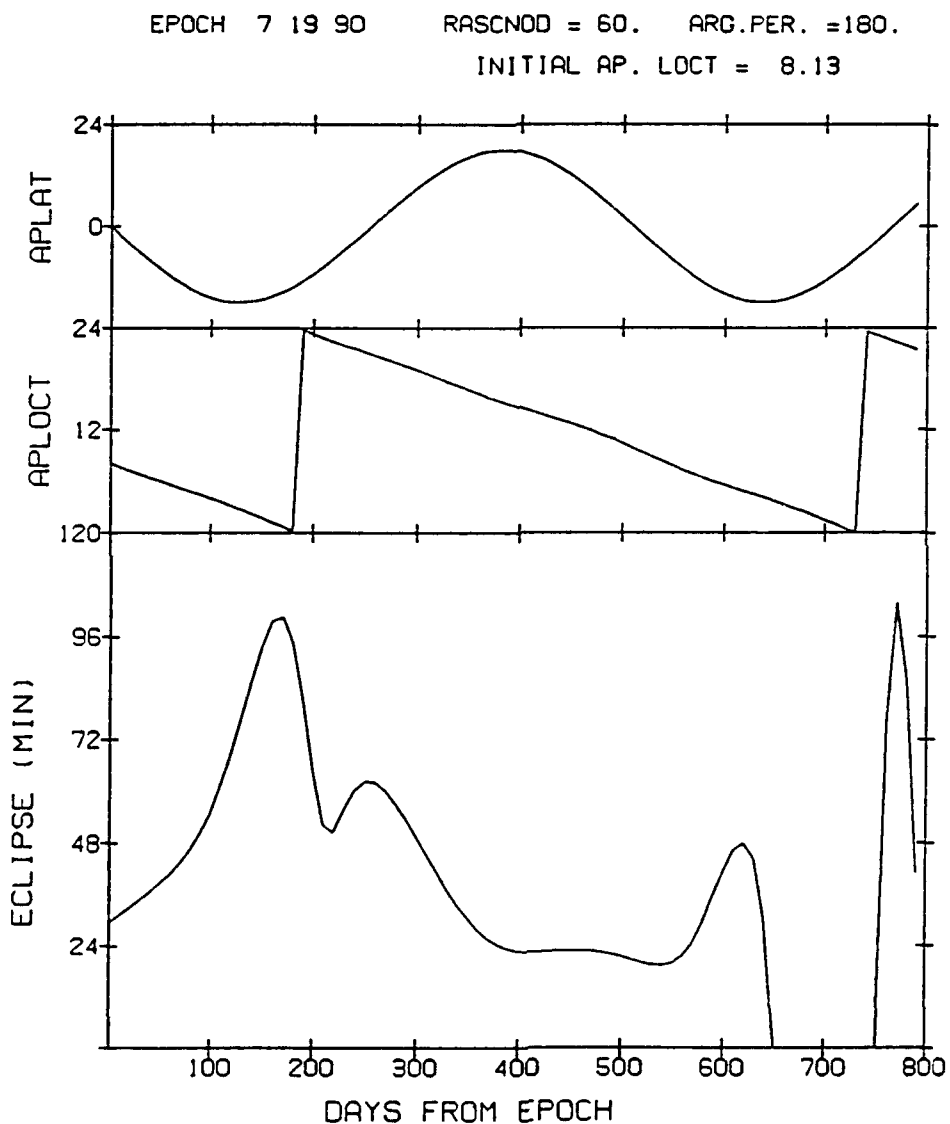


Figure 30. Predicted CRRES orbital parameters.

- 1) Coords -- coordinate transformation routines,
- 2) Eph_Att -- ephemeris and attitude routines with sample files,
- 3) ExtFlds -- external magnetospheric magnetic field models and the code to run them,
- 4) IntFlds -- internal magnetospheric magnetic field models and the code to run them, and
- 5) RadBlts -- NASA trapped radiation belt models and the code to run them.

Within these directories, the following routines reside:

1) Coords

- a) Conrvt -- converts geodetic to geocentric coordinates and vice versa,
- b) Transf -- converts ECI to GSE, geographic, GSM, SM, VDH, and DM, and vice versa,

2) Eph_Att

- a) AGMOD -- attitude program which performs line of sight calculations,
- b) CAF01040 -- sample attitude file,
- c) E000S001 -- sample ephemeris file,
- d) E000S002 -- sample ephemeris file,
- e) ReadEph -- reads an ephemeris file and prints out the header,

3) ExtFlds

- a) BXYZHV -- subroutine containing the Hilmer-Voigt model,
- b) BXYZMD -- subroutine containing the Mead model,
- c) BXYZNO -- dummy subroutine with no external field model,
- d) BXYZOP -- subroutine containing the Olson-Pfizer tilt-dependent model,
- e) BXYZT89 -- subroutine containing the Tsyganenko 1989 model,
- f) DrvrEqB -- sample driver program shows how to set-up a model run; must be linked to a BXYZ__ file and to the library ExMdAft,
- g) EqBMDJob -- sample job for submitting a model run to the batch queue,
- h) ExMdAft -- library of required routines for a model run,
- i) ExMdSrc -- source code of the library routines,
- j) HV_In -- sample Hilmer-Voigt input parameters,
- k) Md_In -- sample Mead input parameters,
- l) T89Par -- Tsyganenko 1989 parameter file required to be in the directory during a run,
- m) T89_In -- sample Tsyganenko 1989 input parameters,

4) IntFlds

- a) CInteg -- Cain's integration routine to obtain B and L,
- b) GenBL -- gets B and L for a given latitude, east longitude, and altitude for one of several provided internal field models,
- c) Intrp85 -- Cain's interpolation method to get L and the invariant latitude for 1985,
- d) Intrp90 -- Cain's interpolation method to get L and the invariant latitude for 1990,

5) RadBlts

- a) AE8Max -- NASA trapped electron model for solar maximum conditions,
- b) AE8Min -- NASA trapped electron model for solar minimum conditions,
- c) AP8Max -- NASA trapped proton model for solar maximum conditions,
- d) AP8Min -- NASA trapped proton model for solar minimum conditions,
- e) Model87 -- sample code to run the trapped particle models, 1987 version, and
- f) RadBelt -- sample code to run the trapped particle models, 1988 version.

1.3.2 Other Developments

1.3.2.1 Conversion of Observed Pitch Angles to Equatorial

The product-associated data base described above provides distributions of trapped particle populations in the observed pitch angle at the location of the satellite, \mathbf{r} . For further modeling and analysis, it is useful to convert to distributions in the equatorial pitch angle, which would be measured at the equatorial crossing \mathbf{r}_e of the field line through \mathbf{r} (see Figure 31 below), thereby removing the variation of pitch angle with latitude. This can be done by the Liouville theorem, from which it follows that

$$f_e(\alpha_e) = f(\alpha) \quad (12)$$

where

- f_e = the pitch angle distribution at \mathbf{r}_e ;
- α_e = the pitch angle at \mathbf{r}_e ;
- f = the pitch angle distribution at the point \mathbf{r} ,
- α = the pitch angle that a particle with equatorial pitch angle α_e at \mathbf{r}_e would have at the point \mathbf{r} .

From the constancy of the first adiabatic invariant:

$$\frac{\sin^2 \alpha}{\sin^2 \alpha_e} = \frac{B}{B_e} \quad (13)$$

where B and B_e are the magnetic field vector magnitudes at \mathbf{r} and \mathbf{r}_e , respectively.

Note that there is a maximum pitch angle $\alpha_{e\max}$ for which the equatorial distribution function f_e can be determined from the distribution function f at \mathbf{r} . This is given by

$$\sin^2 \alpha_{\text{emax}} = \frac{B_c}{B} \quad (14)$$

This is the largest equatorial pitch angle for which particles can mirror at points of latitude greater than or equal to the latitude of the point r (Figure 31).

Program EQMAP performs the conversion, specified by Equation (13), of observed pitch angle to equatorial pitch angle for each of 19 observed pitch angle bins for the set of positional bin passes in a product associated data base. The central and maximum angle of each bin are converted. The bins are assumed to be centered at multiples of 5°, except for a loss cone bin, 0-2.5°, and the last bin, 87.5°-90°. An input file is required containing, for the time center of each positional bin pass, the magnetic field magnitudes at the satellite and at the equatorial crossing. An output file is created containing all the information of the input file, plus the resulting equatorial pitch angles.

1.3.2.1.1 Subroutine BFLDSM

Program OPTRACE [RADEX, Inc, 1987] has the capability to compute L for a specified point. This value relates to the second adiabatic invariant only for particles which mirror at this point, that is, particles whose pitch angles are 90° at this point. The second adiabatic invariant for a non-90° pitch angle particle is related instead to the L value at the points where that particle mirrors. These points are specified by

$$B_m = \frac{B_0}{\sin^2 \alpha} \quad (15)$$

where B_0 is the magnetic field magnitude at our initial point, B_m is the mirror point magnetic field magnitude, and α is the pitch angle at the initial point. The closest point, satisfying Equation (15) on each side of the initial point, must be found. The L value then depends on the invariant integral between these two points:

$$I = \int_c^d \sqrt{1 - B(s)/B_m} ds \quad (16)$$

where c and d are the two points where the particle mirrors, $B(s)$ is the magnetic field magnitude at a point s on the field line, B_m is the mirror point magnetic field magnitude according to Equation (15), and ds is an element of length along the field line.

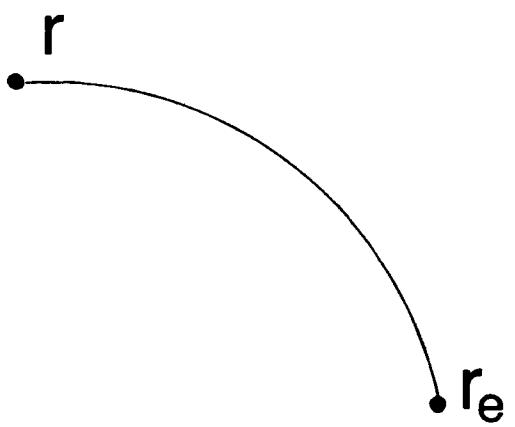


Figure 31. Magnetic field line passing through a given vector location \mathbf{r} and crossing the Equator at \mathbf{r}_e .

To perform the calculation requires the following steps:

- 1) Trace the field line through the initial point to both Earth intercepts;
- 2) Determine the B value, by Equation (15), for the points where the particle mirrors;
- 3) Search for these points along the field line traced in step 1;
- 4) Compute the invariant integral I, Equation (16), for these points, and then L from McIlwain's or Hilton's approximation.

Subroutine BFLDSM, a modification of the OPTRACE package, contains the option to save a traced field line in a common memory area. For each point along the line, the cartesian coordinates, altitude, and magnetic field magnitude are saved. The inputs to the routine are:

1. Date and GMT
2. Positional coordinates

The output is the traced field line just described, stored northern-most points first. Step 2 is a simple calculation, using Equation (15). Steps 3 and 4 can be performed by subroutine LB, part of the BFLDSM package. It takes as its input, a traced field line, as just described, and the B value at the mirror point (B_m of Equation (15)). The output is the desired L value. BFLDSM has been used in the L vs pitch angle studies described in section 1.2.2, above, and in program PADEPL, described below (section 1.3.2.2).

The BFLDSM package must be linked with the OPTRACE package, and with object modules named IGRF85 and BXYZMU, respectively, for the desired internal and external field models. These would be used instead of the default modules in the OPTRACE package.

Incidentally, the BFLDSM package contains modules also for the following:

- 1) Writing saved field lines to disk for subsequent display using field line plot packages;
- 2) Finding the location and value of the minimum magnetic field magnitude;
- 3) Finding the equatorial crossing;
- 4) Finding the low altitude footprints.

1.3.2.1.2 CRRES Coordinate Transformation Software Library

This package permits one to perform transformations of rectangular coordinates or vector components between the Earth Centered Inertial (ECI) coordinate system and the following:

Geocentric Solar Ecliptic (GSE)
Geographic (GEOG)
Geocentric Solar Magnetospheric (GSM)
Solar Magnetic (SM)
Vehicle Dipole Horizon (VDH) or Dipole Meridian (DM)

These coordinate systems, described in detail by *Bhavnani and Vancour* [1991], are summarized below. Since we describe right-handed coordinate systems, it is necessary to define only two of the coordinate axes.

Earth Centered Inertial (ECI)

The z-axis is along the Earth's rotational axis, positive north; the x-axis points to the vernal equinox. Origin is center of the Earth.

Geocentric Solar Ecliptic (GSE)

The x-axis points from the center of the Earth to the sun; the z-axis is perpendicular to the ecliptic plane (parallel to the ecliptic pole), positive north. Origin is center of Earth.

Geographic (GEOG)

The z-axis is along the Earth's rotational axis, positive north; the x-axis points to the Greenwich meridian. Origin is center of Earth.

Geocentric Solar Magnetospheric (GSM)

The x-axis points from the Earth to the sun; the z-axis is perpendicular to the x-axis, in the plane containing the x-axis and the magnetic dipole axis, positive north. Origin is center of Earth or location of offset dipole.

Solar Magnetic (SM)

The z-axis is along the magnetic dipole axis, positive north; the x-axis is perpendicular to the z-axis, in the plane containing the z-axis and the sun, positive toward the sun. Origin is center of Earth or location of offset dipole.

Vehicle Dipole Horizon (VDH) or Dipole Meridian (DM)

The z-axis (H) is parallel to the magnetic dipole axis, positive north; the y-axis (D) is perpendicular to the z-axis and the vector from the origin to the point of interest, positive east. Origin is point of interest.

The Offset Dipole Location

In the GSM, SM, and VDH systems the option exists to use either the center of the Earth or the location of the offset dipole as the coordinate origin. The location of the offset dipole is defined as that position, which, if used as a coordinate origin, would result in the vanishing of the ($n=2, m=0$) and ($n=2, m=1$) coefficients of the spherical harmonic expansion of the Earth's magnetic field in a coordinate system whose z-axis is aligned with the dipole. (See *Chapman and Bartels* [1940] for details). To use the offset dipole option, the input vector (the vector in the coordinate system to be transformed from) must be in km. When transforming from the ECI system to either GSM or SM, the appropriate rotation matrix is applied to the vector difference between the input vector and the offset dipole displacement from the center of the Earth, in the ECI system. In the inverse transformation, the input vector is rotated to ECI, then the ECI offset dipole displacement vector is added to the result.

1.3.2.2 L vs Pitch Angle for Ephemeris

In a static radiation belt model, the mirror point L and B values should serve as independent variables. To develop such a model, data should be sorted with respect to these variables and the energy. It is frequently assumed that L is constant along a field line, and therefore, independent of pitch angle for particles observed at a given position. However, as discussed previously, there can be considerable variation near geosynchronous altitude in a realistic magnetic field model. Therefore, it appears prudent to obtain the pitch-angle-dependent L for each observation, rather than the L at the specified location, given on the ephemeris file. This latter L is just the value for particles with 90° pitch angles. Therefore, program PADEPL has been developed which provides a supplement to the ephemeris file containing, for each record on the ephemeris file, the L values for each of the pitch angle bin centers defined in the above paragraph. The pitch-angle dependent L values may then be computed for arbitrary times and pitch angles by conventional interpolation schemes as is done for the standard ephemeris variables.

1.3.2.3 Adiabatic Invariants and Dipole-Equivalent Invariants

To facilitate the study of radiation belt dynamics, *Schulz* [1991] (Spring AGU Meeting) has recommended organizing the CRRES radiation belt particle data in terms of the adiabatic invariants. These are defined as action integrals pertaining, respectively, to the basic three approximately separable periodic components of the motion of magnetospherically trapped particles: the spiraling motion of the particle about a guiding center, the motion of the guiding center along field lines, and the longitudinal drift motion of the guiding center around the Earth. In the absence of an electric field component parallel to the magnetic field, the first invariant reduces to a very simple expression:

$$\mu = p^2/(2mB_m), \quad (17)$$

where p is the particle's momentum, m its mass, and B_m is the mirror point magnetic field magnitude, given by

$$B_m = B/\sin^2\alpha, \quad (18)$$

where B is the magnetic field magnitude at a given location traversed by the particle, and α is the pitch angle at that location.

The second adiabatic invariant is given by

$$J = 2pI_m, \quad (19)$$

where,

$$I_m = \int \sqrt{1 - B(s)/B_m} ds, \quad (20)$$

with the integral taken along the field line between the particle's mirror points. $B(s)$ is the magnetic field magnitude at a point s on the field line.

In these expressions, and in what follows, the subscript m is used to designate a mirror point quantity. Thus, B_m is the magnetic field at the mirror point of a particle, as opposed to the point of observation. I , without the subscript, can be considered a function of position if B_m is replaced by B at the position in question and the integral is taken between that position and its conjugate point. The subscript emphasizes the dependence of these quantities on the mirror points rather than the position of observation. The mirror point, in turn, is a function of the point of observation and the pitch angle.

The third adiabatic invariant is given by

$$\Phi = \int \mathbf{B} \cdot d\mathbf{a}, \quad (21)$$

where the integral is over any surface enclosed by the drift orbit.

Note that, if the magnetic field is static, the particle momentum is fixed and the parameters I_m and B_m serve equally as well as the adiabatic invariants for parameterizing the particle trajectories, since they are then functions of μ and J and are, therefore, themselves invariant. Thus, I_m and B_m specify the set of mirror points through which the particle passes in its orbit, and therefore, completely specify the orbit. In this case, the third invariant, the flux enclosed by the drift orbit, is not an independent parameter. However, its place as a constant of the motion may be taken by the particle's energy. The constancy of these parameters disappears in time-varying fields in which the resulting induction electric field does work on the particles, thus, changing their energies and momenta. I_m and B_m must correspondingly be adjusted to conserve μ and J .

McIlwain [1961] has defined a shell parameter L_m as a function of I_m and B_m . This parameter is, therefore, adiabatically conserved if I_m and B_m are. In a dipole field, L_m is the equatorial crossing distance of the shell of field lines through which the particle passes. Therefore, at a given location, all particles have the same L_m value regardless of pitch angle. Since this relationship remains approximately valid in the Earth's internal field, L_m has a distinct advantage over I_m for organizing the inner belts. As a function of position, L is constant along a dipole field line and approximately constant along field lines of the Earth's internal field.

1.3.2.3.1 Equivalent Parameters

A problem with the adiabatic invariants is the difficulty in working with them due to lack of familiarity. We are more accustomed to energy spectra, radial distributions, and pitch angle distributions. Thus, we are motivated to define a set of equivalent invariants - the energy, L_{md} , and equatorial pitch angle that particles with a given set of adiabatic invariants would attain if the magnetic field changed adiabatically to a specified reference field. In the past, the Mead model has been used as the reference field [Bass, et. al., 1989]. A simpler choice would be a dipole field. We would, therefore, call these parameters dipole-equivalent invariants. First, we have, for the dipole-equivalent L_{md} :

$$L_{md} = -2\pi M/\Phi, \quad (22)$$

where M is the dipole moment of the chosen dipole reference field. A review of *Roederer* [1970] and *Schulz and Lanzerotti* [1974] leads to the conclusion that this is the L parameter used by them in diffusion equations, rather than McIlwain's parameter. Unlike the latter, L_{md} is a function of the third adiabatic invariant, and, therefore, would not change under adiabatic variations of the magnetic field. Furthermore, this L_{md} is actually independent of a particle's mirror points in a symmetric non-dipole field. Thus, any dependence on mirror points reflects shell-splitting in an asymmetric field.

To obtain the dipole-equivalent equatorial pitch angle, α_d , we note the following [*Roederer*, 1970]:

$$I_m^2 B_m = \text{constant} \quad (23)$$

which follows from Equations (17) and (18), and constancy of J and μ . After substituting known dipole expressions for B_{md} and I_{md} as functions L_{md} and α_d , we solve for α_d . Finally, constancy of the first adiabatic invariant supplies the ratio p_d/p , where p_d is the dipole-equivalent momentum, and p is the observed momentum. From this ratio, we may obtain the dipole-equivalent energy E_d for any observed energy.

1.3.2.3.2 Software

Figure 32 summarizes software that has been developed to compute the adiabatic invariants and dipole-equivalent invariants. As indicated in the top block, we are given the particle position, pitch angle, energy, mass, and the time. The first step is to compute the set of energy-independent parameters for specified positions and pitch angles in a given field model. These are the quantities B_m , I_m , L_m , and Φ . Subroutine ADINV performs this function (in this and all subsequent blocks, CAPS enclosed by parentheses indicate subroutine names). This is the most CP-time-intensive step of the process, and will be described in more detail below. The remainder of the procedure has two alternatives. If one desires the adiabatic invariants, it is prudent to take the left-hand branch, in which the first two adiabatic invariants, J and μ , are obtained by direct substitution (subroutine ADINV2) of I_m and B_m into Equations (17) and (19). The dipole-equivalent invariants are then obtained, as described above, using subroutine DIPINV. The right-hand branch may be followed if one needs only the dipole-equivalent invariants, but is computing them for several energies and/or masses. Then it is noted that the first two of these, L_{md} and α_d , are independent of mass and energy, thus, needing to be determined only once at a given location, time, and pitch angle. Along with these, a third mass/energy independent parameter, the ratio p/p_d is also determined. These are collectively called energy-independent dipole-equivalent parameters. Finally, the dipole-equivalent energy can be determined for each mass and energy

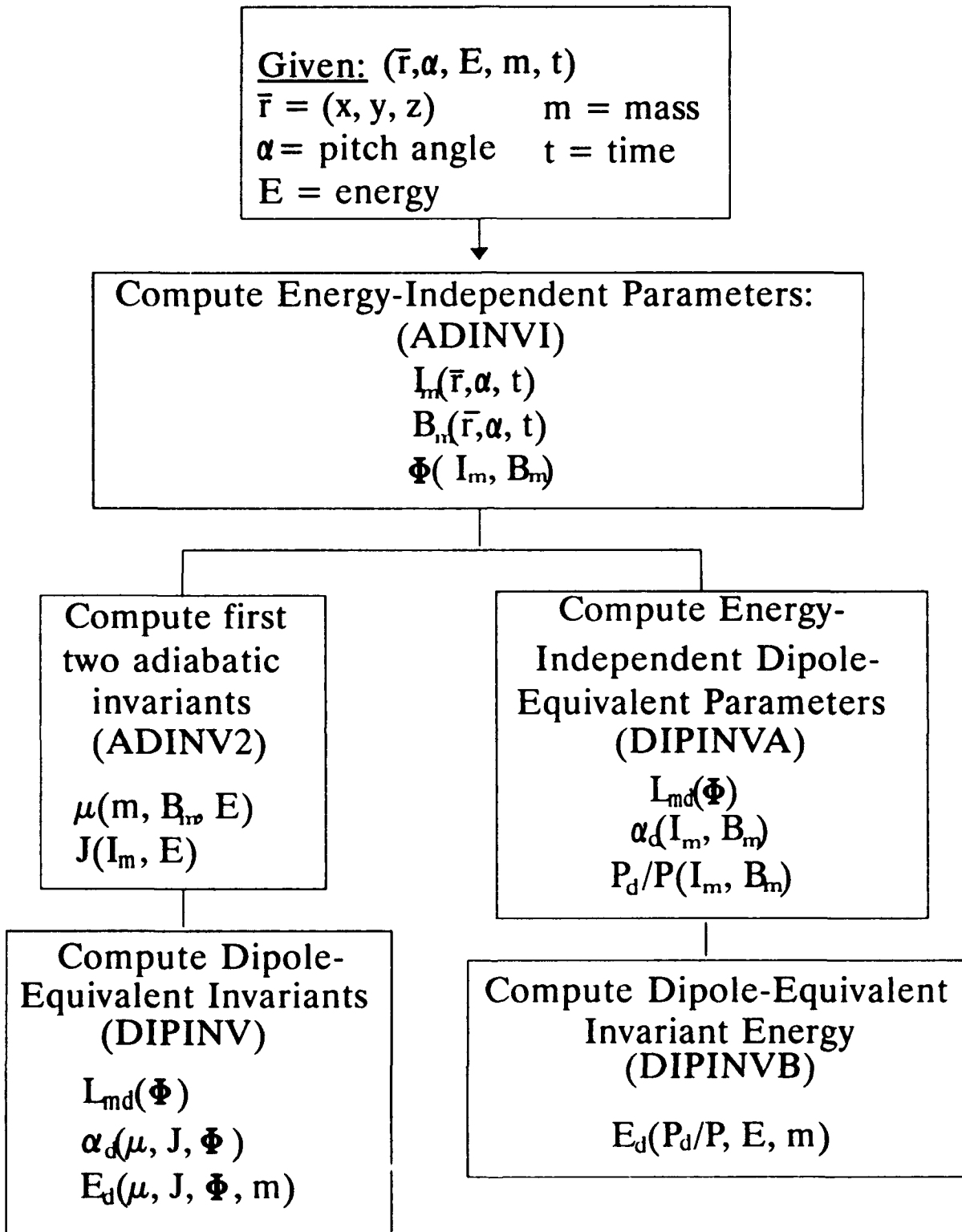


Figure 32. Overview of software for computation of adiabatic invariants and dipole equivalent invariants.

(subroutine DIPINVB).

The computation of the energy-independent parameters (subroutine ADINV) requires three stages:

- 1) Trace the magnetic field line through the position of interest and compute the magnetic field value at that specified location.
- 2) For each pitch angle, determine the mirror point magnetic field value B_m and the mirror point integral I_m , using Equations (18) and (20).
- 3) For each pitch angle, compute the third invariant Φ Equation (21).

Stage 3 requires the determination of the drift shell, defined by the set of field lines containing the mirror points of the requisite I_m and B_m . The magnetic equatorial crossing distances of the drift shell are determined at each of 25 equally spaced local times between 0 and 12 hours. That portion of the shell between 12 and 24 hours is determined from the portion between 0 and 12 hours by dawn-dusk symmetry. The required field line crossing the equator, at a given local time, is found by iterative search (subroutine LBSRCH). The initial guess for the crossing distance is the value of L_m , McIlwain's function of B_m and I_m . Then the value of L at the point $B=B_m$ along this field line is found. If this value is within $10^{-4} R_E$ of the required L_m , then the search is terminated. Otherwise, the difference is used to correct the equatorial crossing distance and the process repeated until the crossing distance is determined to within specified accuracy ($10^{-4} R_E$). Generally this takes 3-5 iterations.

Given the set of equatorial crossing distances defining the drift shell, the third invariant is computed by (subroutine INVAR3), using code provided by Lockheed, Inc. [Nightingale, et. al., 1986]. This code computes the third invariant in 3 different ways:

- 1) Compute directly the magnetic flux crossing that portion of the equatorial surface bounded by the drift shell. In this approach, the region of the equatorial surface near the origin is replaced by a hemisphere to avoid the singularity in the magnetic field at the origin.
- 2) Compute the flux crossing that portion of a hemispherical surface of specified radius enclosed by the drift shell.
- 3) Compute the line integral of the vector potential along the intersection of the drift shell with a hemispherical surface of specified radius.

For a divergence-free magnetic field, these approaches give the same result. However, since the latter two methods require the additional field line tracing to the specified surface, only the first method has been used here.

1.4 References

- Baker, D. N., Higbie, P. R., Hones, E. W., Jr., and Belian, R. D., High resolution energetic particle measurements at $6.6 R_E$: 3. Low-energy electron anisotropies and short-term substorm predictions, *J. Geophys. Res.*, vol. 83, no. A10, p. 4863, 1978.
- Bass, J. N., Gussenhoven, M. S., and Redus, R. H., "The Importance of Adiabatic Variations in Trapped Particle Distributions Observed by the SCATHA Satellite", GL-TR-89-0233, 29 Nov 1989, ADA220859.
- Bhavnani, K. H., and Vancour, R. P., "Coordinate Systems for Space and Geophysical Applications", PL-TR-91-2296, Dec 1991.
- Chapman, S., and Bartels, J., *Geomagnetism*, Vol. II, Oxford at the Clarendon Press, London, p. 648, 1940.
- Gussenhoven, M. S., Mullen, E. G., and Sagalyn, R. C., "CRRES/SPACERAD Experiment Descriptions", Air Force Geophysics Laboratory Report AFGL-TR-85-0017, p. 66, 1985, ADA160504.
- Hanser, F. A., Hardy, D. A., and Sellers, B., "Calibration of the Rapid Scan Particle Detector Mounted in the SCATHA Satellite", Air Force Geophysics Laboratory Report AFGL-TR-79-0167, 1979, ADA082382.
- Heinemann, M., Representations of currents and magnetic fields in anisotropic magnetohydrostatic plasma, *J. Geophys. Res.*, vol. 95, no. A6, p. 7789, 1990.
- Hilmer, Robert V., *A Magnetospheric Magnetic Field Model with Flexible Internal Current Systems*, A thesis submitted in partial fulfillment of the requirements for the degree doctor of philosophy, Rice University, Dept. of Space Physics and Astronomy, Houston, TX, 1989.
- McIlwain, C. E., "Coordinates for Mapping the Distribution of Magnetically Trapped Particles", *J. Geophys. Res.*, Vol. 66, No. 11, Pp. 3681-3691, 1961.
- Mullen, E. G., and Gussenhoven, M. S., "SCATHA Environmental Atlas", Air Force Geophysics Laboratory Report AFGL-TR-83-0002, pp. 27-76, 1983, ADA131456.
- Nightingale, R. W., Chiu, Y. T., Davidson, G. T., Francis, W. E., Rinaldi, M. A., Robinson, R. M., and Vondrak, R. R., "A Space Radiation Test Model Study", AFGL-TR-86-0064, 1986, ADA169412.
- Olson, W. P., and Pfitzer, K. A., "Magnetospheric Magnetic Field Modeling", Annual Scientific Report, AFOSR Contract No. F44620-75-C-0033, McDonnell Douglas Astronautics Company, Huntington Beach, CA, 1977.
- Radex, Inc., "CRRES Data Processing Ephemeris File Generation System Product Development Specification", Radex, Inc., Bedford, MA 01730, RXR87041, 1987.

Radex, Inc., "Integrated Analytical Evaluation and Optimization of Model Parameters Against Preprocessed Measurement Data", Radex, Inc. Final Report, GL-TR-89-0163, 1989, ADA215518.

Roederer, J. G., "Dynamics of Geomagnetically Trapped Radiation", Springer-Verlag, Berlin/Heidelberg/New York, 1970.

Schulz, M., and Lanzerotti, L. J., "Particle Diffusion in the Radiation Belts", Springer-Verlag, Berlin/Heidelberg/New York, 1974.

Schulz, M., and McNab, M. C., "Source-Surface Model of the Magnetosphere", Aerospace Corp., Space Sciences Lab, Rpt. No. SSL-87(7165)-1, Nov 1986.

Schulz, M., "Opportunities for Radiation Belt Modeling: Empirical and Theoretical", *Spring Meeting 1991 Program and Abstracts*, EOS Suppl., p. 232, 1991.

Stern, D. P., "Parabolic Harmonics in Magnetospheric Modeling: The Main Dipole and the Ring Current", J. Geophys. Res., Vol. 90, No. A11, Pp. 10,851-10,863, 1985.

Tsyganenko, N. A., A magnetospheric magnetic field model with a warped tail current sheet, *Planet. Space Sci.*, vol. 37, no. 1, p.5, 1989.

Vasyliunas, V. M., Mathematical models of magnetospheric convection and its coupling to the ionosphere, in *Particles and Fields in the Magnetosphere*, edited by B. M. McCormac, p. 60, D. Reidel, Hingham, Mass., 1970.

West, H. L., Jr., The signatures of the various regions of the outer magnetosphere in the pitch angle distributions of energetic particles, in *Quantitative Modeling of Magnetospheric Processes, Geophys. Monogr. Ser.*, vol. 21, edited by W. P. Olson, p. 150, AGU, Washington, D. C., 1979.

2.0 DYNAMIC MAGNETIC FIELD MODELS

2.1 Models Published Before 1989

In the Earth's magnetosphere, the magnetic field is the sum of two parts: that which we will call the "internal" field because it is due to sources (currents) in the Earth's interior, and, that which we will call the "external" magnetic field because it is due to sources outside the Earth's surface. Since its sources are in the interior of the Earth, the internal field, at a point outside the Earth's surface, is curl-free. Therefore, the internal field can be expressed as the gradient of a scalar potential.

Since the magnetic field is also divergence-free, the scalar potential satisfies Laplace's equation and is, therefore, commonly expressed as an expansion in spherical harmonics.

The external field, unlike the internal, is not, in general, current-free and usually cannot be expressed as the gradient of a scalar potential. However, since the external currents are more amenable to observation, more can be said about them than the internal currents. Thus, external field modeling has frequently begun with models of the current from which the field is subsequently derived. The currents, included in most models, are those known as ring currents, cross-tail currents, and magnetopause currents. The ring currents, carried by trapped ions and electrons in the 20-50 keV energy range, circulate longitudinally around the Earth at distances 2-7 R_E . The cross-tail currents flow from dawn to dusk across the night-side plasma sheet. Some models also include the associated return currents, flowing around the magnetopause from dusk to dawn. The magnetopause currents are the Chapman-Ferraro boundary currents, which are formed by the interaction of the magnetosphere with the solar wind. The field, due to the magnetopause currents alone, can be expressed in terms of a scalar potential (for points inside the magnetosphere). There is another system of currents, the field-aligned currents, which none of the models to be discussed here include explicitly.

The CRRES satellite will provide data for a generation of new models of the Earth's radiation belts. Since the orbits of the trapped high energy radiation belt particles are controlled by the Earth's magnetic field, the accuracy of the models will largely be determined by the accuracy of the magnetic field models used in ordering the data. Present radiation belt models neglect the external magnetic field. While this approximation may be acceptable for the inner belt, it becomes questionable at larger distances because the external field accounts for an increasing fraction of the total field.

This subsection reviews the models listed in Table 2. We begin with the derivation and mathematical construction of these models. A comparison of computation times for the models is given.

Table 2. External Magnetic Field Models

- Olson-Pfizer Tilt Dependent [*Olson and Pfizer, 1977*]
- Olson-Pfizer Dynamic [*Pfizer, et. al., 1988*]
- Mead-Fairfield [*Mead and Fairfield, 1975*]
- Tsyganenko-Usmanov [*Tsyganenko and Usmanov, 1982*]
- Tsyganenko [*Tsyganenko, 1987*]
- Stern Parabolic Magnetopause/Stretched Magnetosphere [*Stern, 1985, 1987*]

Primary interest for radiation belt analysis are the properties of the McIlwain L parameter and the magnitude of the total (internal + external) magnetic field vector since these have been the traditional sorting parameters for modeling the trapped particle populations. Comparisons of the L parameter among the models are presented. Next, we compare the total magnetic field vector derived from the models with those observed by the SCATHA satellite for a quiet and a moderately active period. Finally, model depiction of the night side equatorial magnetic field depression as a function of distance is compared with averaged measurements by the AMPTE and OGO satellites. The equatorial field is critical to the magnetic mapping of auroral phenomena to the plasma sheet.

2.1.1 Model Derivation and Description

Most of the models begin with some description of the three current systems we mentioned above, viz., the ring currents, the cross-tail currents, and the magnetopause currents. The contributions of these three current systems are modeled separately and summed to produce the total magnetic field vector.

In this report, we will frequently refer to the Solar Magnetic (SM) and Geocentric Solar Magnetospheric (GSM) coordinate systems, following the terminology of *Russell* [1971]. In both systems the x-z plane contains the dipole and the Earth-Sun line, while the y-axis is positive toward dusk. In the SM system the z-axis is parallel to the dipole, positive toward the north, while the x-axis is positive on the sunward side of the dipole. In the GSM system, the x-axis is along the Earth-Sun line, positive toward the Sun, while the z-axis is positive on the northward side of the Earth-Sun line.

2.1.1.1 Olson-Pfizer Tilt Dependent Model

The Olson-Pfizer tilt dependent model [*Olson and Pfizer*, 1977] is a revision of the tilt-averaged model of *Olson and Pfizer* [1974]. Tilt here refers to the complement of the Sun-dipole angle. The motivation for the revision was that the tilt-averaged model is not a good representation of the zero tilt case, primarily at large distances on the midnight equator. When the dipole is tilted, the plasma sheet has been observed to be parallel with the GSM equatorial (x-y) plane but not coincident with it [*Stern*, 1976]. Simple models [*Murayama*, 1966; *Speiser and Ness*, 1967; *Fairfield and Ness*, 1970] postulate that the plasma sheet is hinged to the dipole equatorial plane $8\text{-}11 R_E$ from the Earth. Locations on the dipole equator outside the hinging distance are, therefore, in the plasma sheet only when the dipole is untilted. Since the plasma sheet is an area of minimum field strength, the field at zero tilt is generally smaller than the average field for such points on the dipole equator.

The SM components of B_{ext} are expressed as sums of terms of the form

$$[A_{ijk} + B_{ijk} \exp(-0.06r^2)]x^i y^j z^k$$

where the coefficients A_{ijk} and B_{ijk} are simple linear or quadratic functions of the tilt. The model contains no dependence on magnetic activity but is proposed as an average model for quiet conditions ($K_p = 0, 1$). Spatially, it is valid from $2.5 R_E$ to $15 R_E$, except beyond the noon magnetopause at $10.5 R_E$. The model is not rigorously divergence free.

2.1.1.1.1 Model Derivation

Like the 1974 tilt-averaged model, the tilt-dependent model was constructed by first considering models for the current systems. The magnetopause currents are similar to those developed by *Olson* [1969] from a self-consistent solution to the Mead-Beard pressure balance condition. However, for the tilt-dependent model, an empirical shape for the magnetopause surface was chosen instead of Olson's self-consistent solution. Magnetopause currents and their resulting contribution to the field were computed numerically.

The ring and cross-tail currents are constructed from a system of wires [*Olson*, 1974]. The ring currents were made from appropriately placed elliptical wires, such that their noon crossings were at lower radial distances than their midnight crossings. Therefore, the resulting ring current is not azimuthally symmetric. However, dawn-dusk symmetry was retained by placing the elliptical foci on the SM x-axis. The flow in the inner three wires is eastward, while in the remaining wires, it is westward. The boundary between eastward and westward current density is $\sim 5 R_E$ at midnight, $3 R_E$ at noon. The cross-tail currents are constructed from loops consisting of dawn-to-dusk flow on the northern and southern surfaces of the hinged plasma sheet ($\Delta z_{GSM} = \pm 3 R_E$), coupled, respectively, to return currents over the northern and southern surfaces of the magnetopause. The loops are tilted relative to the normal to the plasma sheet in order to model the decay of B_z with increasing distance down the tail. When the dipole is tilted, the loops near the inner edge are tilted toward the normal to the dipole equator plane.

Parameters specifying the wires (position, orientation, size, and shape), their currents, and the magnetopause shape were adjusted so that the resulting total external field fit OGO-3 and -5 observations in the inner magnetosphere [*Sugiura, et. al.*, 1971], and Explorer-33 and -35 observations in the tail [*Mihalov, et. al.*, 1968; *Behannon*, 1970; *Meng and Mihalov*, 1972]. The resulting field, still numerical in form, was fit by linear least squares to the analytic series described above.

2.1.1.2 Olson-Pfizer Dynamic Model

This model [*Pfizer, et. al.*, 1988] is the result of a series of event studies performed for NASA Coordinated Data Analysis Workshops (CDAW). The principal feature of this model is the introduction of variable strength factors multiplying the quiet models of the fields of the three current systems. The magnetopause strength factor varies inversely as the cube of the standoff distance, which may be computed from the solar wind pressure and speed by:

$$R_{st} = 98/(nv^2)^{1/6} \quad (24)$$

with R_{st} in R_E , n the solar wind ion density in particles/cc, and v the solar wind speed in km/sec. The quiet model assumes $R_{st} = 10.5 R_E$. The field due to the magnetopause is scaled geometrically in accordance to this scaling of the magnetopause. Thus, the field at the position r due to the scaled magnetopause is

$$B(r, R_{st}) = k^{-3} B_{quiet}(r/k) \quad (25)$$

where $k = R_{st}/10.5$.

The contribution due to the tail current system is scaled in the same way as the magnetopause contribution, both in strength and geometry. An index suggested by Akosofu [*Olson and Pfister, 1932*], which was successfully employed in tail field modeling for the CDAW 2 event, was found to be unsatisfactory for subsequent events. The ring current system is scaled in strength only, using the D_{st} index:

$$S_{ring} = 1.0 - 0.03 D_{st} \quad (26)$$

The unscaled (quiet) models of these systems are similar in mathematical form to the quiet tilt-dependent model. However, the dynamic model is valid only for zero tilt. Spatially the model is valid from $2.5 R_E$ to $60 R_E$ on the night side, and out to the magnetopause on the day side. Like the tilt-dependent model, the dynamic model is not divergence-free.

2.1.1.3 Mead-Fairfield Model

In the Mead-Fairfield model [*Mead and Fairfield, 1975*] each component of B is expressed as an expansion in products of polynomials in the SM coordinates and the dipole tilt. The SM coordinates are actually rotated westward by the approximate solar wind aberration angle of 4° (the shift in the solar wind direction due to the orbiting Earth). Thus, there is symmetry about a plane 4° west of the noon-midnight meridian, rather than about the noon-midnight meridian itself. For each of $4 K_p$ bins ($0,0^+; 0-2^-; 2-9; 3-9$) the coefficients were derived from the data by least squares, enforcing the zero divergence condition by a set of linear constraints on the coefficients. The model provides no description of the individual current systems but the total current can be derived by taking the curl of the magnetic field vector.

The data base consisted of 12,616 averaged vector measurements by magnetometers on board satellites Explorer 33 (IMP A-D), Explorer 34 (IMP-4), Explorer 41 (IMP-5), and Explorer 43 (IMP-6) [*Behannon, 1968; Fairfield, 1969; Fairfield and Ness, 1972; Fairfield, 1974*]. The averaging was over half-Earth radii, which typically spanned 10-15 minutes. The data base contains gaps in the near-Earth equatorial region, and at high southern latitudes. Specifically, there are few measurements within $5 R_E$ of the Earth and none within $4 R_E$. Thus, the model is valid for radial distances between 5 and $15 R_E$.

2.1.1.4 Tsyganenko-Usmanov and Tsyganenko Models

The Tsyganenko-Usmanov [*Tsyganenko and Usmanov, 1982*] and *Tsyganenko* [1987] models are expressed as sums of the contributions from the three external sources mentioned above. The ring current and tail current contributions are expressed analytically by functions which are the curls of vector potentials; hence, their divergences vanish identically. Both models employ a mathematically simple azimuthally symmetric ring current circulating around the dipole. In contrast to the Olson-Pfister models, the ring current flow direction is westward, independent of distance from the Earth. Accurate modeling of the innermost region was not attempted due to insufficient data coverage. In the

Tsyganenko-Usmanov model, the tail current flows mainly from dawn to dusk on a flat sheet "hinged" or offset a distance z_0 on the GSM z-axis due to the dipole tilt. Both models use tilt-dependent products of polynomials and decaying exponentials in the coordinates to represent the magnetopause current contribution. For these, the zero divergence condition was enforced while determining the coefficients. The data bases for these models contain the Mead-Fairfield data base as a subset. The Tsyganenko data base is more extensive at large distances down the tail; hence, it has a more elaborate tail model.

2.1.1.4.1 Ring Current Model

The ring current field in both models is given by:

$$B_\rho = B_0 [12\rho' z' / (\rho'^2 + z'^2 + 4)^{5/2}] \quad (27a)$$

$$B_z = 4B_0 [(2z'^2 - \rho'^2 + 8) / (\rho'^2 + z'^2 + 4)^{5/2}] \quad (27b)$$

$$B_\phi = 0 \quad (27c)$$

Where $\rho' = \rho/\rho_0$, $z' = z/z_0$, ρ , z , and ϕ are cylindrical coordinates with the z-axis parallel to the dipole, and B_0 and ρ_0 are adjustable parameters. The maximum ring current density is located at $\rho = \rho_0$, while the strength of the current is proportional to B_0 .

2.1.1.4.2 Tail Current Models

The tail current field is the product of a field due to an infinitely extended current in the dawn-dusk direction and a y-dependent factor that was introduced to improve model-observation agreement in the dawn and dusk regions of the near-Earth magnetotail. The Tsyganenko-Usmanov model contains seven adjustable parameters and the Tsyganenko model contains nine. The Tsyganenko model also contains return current sheets at $30 R_E$ above and below the GSM equator, each equal in magnitude to half the main tail currents.

2.1.1.4.3 Magnetopause Current Models

The magnetopause current expansion consists of products of powers of the coordinates y and z perpendicular to the Earth-Sun line, decaying exponentials down tail, and the sine and cosine of the tilt angle. There is no explicit physical connection of the parameters with any current structure; thus, the zero divergence criterion is not automatically satisfied for any set of chosen parameter values. Thus, the divergence requirement was imposed by a set of linear constraints on the parameters during the least squares fitting procedure. There are 18 linear coefficients in the Tsyganenko-Usmanov magnetopause model and a single nonlinear parameter specifying the exponential decay down the tail. The Tsyganenko model contains 22 linear parameters and two nonlinear parameters. The authors assert that these terms also include average contributions of field aligned currents.

2.1.1.4.4 Model Derivation

The Tsyganenko-Usmanov data base consists of the Mead-Fairfield data set and data from the HEOS-1 and HEOS-2 spacecraft [*Hedgecock and Thomas*, 1975]. The additional data are 6248 vector averages in the radial range $6-35 R_E$. In the Tsyganenko data base, this is augmented by 11,150 similar averages from six IMP spacecraft (A, C, E, F, G, and I) in the range $-66 R_E \leq x_{GSM} \leq -15 R_E$, and 6675 averages from IMP-H and IMP-J at down-tail distances $25-45 R_E$. Apparently, this additional down tail data motivated the refined Tsyganenko tail model. Of particular note is that the additional data (in both models) do not fill in the near-Earth gap left by the Mead-Fairfield model data base. Therefore, these two models must also be suspect within $5 R_E$ of the Earth. The minimal coverage of the Tsyganenko-Usmanov data set beyond $20 R_E$ down tail defines the limit for that model. The Tsyganenko model is supplied in two versions: a long version valid to $70 R_E$, and a short version valid to $30 R_E$.

As for the Mead-Fairfield model, parameter sets are given for each of several K_p bins (11 in the Tsyganenko-Usmanov model, 6 in the Tsyganenko long version, and 8 in the Tsyganenko short version).

2.1.1.5 Stern Parabolic Magnetopause - Stretched Magnetosphere Model

The field due to the magnetopause currents is represented within this boundary as the gradient of a scalar potential satisfying Laplace's equation [*Stern*, 1985]. The requirement of a closed magnetosphere, i. e., that the field lines of the total field do not cross this boundary, leads to the condition that the normal component of the boundary field must cancel the normal component of the total field due to internal sources (dipole, ring current, etc.). Since the boundary is assumed to be parabolic, the solution is expanded in parabolic harmonics analogous to the use of spherical harmonics for problems with spherical boundaries. The axis of the boundary is the GSM axis, and its nose is at local noon. No attempt is made at a self-consistent solution of the pressure balance condition. Thus, there is no dependence of the shape on the dipole tilt.

The ring current field is modeled with the Tsyganenko-Usmanov expression. The total field due to the dipole and cross-tail currents is simulated by a stretched magnetosphere model [*Stern*, 1987]. The field at any point is represented in terms of the dipole field at some other location, specified by a stretching function. Both the stretched dipole and ring current fields are accounted for in the boundary conditions. The solution for the pure dipole has a simple scaling property with respect to pure linear scaling of the boundary. The ring current solution has a similar property, if the dimension of the ring current is also scaled.

2.1.1.5.1 Model Derivation

The basic quiet magnetopause paraboloid is determined by the requirements that the noon equatorial crossing distance (standoff distance) be $10 R_E$, and the dawn and dusk equatorial crossing distances be $15 R_E$ which are consistent with observations [*Fairfield*, 1971]. The expansion for the tail field scalar potential is truncated to 10 terms. The dependence of the magnetopause field on standoff distance is derived by assuming that the dimensions of the magnetopause vary linearly with the standoff distance, and then, using the above-mentioned linear scaling property of the field.

For the ring current, there is no specification of parameters. We have assumed strength parameter $B_0 = -20\text{nT}$ and length parameter (ρ_0)=4 R_E . The stretch function is a spline fit of a tabulation generated by the author and is designed to fit night side equatorial observations of *Fairfield* [1968].

2.1.2 Computation Times

Table 3 lists the VAX 8650 computation time per 10000 subroutine calls for the various external models and the IGRF85 internal model. The table shows that the time for a total internal + external model calculation is not terribly sensitive to the choice of external model, unless the external model is Stern's. Most of the Stern model computation time is in the magnetopause part, which requires generation of Bessel functions for the parabolic harmonic expansions. The Bessel functions were computed with routines from *Press, et. al.* [1986].

Table 3. Vax 8650 Computation Times (sec/10000 calls)

Olson-Pfizer Tilt Dependent	2.0
Olson-Pfizer Dynamic	5.2
Mead-Fairfield	0.3
Tsyganenko-Usmanov	1.8
Tsyganenko Short Version	3.0
Tsyganenko Long Version	3.6
Stern Parabolic Magnetopause/Stretched Magnetosphere	12.0
IGRF85	9.2

2.1.3 L Parameter Comparisons

As explained by *Jordan and Bass* [1990], the McIlwain L parameter [*McIlwain*, 1961], at a point, is a function of the first two adiabatic invariants of particles mirroring at that point provided the magnetic field is static. For internal fields, we may consider this to be true, if we neglect the slow secular change known to be taking place. In Figures 33 and 34, we show $\Delta L = L - L_d$, where L_d is the dipole L parameter, $r/\sin^2\theta$, with θ the magnetic colatitude and r the radial distance of the point in R_E .

In the figures, we show contours of constant ΔL for the IGRF85 model, updated to 1 January 1990. The individual contour plots are at designated values of L_d , and are on magnetic latitude-local time grids. The dipole tilt is zero, meaning that the dipole vector is normal to the Earth-sun line, and the solar magnetic longitude (SLON) is zero. The contours cover only locations above the surface of the Earth. Thus, as L_d increases, the amount of latitude space covered increases.

Near the equator ΔL is less than 0.1 but it exceeds this value in the South Atlantic Anomaly and at high latitudes. As L_d increases, $\Delta L = 1$ contours appear at the high latitudes, which were below the surface at lower L_d . One remarkable feature that appears is that a contour is nearly stationary beyond the L_d threshold for its appearance; thus, ΔL is approximately independent of L_d .

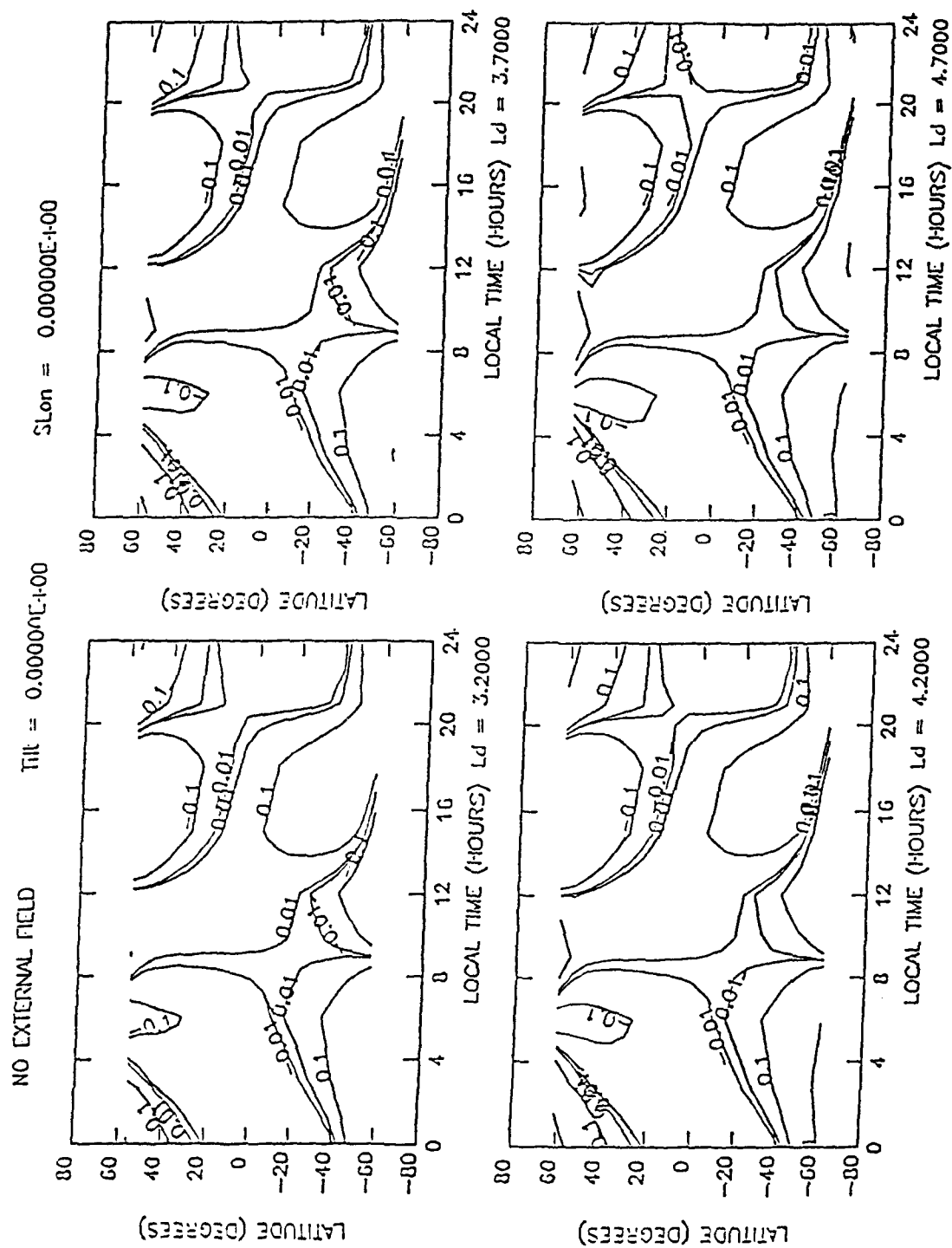


Figure 33. Contours of constant $\Delta L = L - L_d$: internal magnetic field; $L_d = 3.2, 3.7, 4.2$, and 4.7 .

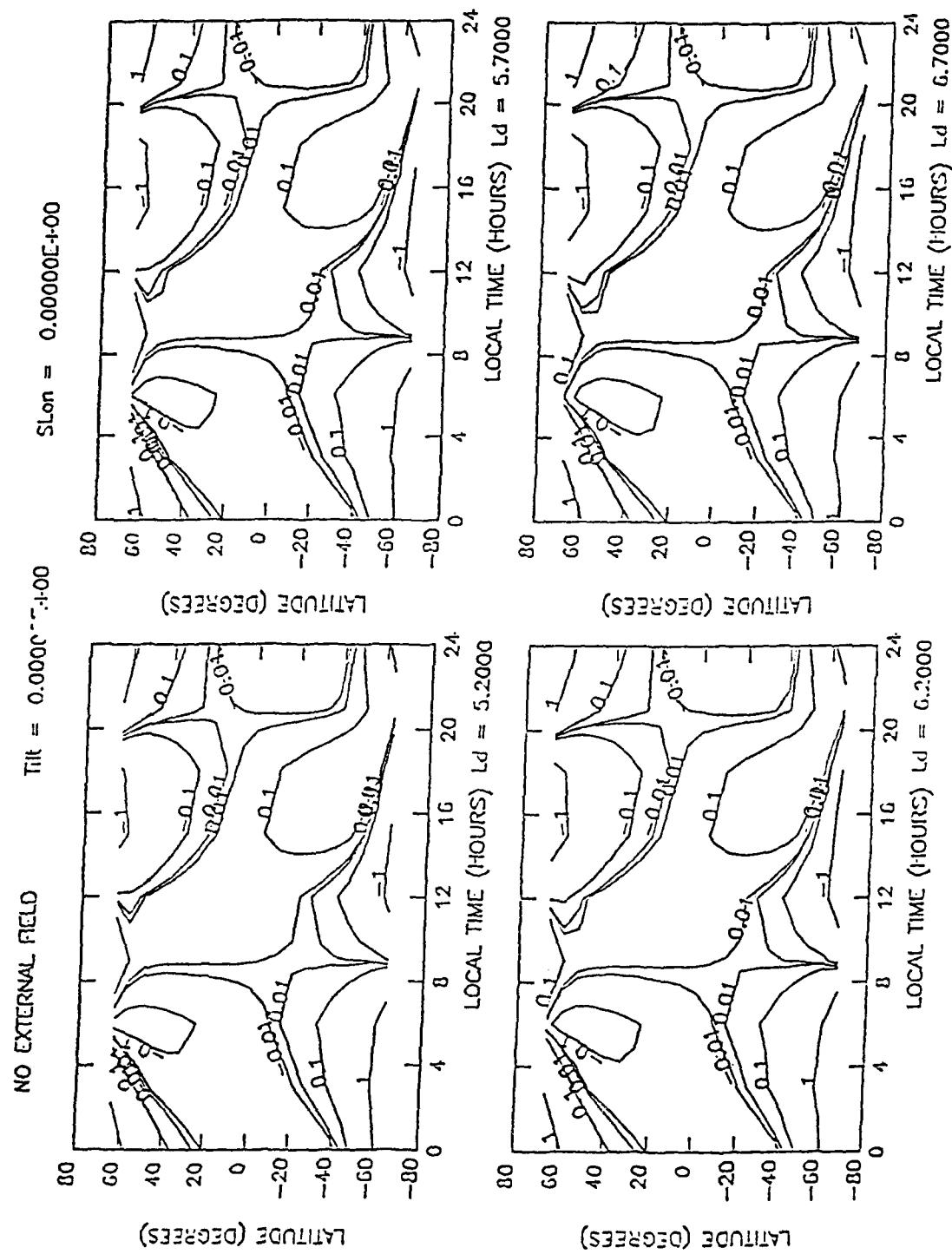


Figure 34. Same as Figure 33, but for $L_d = 5.2, 5.7, 6.2$, and 6.7.

Figures 35 and 36 similarly display ΔL for a field composed of the IGRF85 internal model and the Olson-Pfizer tilt dependent external model. In Figure 36, we have marked the local minima and maxima with "L" and "H", respectively, indicating their values. Now, as L_d increases, the contour pattern begins to deviate substantially from the IGRF85 baseline. At high L_d , there is a large area around the sub-solar point with $\Delta L < -1$, and a corresponding area around the anti-solar point with $\Delta L > 1$.

To examine this effect further, and in particular, to more easily compare the models, we have plotted, in Figures 37 and 38, ΔL vs L_d at 0° and 20° dipole latitude, respectively, for both noon and midnight, and for 0° and 18° dipole tilt. The latitudes and radial range were chosen to reflect the planned CRRES orbital parameter ranges. We compare in these figures the IGRF85 model alone ("NO Ext", solid line) with results obtained for IGRF85 + Tsyanenko-Usmanov, Tsyanenko short version ("Tsyg" 1987), Mead-Fairfield, and Olson-Pfizer tilt-dependent models. The constant and very low ΔL for the internal model alone is in agreement with what was observed in the contours plots. One readily sees the growing effect of the external models as L_d increases. A radiation belt particle which mirrors at the equator (equatorial pitch angle = 90°) must follow a path of constant L . At noon the $L=L_d$ path is outside the $L_d = \text{constant}$ circle by approximately the amount shown in the noon plot. Thus, at noon, the $L=7$ path is approximately $0.5 R_E$ outside the $L_d=7$ circle. At midnight, nearly the opposite is true: the $L=7$ path is inside the $L_d=7$ circle. Thus, a trapped particle, conserving its adiabatic invariants and mirroring at the equator, travels a path significantly distorted from a circular path.

The differences between the models is up to $0.25 R_E$ in the high L_d region of the plots. The Olson-Pfizer tilt-dependent model yields the largest L values in the inner region, while the Mead-Fairfield model gives the largest values in the outer region at noon, and the Tsyanenko and Tsyanenko-Usmanov models yield the largest values at midnight. The Olson-Pfizer midnight L increases nearly linearly with distance, while the L values for the other models increase more rapidly in the outer region than in the inner region. The dependence of the L value on dipole tilt is negligible at the equator, but significant at 20° latitude. Thus, we see that there are substantial modifications in the trapped particle orbits when the external field is introduced and noticeable differences between various models of the external field. Thus, it is worthwhile to compare the models with observations.

2.1.4 Models vs. Data

A static radiation belt model will require a good static magnetic field model. Therefore, we have chosen SCATHA magnetometer data from the magnetically quiet 20 April 1979 for comparison with the models. Despite the quiet condition, the solar wind pressure increased steadily during the period, allowing us to test the magnetopause modeling capabilities of the various models. The following day, there was a small substorm, during which, the measured magnetic field magnitude decreased considerably from the prediction of the static Olson-Pfizer tilt dependent model. If we wish to model adiabatic variations of the radiation belt particles during such substorms, we need to have an accurate model of the magnetic field variations.

Since the SCATHA orbit is limited to the outer belt, we also examined some published AMPTE/CCE results [Fairfield, et. al., 1987]. As argued by these authors, the inner magnetic flux has a bearing on the equatorial crossings of magnetic field lines intersecting the Earth's surface at given latitudes. The flux intersecting the surface equatorward of a field line in a specified longitudinal sector is approximately

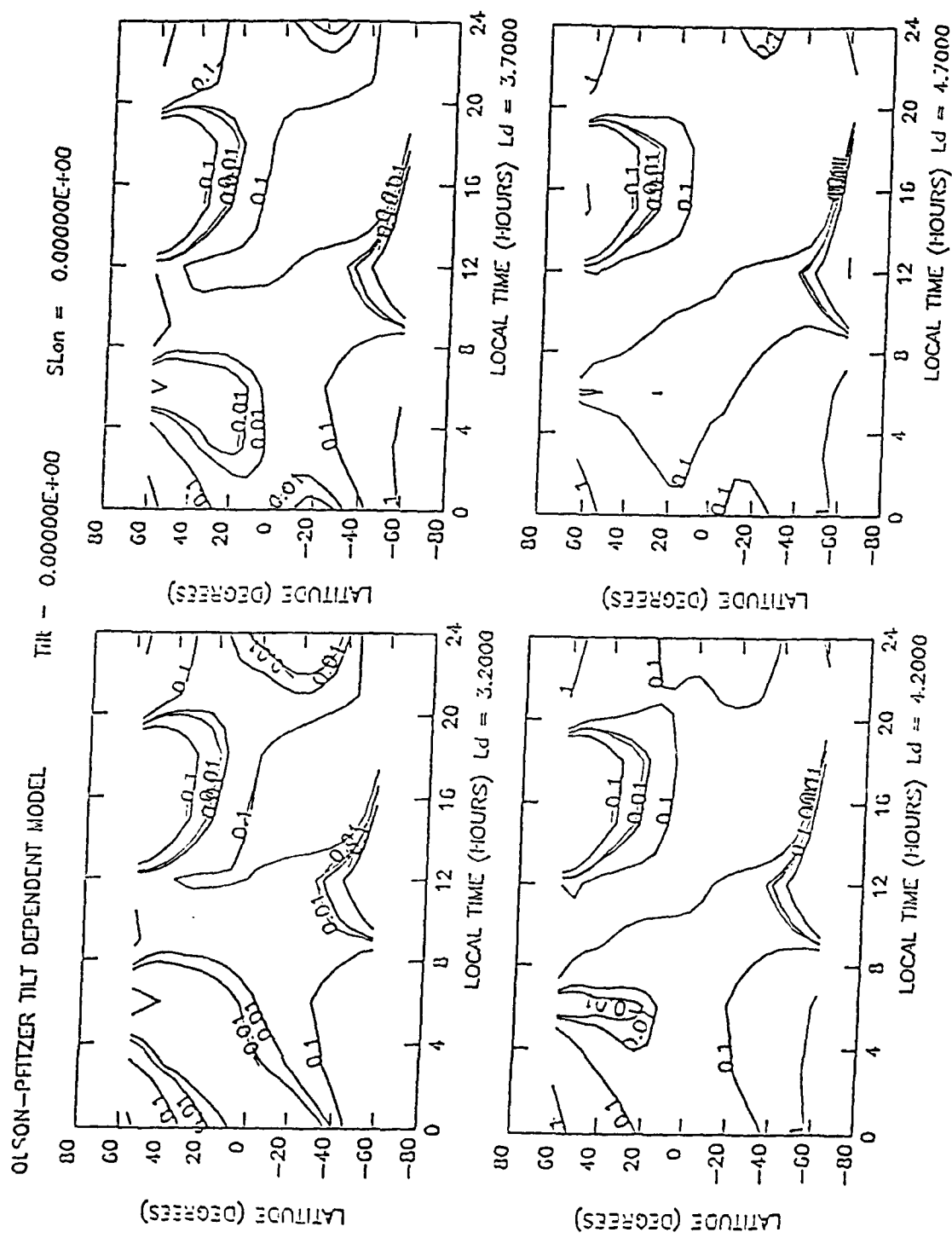


Figure 35. Same as Figure 33, but for internal model + Olson-Pfitzner tilt dependent external model.

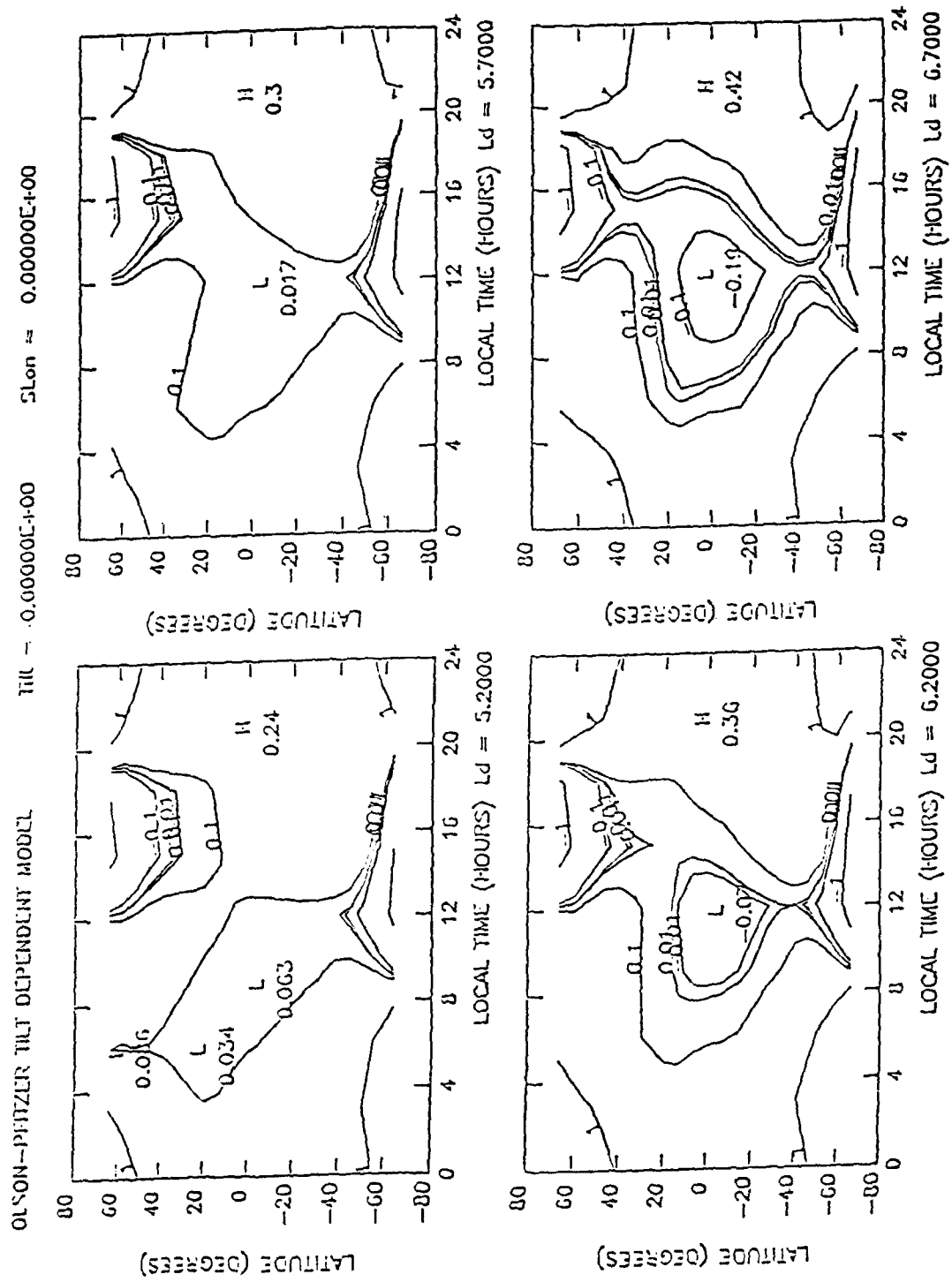


Figure 36. Same as Figure 35, but for $L_d = 5.2, 5.7, 6.2$, and 6.7 .

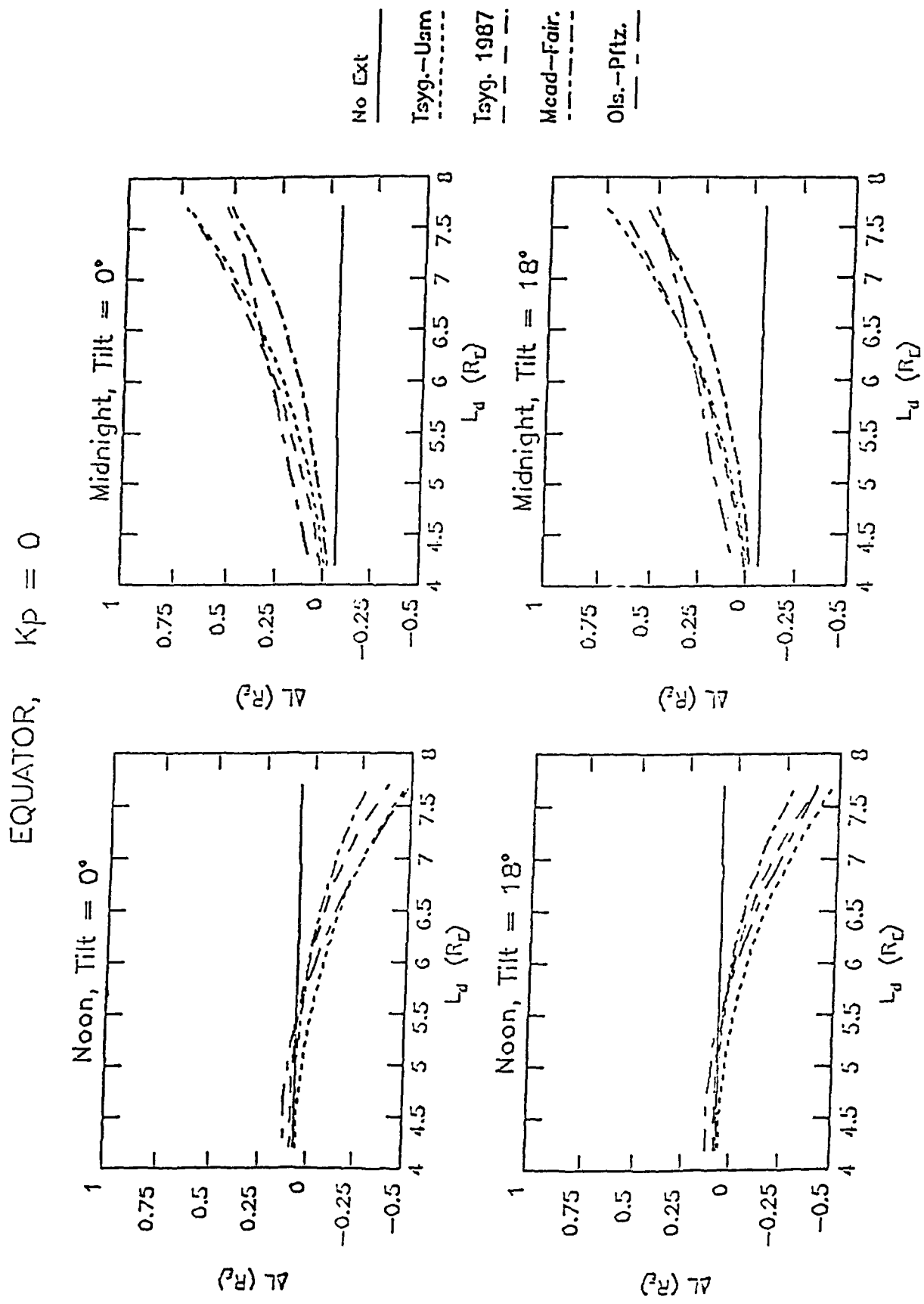


Figure 37. Noon and midnight equatorial ΔL profiles for $K_p = 0$.

Latitude = 20° , $K_p = 0$

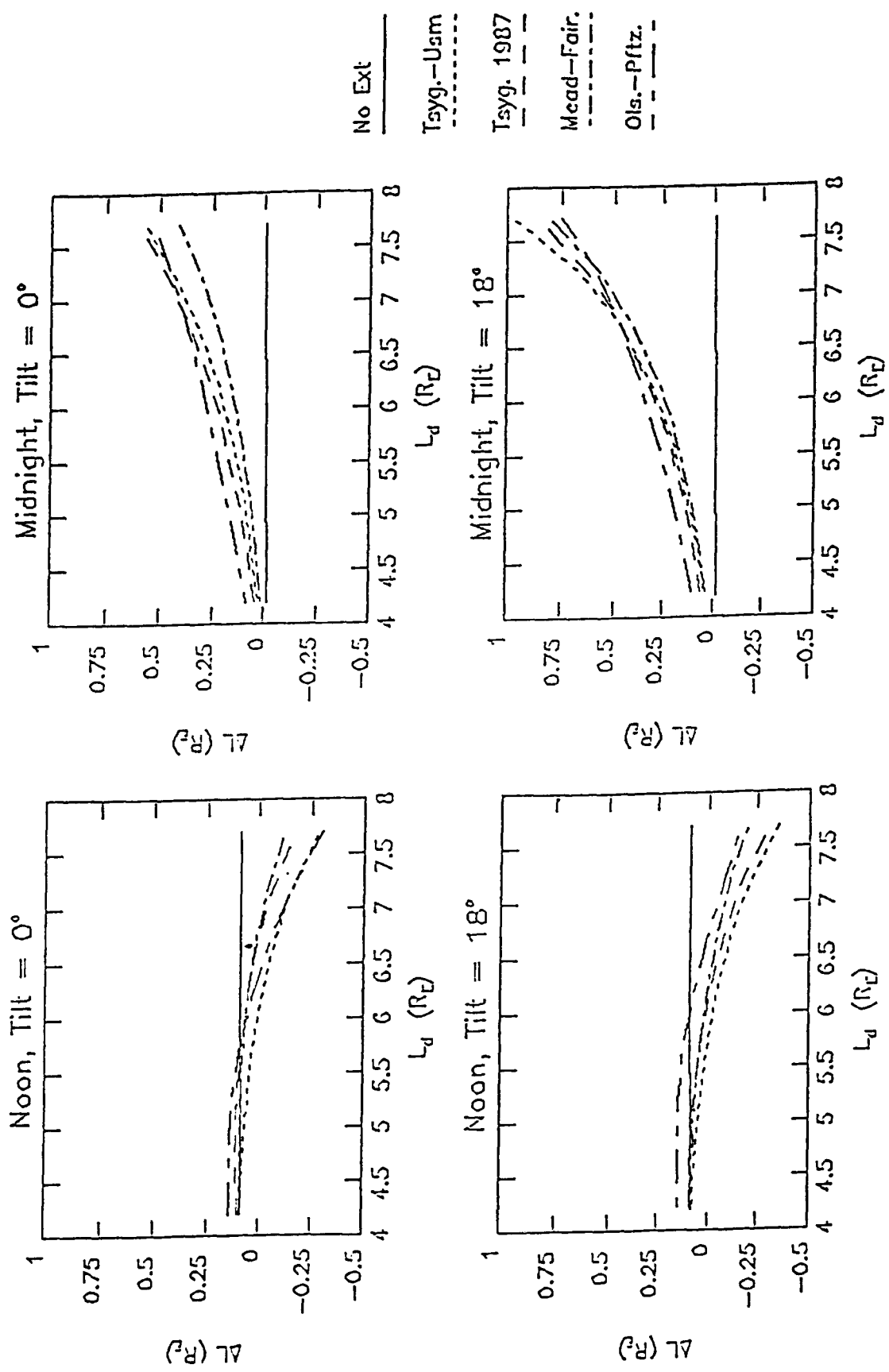


Figure 38. Same as Figure 37, but for 20° N magnetic latitude.

equal to the flux intersecting the equator in the same sector Earthward of the equatorial intersection of the field line.

2.1.4.1 Comparisons of Models with SCATHA Data

The SCATHA satellite orbit is a $5.3 R_E \times 7.8 R_E$ low inclination (7.9°) near-geosynchronous orbit with an easterly drift rate of about 5° per day. On 20 April 1979, the perigee of the SCATHA orbit was at 1600 hours MLT, the apogee was at 0300 hours MLT, and the magnetic latitude was within $\pm 4.5^\circ$. The magnetometer data used in the following were averaged over $1/20 R_E$ bins (~ 15 min.).

Figure 39 shows the differences between the measured and modeled fields for this day. The internal field model used is the Barraclough 1975, updated to the date in question.

Of all the models, the Stern model disagrees the most with the data, while the Olson-Pfitzer dynamic model agreement is generally the best, particularly at perigee, where the differences are greatest. With the exception of the Stern and Olson-Pfitzer dynamic models, the differences at the end of the day, as the next perigee is approached, are positive but opposite in sign from the differences at the beginning of the day at the same location in the orbit. Thus, the field seems to have increased over the 24 hour period relative to the models. In fact, the standoff distance implied by the solar wind data decreased steadily during the day (Figure 40). Thus, it appears that the Olson-dynamic and the Stern models, with their explicit dependence on the standoff distance, depict this variation better than do the other models.

The comparatively large deviations of the Stern model are not surprising since that model has not been extensively fit to data. The large negative deviations for the day local times (meaning the model field intensity exceeds the measured) could possibly be improved by increasing the ring current but this would worsen the disagreement of opposite sign at night local times. The stretch function evidently overestimates field line stretching for this case of extremely low activity.

Figure 41 shows the measured model magnetic field differences for the next day, 21 April 1979. On that day, a substorm occurred with growth phase commencing at ~ 5 hours UT. The measured magnetic field is seen to decrease significantly with respect to all the models. Initially the Olson-Pfitzer dynamic model seems to follow the data marginally better than the other models, but that may only be because it uses hourly indices, while the other dynamic models use the 3-hourly K_p . Thus, later on, the others are doing just as well. The start of the substorm is indicated by the sharp drop in the measured minus Olson-Pfitzer static model difference (solid line) at ~ 4-5 hours UT. During this period, the measured minus Olson-Pfitzer dynamic model difference (dotted line) actually increases, meaning that the dynamic model depicted a faster decrease than was observed. Later, however, the Olson-Pfitzer dynamic model is almost as far off the data as the others. During subsequent disturbances on that day, no model does outstandingly well.

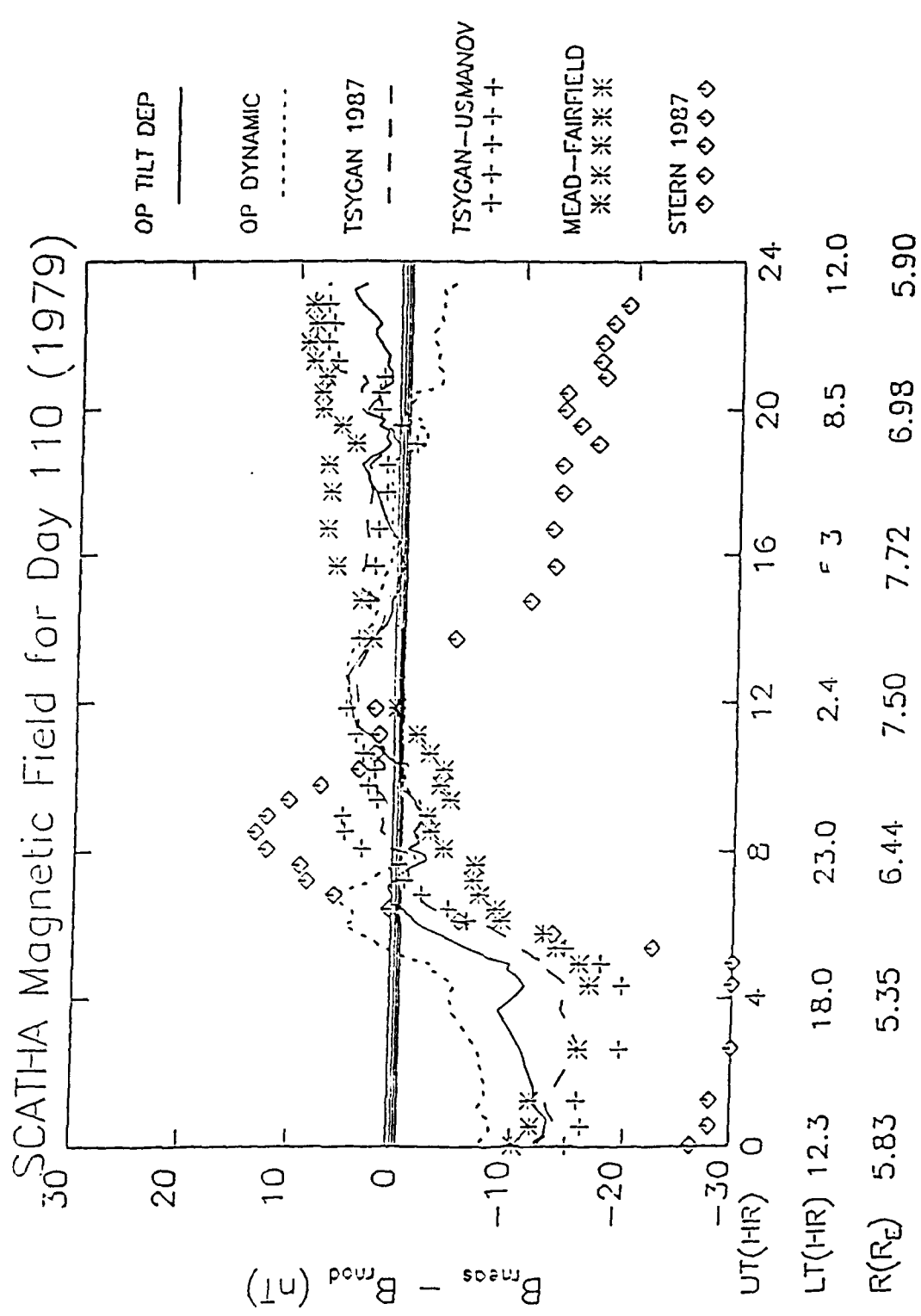


Figure 39. Measured - model differences: 20 April 1979.

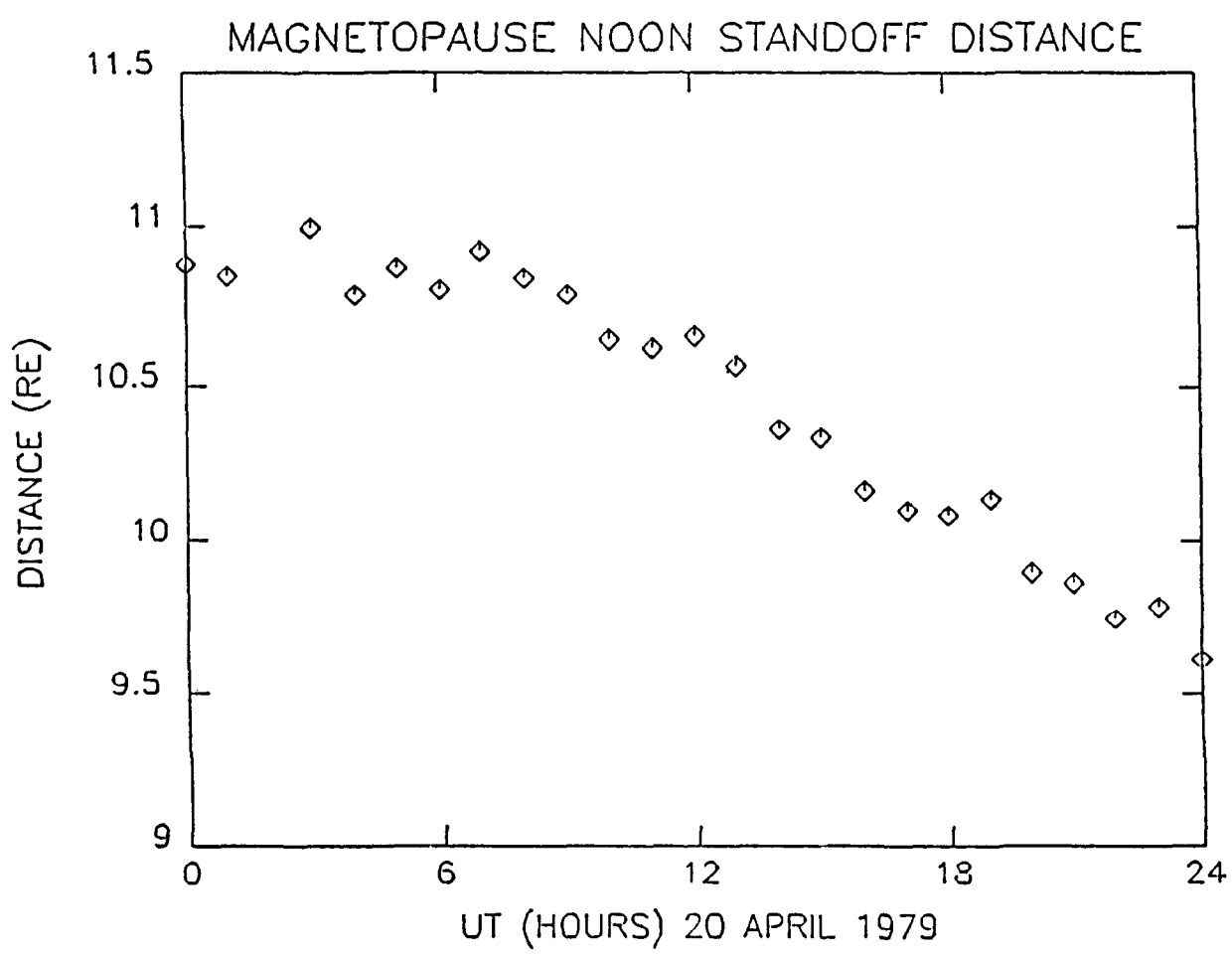


Figure 40. Noon magnetopause standoff distance: 20 April 1979.

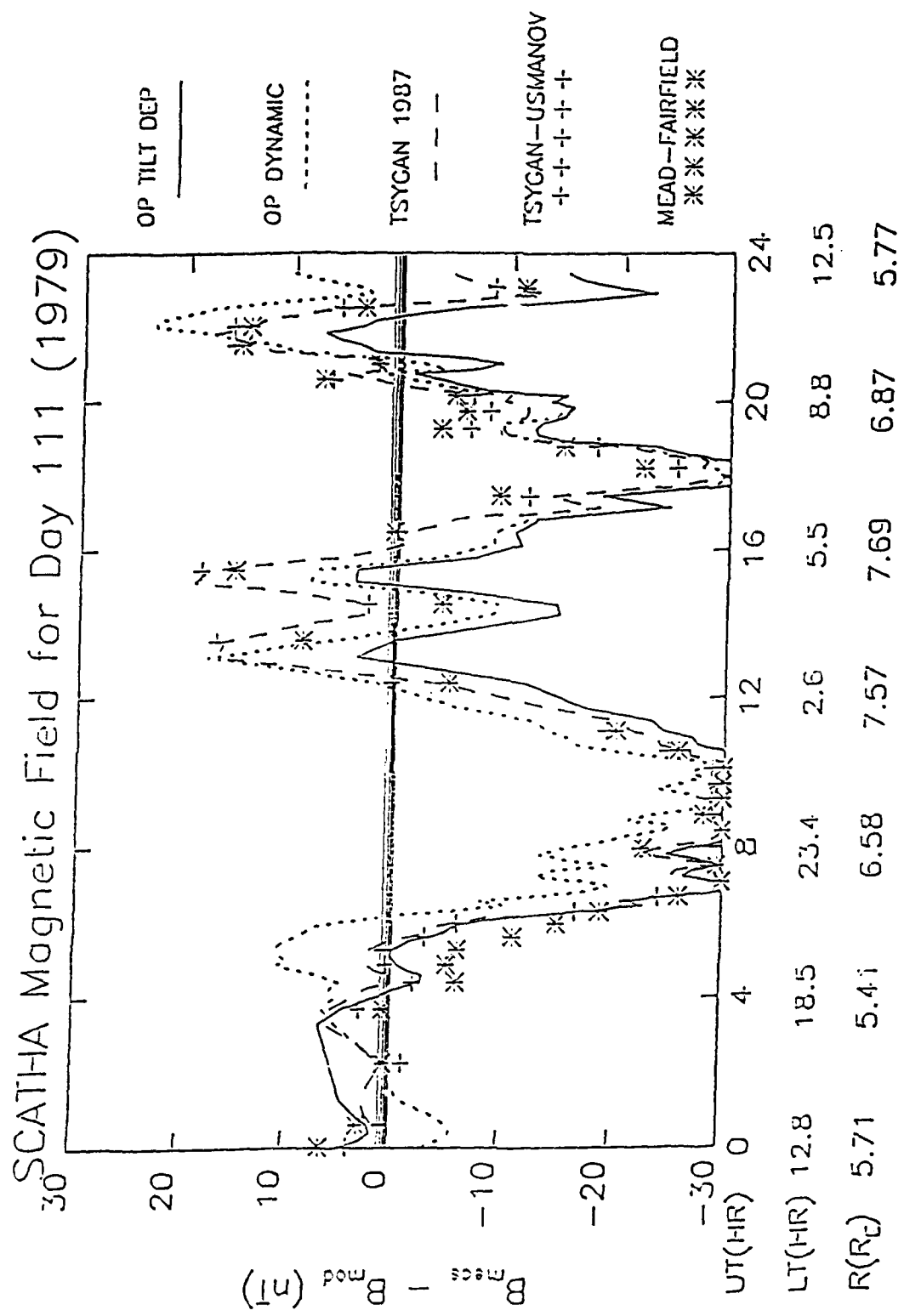


Figure 41. Same as Figure 39, but for 21 April 1979.

2.1.4.2 Midnight Equatorial Field Strength Depression

One important feature of the magnetic field is the variation of the field magnitude along the equator in the noon-midnight plane. On the midnight side, the external sources generally cause a depression in the total field strength, stretching tailward the field lines connected to given locations on the Earth's surface. Therefore, as pointed out by *Fairfield, et. al.* [1987], the magnetic mapping of given points on the Earth's surface to the equator is determined by the amount of this depression. Thus, an accurate model of the midnight equatorial depression is needed to relate auroral observations, such as precipitation boundaries and field aligned currents, to high latitude equatorial factors, such as convection, injections, and plasma pressure gradients.

Figure 42 compares averaged observed equatorial midnight field depressions, adopted from *Fairfield, et. al.* [1987], for various K_p bins with those predicted by the models. The 0-1 bin and the 2-3 bin are from *Sugiura and Poros* [1973], based on OGO measurements, while the results for the other two bins were determined by *Fairfield, et. al.* [1987] from the AMPTE/CCE data. According to the latter authors, some differences in the processing of the data may have led to differences in the high K_p results for the two satellites at the larger distances; however, the smaller distance values seem consistent.

For each model the quantity plotted is

$$\Delta B = |B_{\text{dip}} + B_{\text{ext}}| - |B_{\text{dip}}| \quad (28)$$

for zero dipole tilt. The Olson-Pfizer tilt-dependent model is presented only for the $K_p = 0\text{-}1$ bin. For the Mead-Fairfield, Tsyganenko-Usmanov, and Tsyganenko 1987 short models, we chose bins as close to those of the data as the binning structure of the individual models permitted. Thus, the Mead-Fairfield model is specified for 4 bins. Of these, only two, $K_p < 2$ and $K_p \geq 3$ were sufficiently comparable to the data bins. For the Tsyganenko-Usmanov and Tsyganenko 1987 models, the results were obtained by weighted averaging of appropriately selected model bins; the number of observations in each such bin, given by the authors, determined the weighting factor for that bin.

For the Olson-Pfizer model, the mean standoff distance and D_{st} value for each K_p bin were determined from 1983 data on the NSSDC OMNI online data base. These are given in Table 4. In the Stern model, as for the Olson-Pfizer tilt dependent model, only a single set of results is given.

Table 4. Average Values for the Olson-Pfizer Dynamic Model

K_p	Standoff Distance	D_{st}	No. of points
0-1	9.680	-1.1	440
0-2-	9.601	-2.3	819
2-3	9.091	-7.9	1098
$\geq 3+$	8.514	-28.0	1262

MIDNIGHT EQUATORIAL DEPRESSION

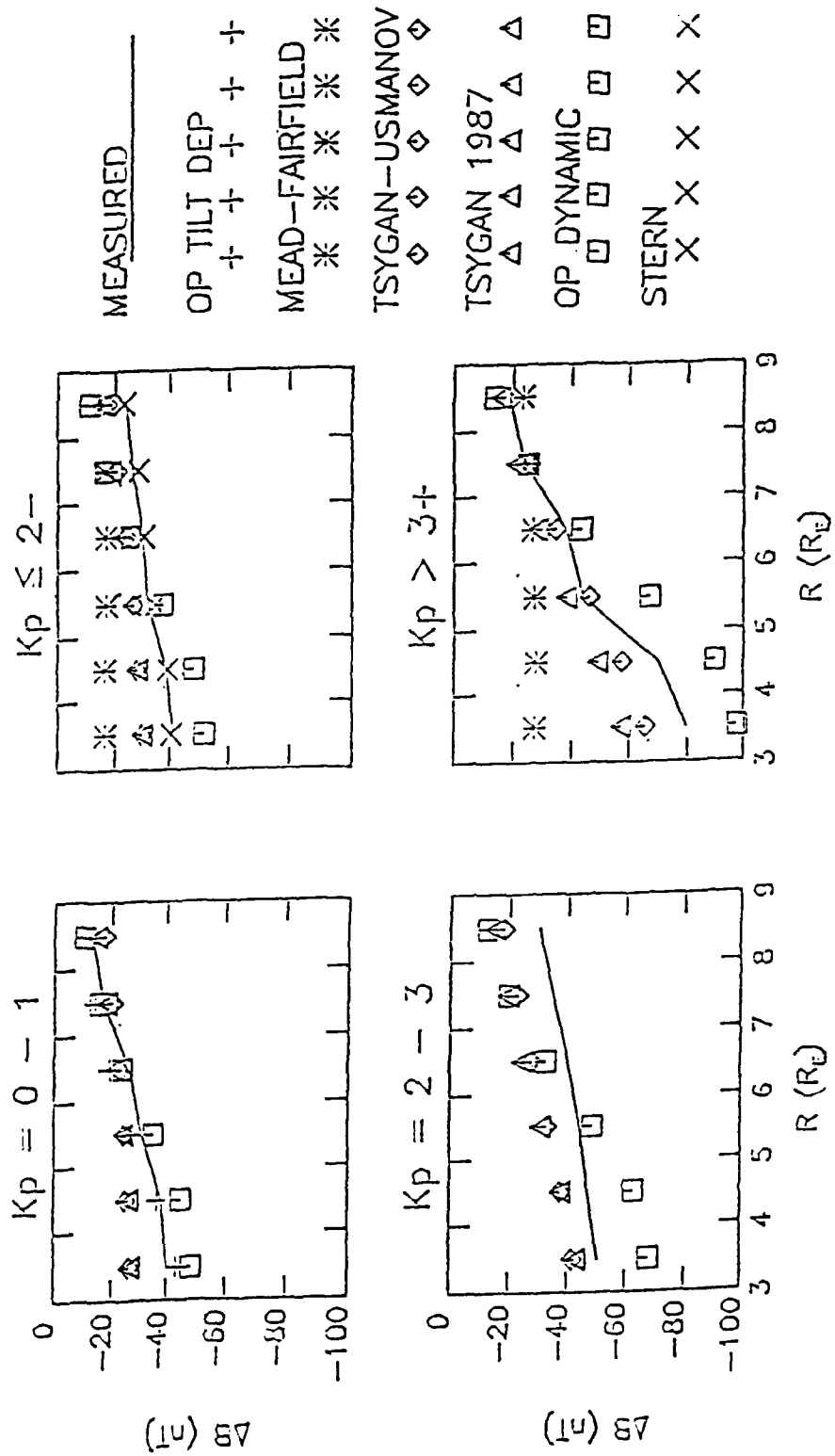


Figure 42. Averaged measured [Fairfield, et. al., 1987] and model midnight equatorial magnetic field depression. The K_p - 0-1 and 2-3 measurements are from OGO data, the $K_p \leq 2$ and $K_p \geq 3+$ measurements are from AMPTE data.

The Olson-Pfizer tilt-dependent model agrees quite well with the measurements for the low K_p bin. This is not surprising, as this model is also derived from OGO data. The Mead-Fairfield, Tsyganenko-Usmanov, and Tsyganenko models all predict depressions smaller than the data at smaller distances. The K_p dependence in the Mead-Fairfield model is nearly constant with distance, while in the other two models the K_p dependence decreases with increasing distance, in apparent contrast with the data. The disagreement at small distances is probably due to the lack of equatorial data at these distances in the data sets used to derive these models. The Olson-Pfizer dynamic model exhibits considerably greater depression than the data. Like the Tsyganenko-Usmanov and Tsyganenko model depressions, that for the Olson-Pfizer dynamic model exhibits decreasing K_p dependence with increasing distance. The Stern model seems to fit the $K_p \leq 2$ - measured depression, which is not too surprising, as Stern's dipole stretch model is based on data averaged over all geomagnetic activity levels.

2.1.5 Summary

Six models of the external magnetospheric field have been reviewed. The purpose of these models is to provide accurate and computationally efficient evaluation of the contribution to the magnetospheric magnetic field due to external sources, for use in analysis and interpretation of magnetospheric data.

Their properties were examined in the $3-8 R_E$ range, that portion of the CRRES orbit where the external field is expected to be important. An external field typically modifies the L parameter beyond $4 R_E$. The dependence of L on the dipole tilt is small along the dipole equator, but significant at higher latitudes.

For a magnetically quiet period, the magnetic field magnitudes derived from all the models agree closely with that derived from SCATHA magnetometer observations over that period. Upon closer review, it was found that the Olson-Pfizer dynamic model tracks the data the best, since its magnetopause model depends explicitly on the standoff distance. Stern's model, although its magnetopause model is also tied to the standoff distance, showed the poorest agreement with the data, possibly because its magnetopause model is purely theoretical, and its tail field, implied by the stretch model, is too large (and negative) on the night side and identically zero on the day side. During a substorm on the following day, none of the models predict the large drop in the field magnitude that is seen by the data, although several of the models show a very small decrease.

For zero tilt, the Stern and Olson-Pfizer tilt-dependent model-calculated equatorial midnight field depressions are consistent with averaged AMPTE and OGO measurements as functions of distance. The Olson-Pfizer dynamic model predicts larger depressions than observed, while the other dynamic models predict smaller depressions.

2.2 Models Published in 1989 or Later

2.2.1 Tsyganenko 1989 Model

After an initial study of the available external magnetospheric magnetic field models, we found two new models which had not been covered: Tsyganenko 1989 and Hilmer-Voigt. Thus, a subsequent study was performed to better evaluate these models along with the Olson-Pfizer Dynamic (1988) model. In fact, two similar studies were performed, the first was a comparison to SCATHA data (20 and 21 April 1979) and the second, a comparison to CRRES data (26 August 1990). Tsyganenko 1989 started with an axisymmetric infinitely thin current disk for the tail current. He transformed the disk to allow for hinging (where the tail current bends away from the dipole equatorial plane in the near Earth region to become parallel to the plasma sheet in the GSM x-y plane). Also, the disk was modified to allow for transverse bending in the y-direction. Factors were added to drop off smoothly as the magnetopause was approached. The ring current is represented by the second derivative of the axisymmetric infinitely thin current disk to better confine its contribution to the field. Only westward current was represented. There is no magnetopause. There is no inner edge to the current sheet. No data was included inside of four R_E . Thus, this model is not really intended for use in the inner magnetosphere. Finally, the data was binned by K_p and fit accordingly. Thus, this is an average model of the field within each K_p bin. As such, we found it to be in relatively good agreement with the data. It is not suited for looking at dynamic changes in the data, such as the compression of the field as the solar wind pressure increases and the magnetopause moves in. Nor can it resolve fine scale activity (K_p is only available as three hour averages). However, as an average model, it did reasonably well in comparison to both our quiet time and early storm time data (Figures 43 and 44). It's fast and very easy to use.

2.2.2 Hilmer-Voigt Model

Hilmer-Voigt is driven by four physical input parameters: dipole tilt, stand-off distance of the magnetopause, activity index Dst, and the midnight equatorward boundary of the diffuse aurora. Considering all of the models that we have looked at, this is the most flexible. The magnetopause is represented by Voigt's 1981 shielded vacuum dipole model with a fixed shape of a hemisphere attached to a cylinder. The ring current is represented by a vector potential similar to that used by Tsyganenko 1987, but Hilmer's expression includes eastward travelling current. The tail current is based on a method used by Tsyganenko and Usmanov which uses magnetic filaments extending infinitely in y. The filaments are grouped in segments. Transverse bending and hinging are included. The stand-off distance determines the strength of the magnetopause currents, Dst controls the ring current, and the midnight equatorward boundary maps to the inner edge of the tail current sheet.

Therefore, this model is the most flexible in rendering the dynamic changes of the magnetosphere. However, it is also the slowest and most difficult to use. The four input parameters are used to find intermediate parameters which are actually required to run the model. Until very recently, this input parameter selection code was not available, so one had to contact Hilmer to get the necessary parameters to run his code for a given configuration of the field. We now have a preliminary release of this intermediate code to work with and test. Nonetheless, this model agreed best with the data overall (Figures 43 and 44). It is not really suitable for heavy data processing, but is very useful for modeling dynamic change on a fairly small scale.

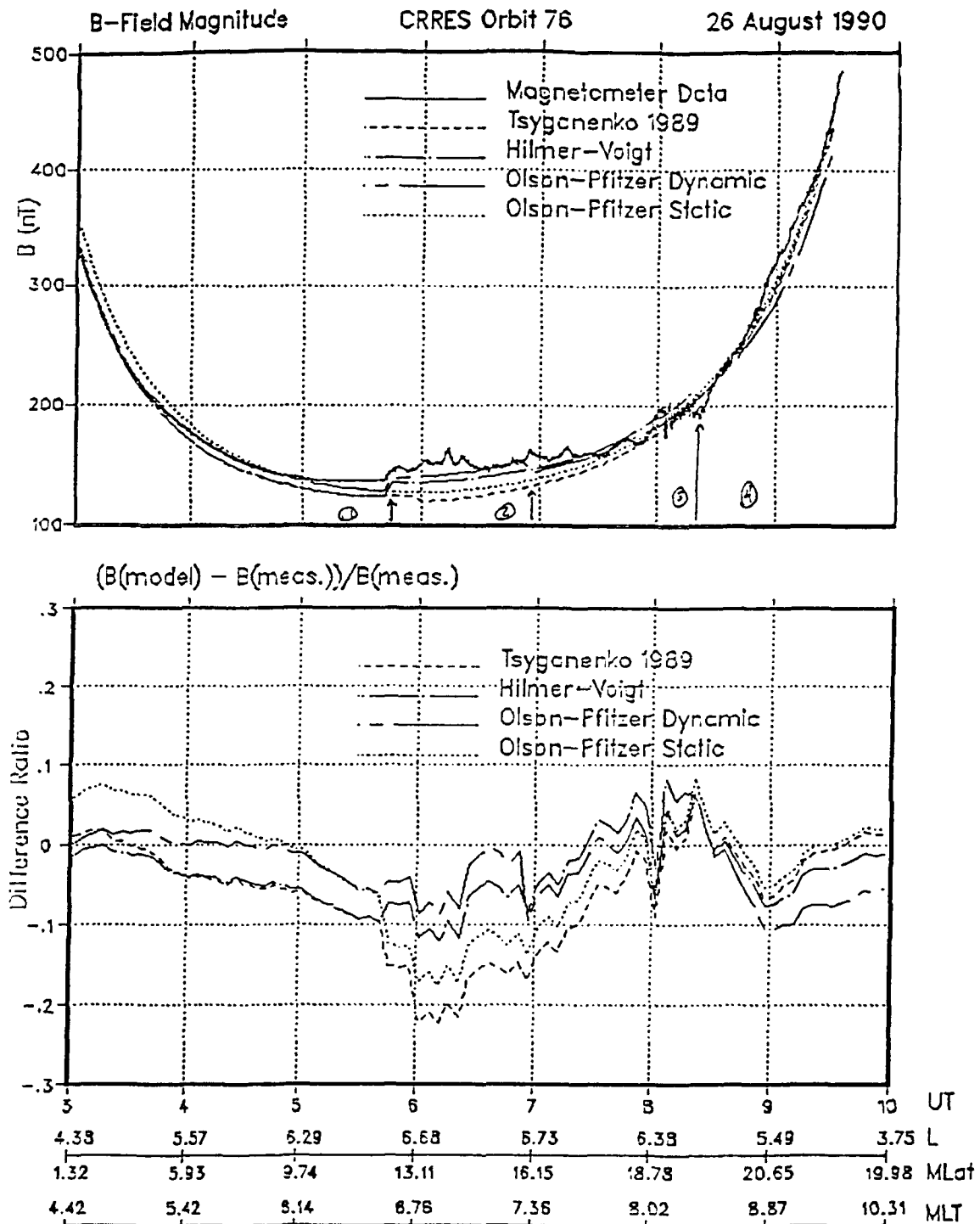


Figure 43. This is a sample of a preliminary comparison of these models to CRRES data. The top panels show the data and model $|B|$ for part of 26 August 1990. The bottom panel shows the difference ratios seen between the models and data for $|B|$.

Angle Between Model And Measured Vectors CRRES Orbit 76 26 August 1990

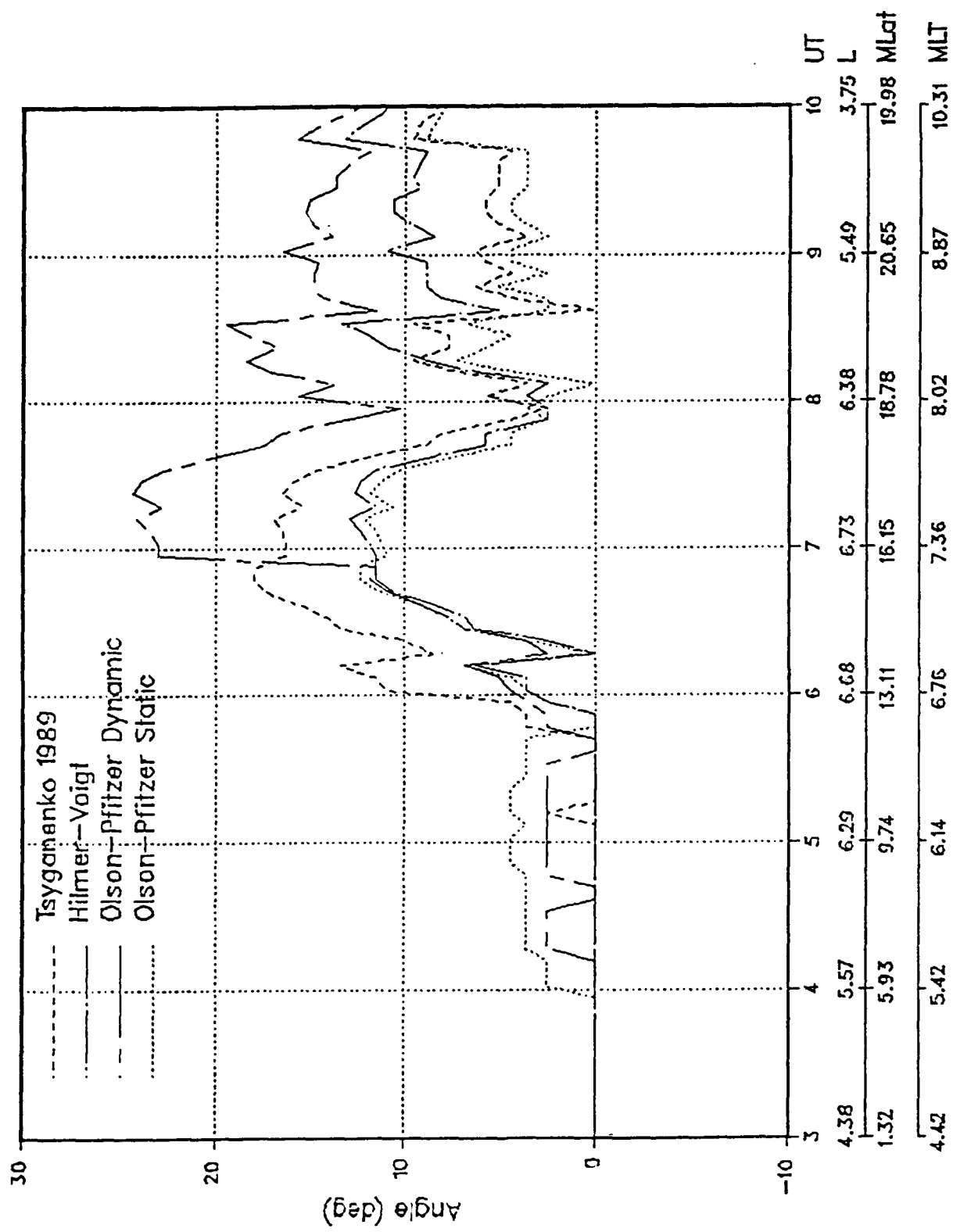


Figure 44. The angle between the CRRES magnetometer measured field vectors and the model field vectors for part of 26 August 1990.

2.3 References

- Behannon, K. W., "Mapping of the Earth's Bow Shock and Magnetic Tail by Explorer 33", *J. Geophys. Res.*, Vol. 73, Pp. 907-930, 1968.
- Behannon, K. W., "Geometry of the Geomagnetic Tail", *J. Geophys. Res.*, Vol. 75, P. 743, 1970.
- Fairfield, D. H., "Average Magnetic Field Configuration of the Outer Magnetosphere", *J. Geophys. Res.*, Vol. 73, Pp. 7329-7338, 1968.
- Fairfield, D. H., "Bow Shock Associated Waves Observed in the Far Upstream Interplanetary Medium", *J. Geophys. Res.*, Vol. 74, Pp. 3541-3553, 1969.
- Fairfield, D. H., "Average and Unusual Locations of the Earth's Magnetopause and Bow Shock", *J. Geophys. Res.*, Vol. 76, Pp. 6700-6716, 1971.
- Fairfield, D. H., "Whistler Waves Upstream from Collisionless Shocks", *J. Geophys. Res.*, Vol. 79, Pp. 1368-1378, 1974.
- Fairfield, D. H., and Ness, N. F., "Configuration of the Geomagnetic Tail During Substorms", *J. Geophys. Res.*, Vol. 75, Pp. 7032-7047, 1970.
- Fairfield, D. H., and Ness, N. F., "IMP 5 Magnetic Field Measurements in the High-Latitude Outer Magnetosphere Near the Noon Meridian", *J. Geophys. Res.*, Vol. 77, Pp. 611-623, 1972.
- Fairfield, D. H., Acuna, M. H., Zanetti, L. J., and Potemra, T. A., "The Magnetic Field of the Equatorial Magnetotail: AMPTE/CCE Observations at $R < 8.8 R_E$ ", *J. Geophys. Res.*, Vol. 92, No. A7, Pp. 7432-7442, 1987.
- Hedgecock, P. C., and Thomas, B. T., HEOS Observations of the Configuration of the Magnetosphere", *Geophys. J. R. Astr. Soc.*, Vol. 41, P. 391, 1975.
- Jordan, C. E., and Bass, J. N., "Evaluation of Magnetospheric Internal Magnetic Field Models and Existing Software", GL-TR-90-0014, January 1990, ADA221816.
- McIlwain, C. E., "Coordinates for Mapping the Distribution of Magnetically Trapped Particles", *J. Geophys. Res.*, Vol. 66, No. 11, Pp. 3681-3691, 1961.
- Mead, G. D., and Fairfield, D. H., "A Quantitative Magnetospheric Model Derived from Spacecraft Magnetometer Data", *J. Geophys. Res.*, Vol. 80, No. 4, Pp. 523-534, 1975.
- Meng, C. I., and Mihalov, J. D., "Average Plasma Sheet Configuration at 60 Earth Radii", *J. Geophys. Res.*, Vol. 77, P. 1739, 1972.
- Mihalov, J. D., Colburn, D. S., Currie, R. G., and Sonett, C. P., "Configuration and Reconnection of the Geomagnetic Tail", *J. Geophys. Res.*, Vol. 73, P. 943, 1968.

Murayama, T., "Spatial Distribution of Energetic Electrons in the Geomagnetic Tail", *J. Geophys. Res.*, Vol. 71, Pp. 5547-5557, 1966.

Olson, W. P., "The Shape of the Tilted Magnetopause", *J. Geophys. Res.*, Vol. 74, No. 24, Pp. 5642-5651, 1969.

Olson, W. P., "A Model of the Distributed Magnetospheric Currents", *J. Geophys. Res.*, Vol. 79, No. 25, Pp. 3731-3738, 1974.

Olson, W. P., and Pfitzer, K. A., "A Quantitative Model of the Magnetospheric Magnetic Field", *J. Geophys. Res.*, Vol. 79, No. 25, Pp. 3739-3748, 1974.

Olson, W. P., and Pfitzer, K. A., "Magnetospheric Magnetic Field Modeling", Annual Scientific Report, AFOSR Contract No. F44620-75-C-0033, McDonnell Douglas Astronautics Company, Huntington Beach, CA, 1977.

Olson, W. P., and Pfitzer, K. A., "A Dynamic Model of the Magnetospheric Magnetic and Electric Fields for July 29, 1977", *J. Geophys. Res.*, Vol. 87, No. A8, Pp. 5493-5498, 1982.

Pfitzer, K. A., Olson, W. P., and Mogstad, T., "A Time Dependent, Source Driven Magnetospheric Magnetic Field Model", *EOS*, Vo. 69, No. 16, P. 426, 1988.

Press, W. H., Flannery, B. P., Teukolsky, S. A., and Vetterling, W. T., "Numerical Recipes: The Art of Scientific Computing", Cambridge University Press, Cambridge/New York/New Rochelle/Melbourne/Sydney, 1986.

Russell, C. T., "Geophysical Coordinate Transformations", *Cosmic Electrodynamics*, Vol. 2, Pp. 184-196, 1971.

Speiser, T. W., and Ness, N. F., "The Neutral Sheet in the Geomagnetic Tail: Its Motion, Equivalent Currents, and Field Line Connection Through It", *J. Geophys. Res.*, Vol. 72, Pp. 131-141, 1967.

Stern, D. P., "Representation of Magnetic Fields in Space", *Rev. Geophys. and Space Phys.*, Vol. 14, No. 2, Pp. 199-214, 1976.

Stern, D. P., "Parabolic Harmonics in Magnetospheric Modeling: The Main Dipole and the Ring Current", *J. Geophys. Res.*, Vol. 90, No. A11, Pp. 10,851-10,863, 1985.

Stern, D. P., "Tail Modeling in a Stretched Magnetosphere 1. Methods and Transformations", *J. Geophys. Res.*, Vol. 92, No. A5, Pp. 4437-4448, 1987.

Sugiura, M., Ledley, B. G., Skillman, T. L., and Heppner, J. P., "Magnetic Field Distortions Observed by OGO 3 and 5", *J. Geophys. Res.*, Vol. 67, P. 7552, 1971.

Sugiura, M., and Poros, D. J., "A Magnetospheric Field Model Incorporating the OGO 3 and 5 Magnetic Field Observations", *Planet. Space Sci.*, Vol. 21, Pp. 1763-1773, 1973.

Tsyganenko, N. A., "Global Quantitative Models of the Geomagnetic Field in the Cislunar Magnetosphere for Different Disturbance Levels", *Planet. Space Sci.*, Vol. 35, No. 11, Pp. 1347- 1358, 1987.

Tsyganenko, N. A., and Usmanov, A. V., "Determination of the Magnetospheric Current System Parameters and Development of Experimental Geomagnetic Field Models Based on Data from IMP and HEOS Satellites", *Planet. Space Sci.*, Vol. 30, No. 10, Pp. 985-998, 1982.

3.0 EPHemeris STUDIES

3.1 Magnetic Latitude and Local Time at Bmin

Along a field line in the trapped radiation belts, there exists a point of minimum magnetic field strength. All particles bouncing along the field line must pass through this minimum. Thus, all trapped particles in the radiation belt must pass through this surface of minima which we often refer to as BMIN. Therefore, from a model of the trapped populations along this surface, it is possible, in principle, to derive the populations at all other points. In practice, however, such a derivation requires the determination of the BMIN location and properties as a function of time and position. This requires that we find the intersection of the field line through the starting position with the BMIN surface. Since straightforward field line tracing can be quite expensive computationally, we have done a survey of BMIN surface properties in the hope of finding properties that would lead to a simpler procedure.

Ideally, the BMIN surface should coincide with the dipole equator. However, it is known that at large distances in the midnight local time sector, the solar wind alters the surface significantly when the tilt of the dipole with respect to the earth-sun line differs from zero. In such cases, the dipole equator is not parallel to the solar wind. At small distances from the earth, the internal field dominates. Thus, the minimum still lies very close to the equator. As the distance increases, the solar wind forces the BMIN surface to curve away from the dipole equator, toward a surface parallel to the earth-sun line. In addition, it causes magnetic field lines to be significantly twisted in local time, so that lines emanating from the earth's surface at dawn or dusk local time are twisted toward midnight. Thus, the local time at a given CRRES location may differ from the local time at the appropriate BMIN intersection.

To study these effects with CRRES, we have constructed, from the standard ephemeris files for the first 450 orbits, a BMIN survey data base which contains for each ephemeris point:

- orbit number and time (year, day number, UT)
- solar magnetic coordinates (radial distance, latitude, local time) at CRRES
- dipole tilt
- magnetic longitude of the sun
- solar magnetic coordinates at BMIN
- magnetic field strength and L at both BMIN and CRRES

Figure 45 shows BMIN local time and orbit number for all BMIN distances greater than $7 R_E$. It shows that apogee approaches local midnight just prior to the end of this period. The maximum solar magnetic latitude magnitude on the BMIN surface was 4.2° . The maximum local CRRES-BMIN local time difference was 11 minutes. Figure 46 shows the BMIN distance and solar magnetic latitude for BMIN distances greater than $6 R_E$. Although there is a lot of variation in the data, there is a trend toward increasing northern latitude with distance. The apogee approaches midnight in midwinter, which is dominated by high negative dipole tilt. In this situation the BMIN surface curves northward of the dipole equator.

In conclusion, the solar wind does not distort the minimum B surface severely from that expected for the simple dipole model, nor does the local time vary significantly along a field line. Such variations that

1991-09-26

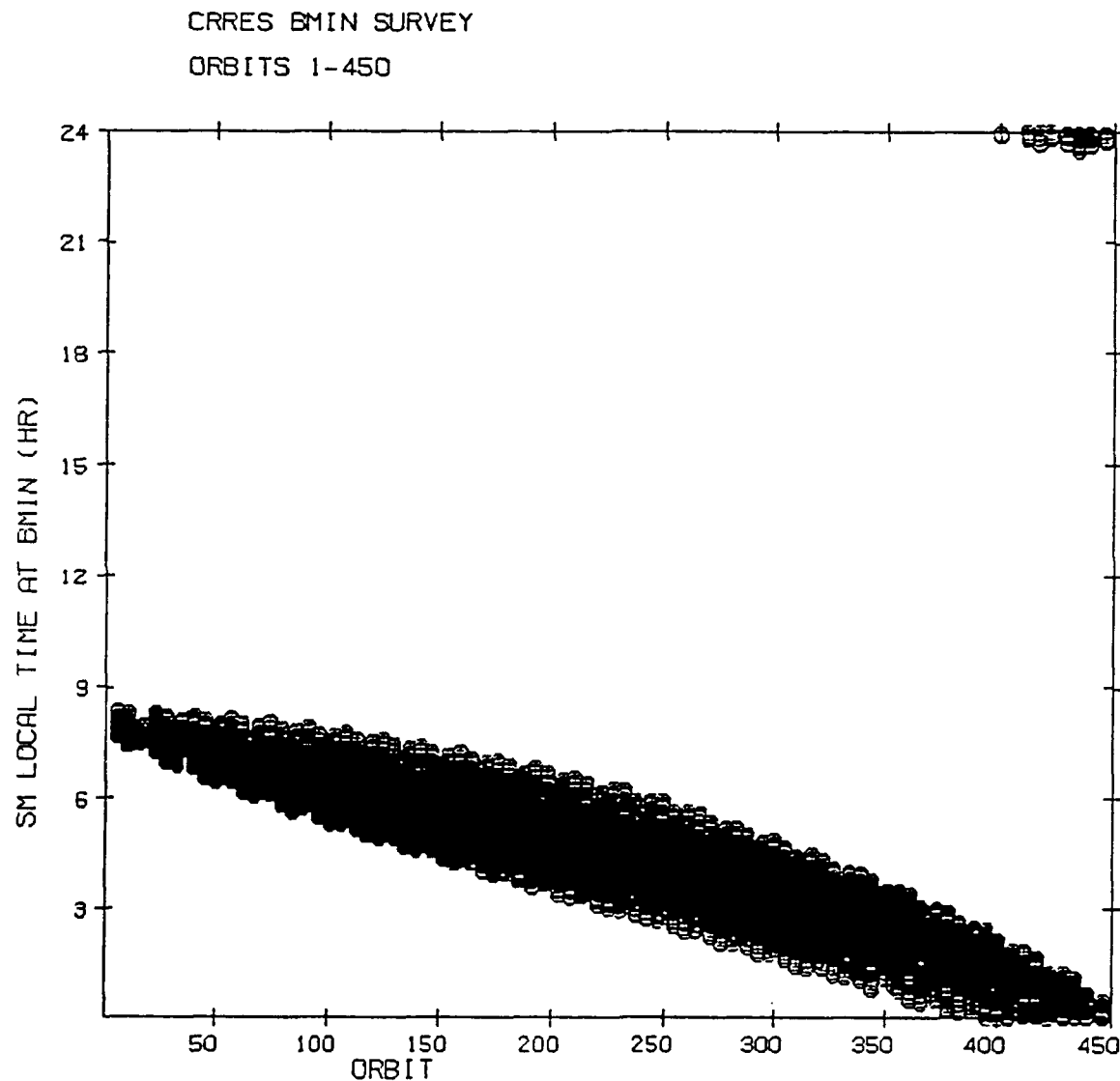


Figure 45. Solar magnetic (SM) local time and orbit number for all cases of BMIN distance greater than $7 R_E$, orbits 1 - 450.

1991-09-26

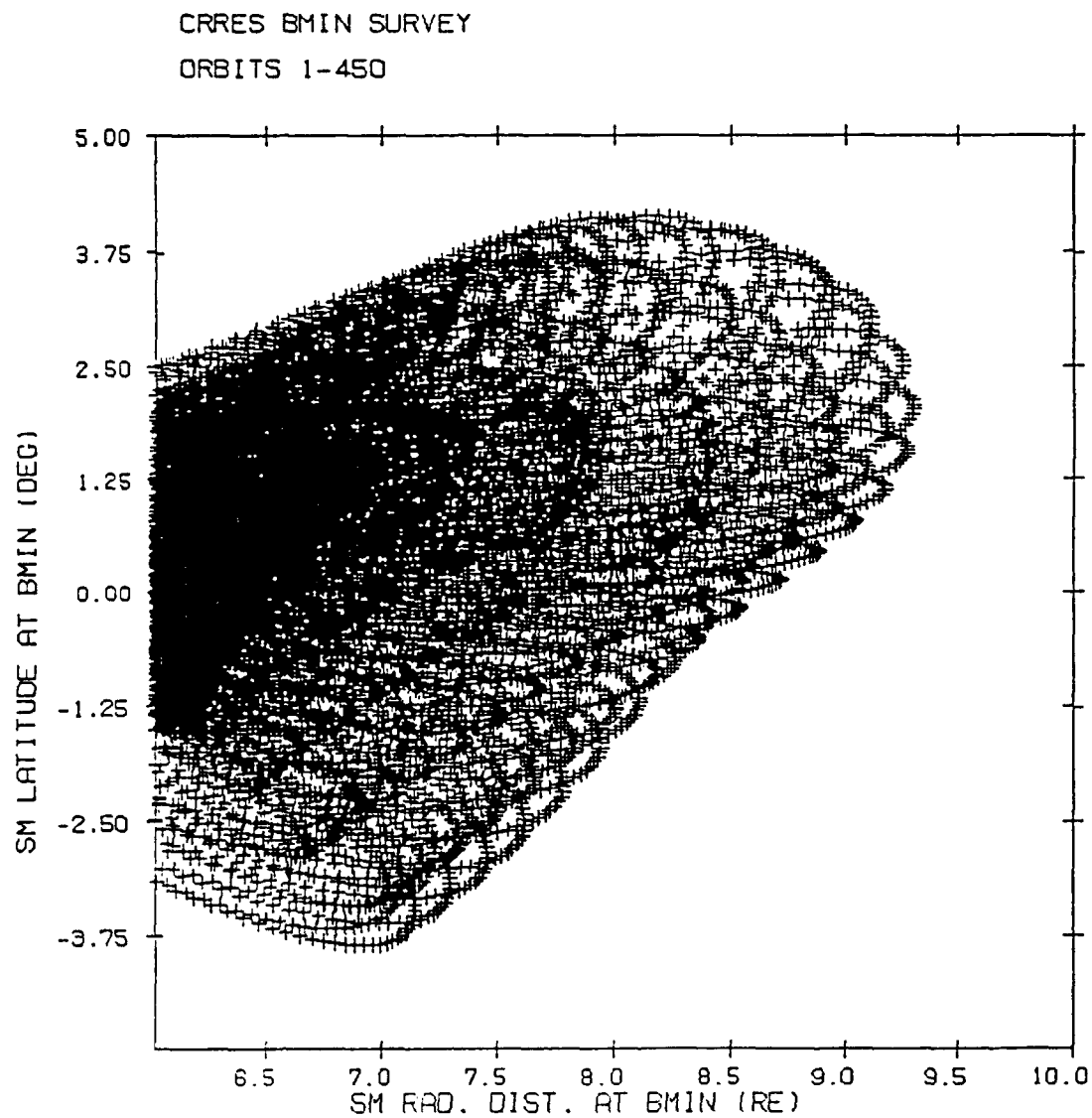


Figure 46. SM latitude and radial distance for all cases of BMIN distance greater than $6 R_E$, orbits 1 - 450.

do exist should be modeled analytically to estimate the intersection of a field line with the BMIN surface, as an alternative to direct tracing.

3.2 B/B_o vs L and Magnetic Latitude

Existing software has been modified and improved to compute the relative dwell times of a satellite for a specified range of B/B_o and L-shell values over a specified time interval. The dwell chart provides a graphical representation of the fraction (percentage) of time that a satellite will spend in a given B/B_o and L-shell interval. The data is represented either by a black and white density, or by different colors. A color Dwell Chart was produced for the CRRES satellite for a one year period using updated CRRES orbital elements.

A color Dwell Chart was produced for the CRRES satellite for a 1/2 year period (July 1990 - January 1991) for the researcher to supplement the 1 year color Dwell chart produced earlier. Software was written to produce Black and White versions of the same Dwell Charts using the HPGL graphics capabilities of the HP LaserJet III printer. Figure 47 shows the black and white version of the 1 year Dwell Chart.

Code was developed which would read the CRRES orbit database files and compute the time of L value crossings, the value of B/B_o , and the magnetic latitude (SM, GM and GSM coordinates) at the crossing times. A series of scatter plots (B/B_o vs. magnetic latitude (SM, GM and GSM)) for selected L values, were produced for orbits 1 - 510. Figure 48 is an example.

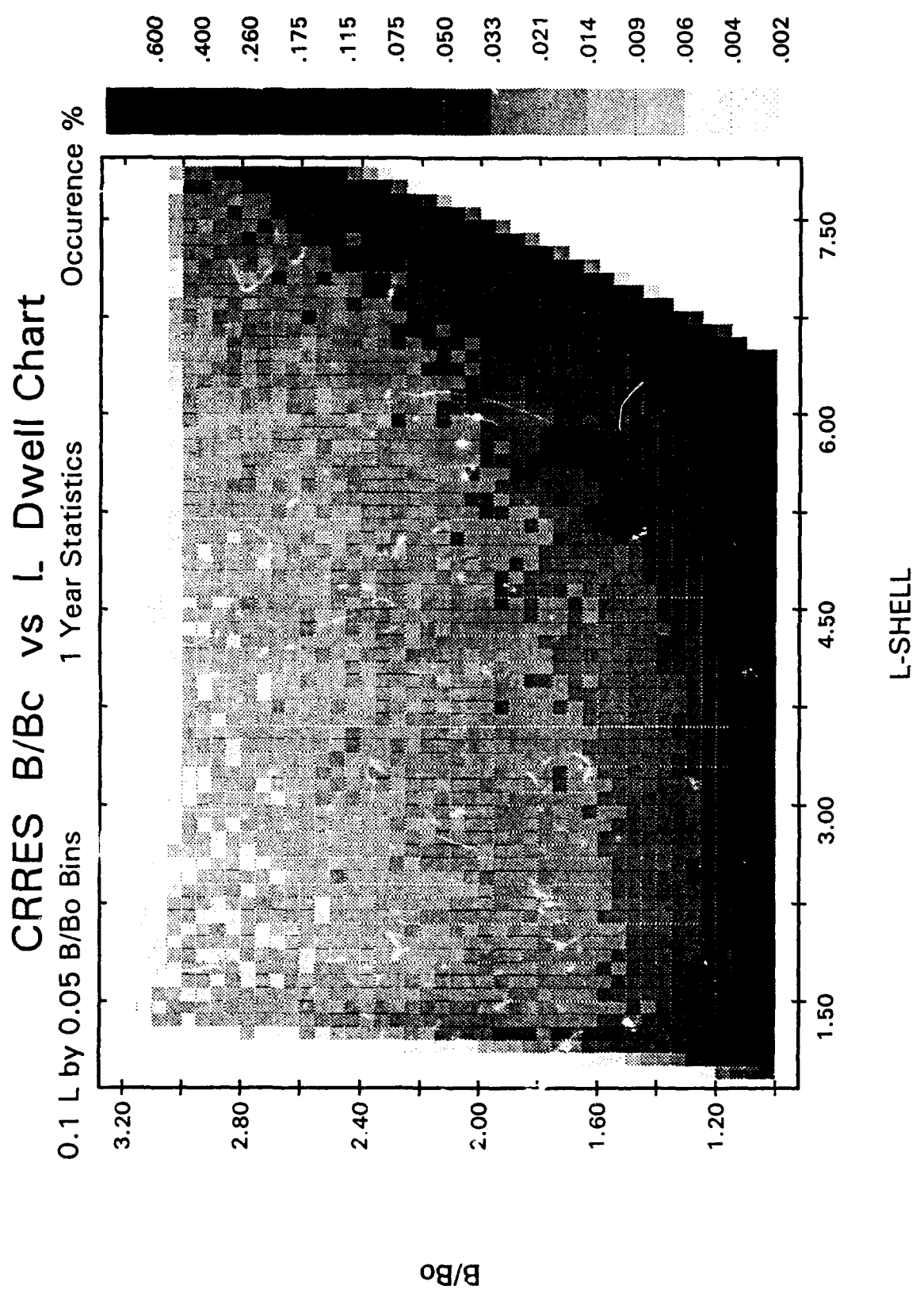


Figure 47. CRRRES B/B₀ vs. L Dwell Chart - 1 Year Statistics

B/Bo vs SMLAT Scatter Plot

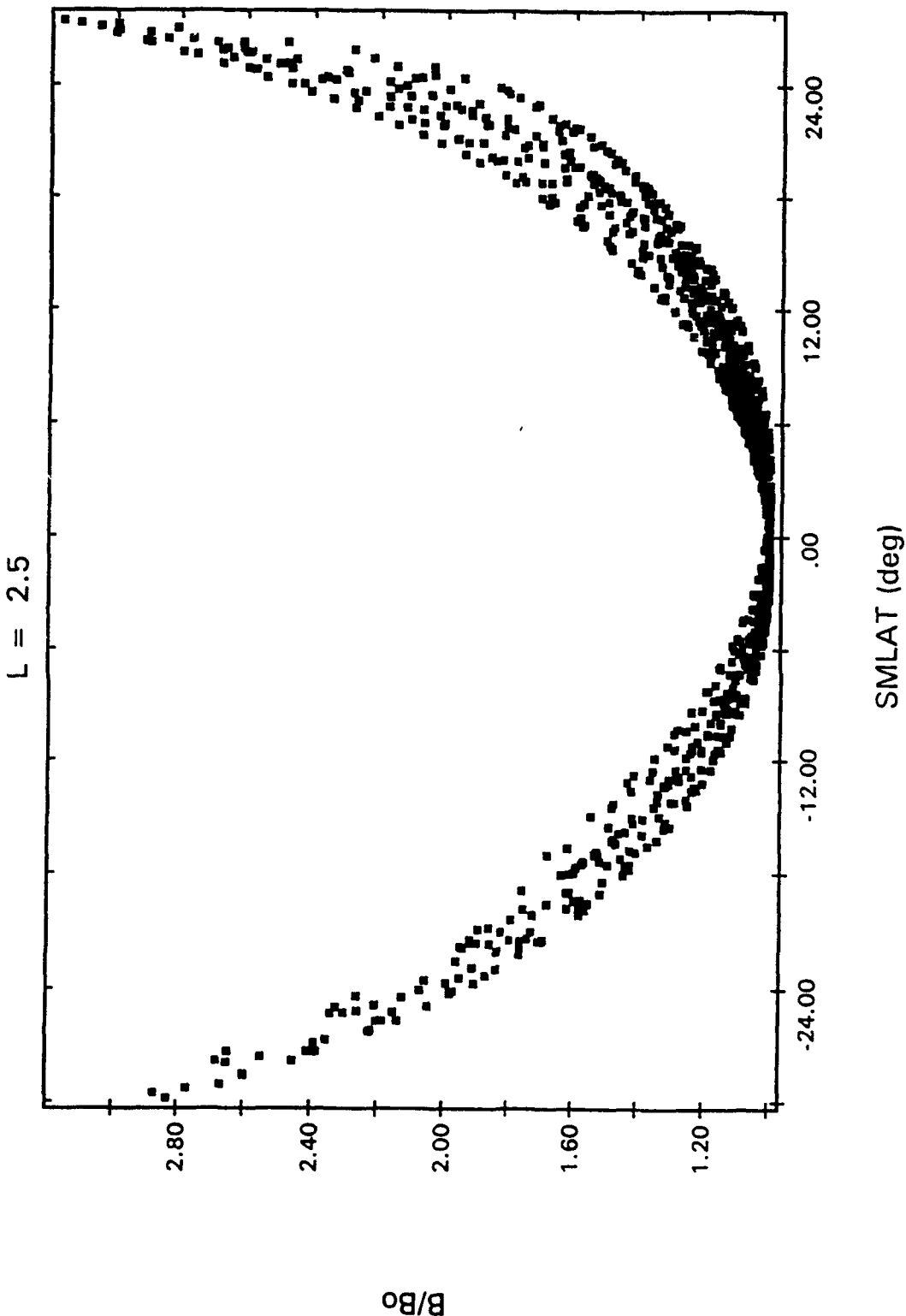


Figure 48. CRRS B/B_0 vs. Solar Magnetic Latitude at $L = 2.5$ (Orbits 1-510).

4.0 INSTRUMENT MODELING

4.1 PROTEL Contamination Code

4.1.1 Motivation

The Proton Telescope (PROTEL) is one of the instruments on the CRRES satellite. A detailed description of the PROTEL instrument is provided in a recent report [*Lynch, et al.*, 1989]. PROTEL measures proton counts in the 1 to 100 MeV energy range in the radiation belts. It consists of two detector instruments, the low energy head [LEH] (1 - 9 MeV) and the high energy head [HEH] (6 - 100 MeV), and a dedicated processor which processes the raw data from the detectors, and at 1 second intervals, transfers the reduced data to the satellite's telemetry system. The reduced data consists of counts in 24 energy channels (8 for LEH, 16 for HEH) spaced logarithmically in the 1 - 100 MeV energy interval, together with environmental data and raw counts for the solid state particle detectors.

PROTEL is designed to operate in a hostile environment, where it is subjected to a high density flux of electrons, protons and, to a lesser extent, heavier ions and cosmic radiation. The design integrates passive shielding techniques, magnetic deflection of electrons, and detection (coincidence and anticoincidence) logic which is used to eliminate spurious proton counts.

In order to properly evaluate the performance of PROTEL, it is necessary to model the behavior of the PROTEL in its hostile environment. In order to do so, it is necessary to anticipate deviations of the PROTEL instrument from its nominal design, and to identify the potential sources of errors due to limitations of the PROTEL design and due to the hostile environment. In the context of this report, contamination refers to the penetration of high energy protons from angles outside the nominal acceptance cone which falsely trigger the PROTEL detection logic, despite the use of passive shielding, consisting of aluminum, brass, iron and tungsten in the construction of the PROTEL housing.

In a recent report [*Redus, et al.*, 1990], it has been suggested that PROTEL will have problems resulting from the penetration of high energy protons from certain angles outside the entrance cone. These protons will produce false counts (contamination) in the data. The effect of contamination on observed counts will strongly depend upon the energy spectrum and angular distribution of the high energy protons. For this reason, a software package (PROTEL Contamination Code) which models the contamination problem for the HEH has been developed.

Portions of the PROTEL contamination code have been used to model the PROTEL calibration experiments which were performed using an accelerator at Harvard University. The predictions of the contamination code were compared with the Harvard experimental data. Within the limits of experimental error, the agreement between the predictions and the model appears to be satisfactory [*Hein, 1990*].

4.1.2 Methodology

The PROTEL HEH contains six solid state detectors D1-D6. D1-D5 each contain two detection areas: the first is a disk, and the second is a ring surrounding the disk. D6 has only a circular disk. Pulse height circuitry, coincidence and anti-coincidence circuitry, and logic are used to classify detection events in the several particle detectors. A detection event is recorded in one of the energy channels only if it meets the energy deposit requirements of the detectors associated with the energy channel and the requirements of the coincidence/anticoincidence logic. The ring detectors and D6 are used in connection with the anti-coincidence logic.

4.1.2.1 Physical Assumptions

The physical assumptions made in developing the PROTEL contamination code are as follows:

The primary effect is due to protons which penetrate the PROTEL housing/shielding and are decelerated in the direction of motion, while interacting with the electrons in the material through which they pass. The protons are assumed to travel in straight lines until they either are stopped by or penetrate the material they are passing through. This is a relatively good assumption for high energy protons. However, important effects are neglected, such as Coulomb scattering with the nuclei, inelastic scattering off of the nuclei, including "STARS" -- nuclear reactions which produce protons, neutrons and/or gamma rays.

These assumptions permit the modeling of contamination by means of "ray tracing" through the PROTEL HEH for particles entering from a given direction and with a given energy as described by a differential flux. The Harvard Accelerator experiments were modeled assuming that the accelerator beam was a parallel beam with little variation transverse to the direction of the beam. In the more general case, it was assumed that the energy spectrum and the angular distribution of the incident radiation are independent. A collection of representative points on the first detector is selected, together with a direction. For each point, the spectrum is computed (using the Janni energy/range relation) at the point of the first detector. A determination is then made as to which detectors the ray passes through; the corresponding energy deposited in each detector is calculated, and the corresponding channel counts are computed. The counts over the detector surface for a given direction are summed, and the sum is weighted according to the direction. The weighted channel counts are summed to obtain a total count for the input spectra.

4.1.2.2 Janni Range-Energy Tables

The Janni Range-Energy Tables [Janni, 1982] were incorporated into the PROTEL Contamination Code for the following materials: Aluminum, Brass, Iron, Tungsten (for the PROTEL HEH passive shielding and housing), Silicon (for the particle detectors) and Lucite (for the absorbers used in the Harvard accelerator experiments).

4.1.2.3 Ray Tracing of PROTEL HEH

FORTRAN Code was developed, which performed a ray trace through the different materials present in the PROTEL HEH passive shielding and housing. Careful measurements were made of the original blueprints of the different materials used in the PROTEL HEH housing and passive shielding. A

routine was developed, which computes the thicknesses of the different materials through which a proton would pass as it entered from a given direction. The routine would return arrays which identified the type of material, and the thickness encountered to an accuracy of 0.1 mm. The latter was used to compute the proton's energy loss using the Janni Range-Energy Relation.

4.1.2.4 Monte Carlo Technique

Early in the development of the Protel Contamination Code, it was discovered that the computational overhead of doing a standard (deterministic) computation was prohibitive. For the Harvard experimental data computation, only a single direction was required, and the computation effort required was reasonable. For the full contamination computation, it was desired to use Monte Carlo methods, in effect, to perform an integration. For each angular distribution of interest (isotropic, and two cases of mirror plane geometry corresponding to maximum and minimum obstruction due to the electron deflection magnet, and the $\sin^N \alpha$ pitch angle distribution) code was written in which 20,000 points on the first detector, and a direction (appropriate to the angular distribution) were randomly selected. The tracing was then performed, which provided a table of materials and thicknesses encountered for each point. The response function was then computed for proton energies ranging from 5-110 MeV at 0.1 MeV intervals, and from 110-250 MeV at 1 MeV intervals. The response function could then be used to compute the results for each angular distribution for an arbitrary energy distribution. In order to verify the sufficiency of 20,000 points, comparison runs were made using different "seeds" for the random number generation, with the result that the output agrees within a few percentage points.

4.1.3 Results

The response function for Channel 10 is provided for the isotropic case (Figure 49) and for the Mirror Plane Distribution Case (Figure 50). For the mirror plane case, two curves are provided which correspond to orientations of the mirror plane relative to the maximum (0°) and minimum (90°) obstruction due to the electron deflection magnet. Note that the effects of contamination for the mirror plane case are not as severe as that found for the isotropic case.

4.1.3.1 Harvard Accelerator Experiment

Early in the development of the PROTEL HEH Contamination Code, portions of the code were used to compute the contamination associated with the PROTEL calibration tests performed with the Harvard Cyclotron. The PROTEL instruments were placed at several different orientations at several different energies, and subject to proton beams of different energies, where the latter were obtained by using different thicknesses of lucite as a beam degrader. The PROTEL HEH mass distribution model and the Janni range - energy relation were used to compute the counts, assuming that the proton beam was parallel and uniform across the HEH. Within experimental errors of the calibration experiment and the positioning of the HEH, the agreement was reasonable.

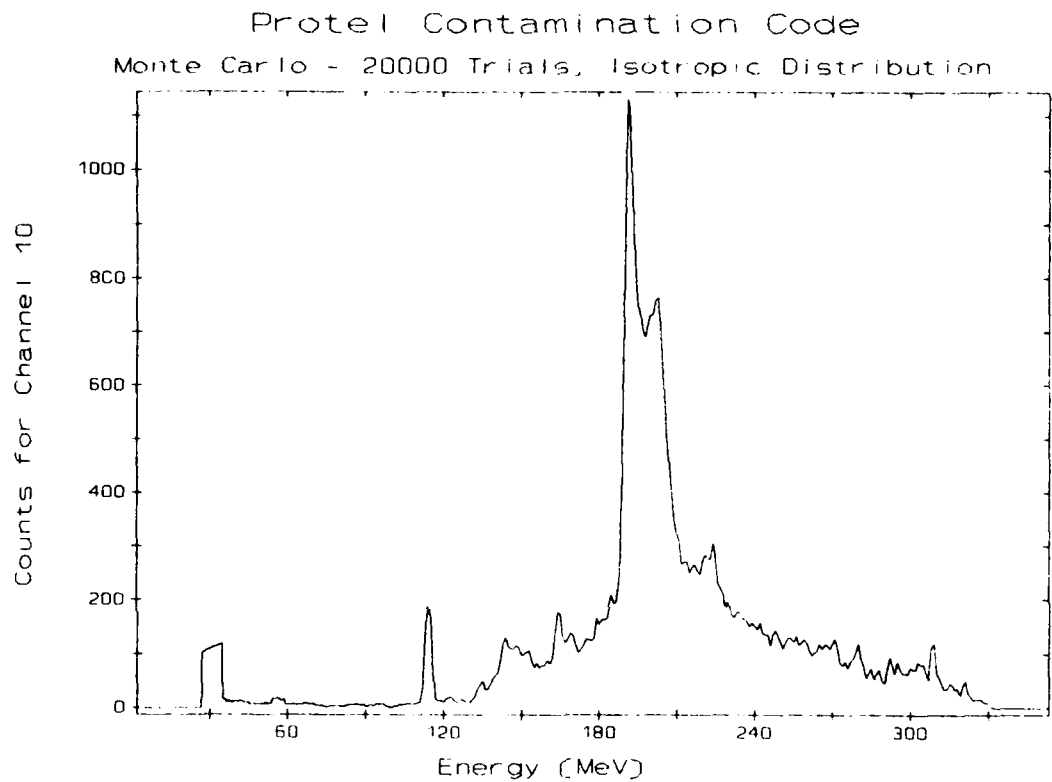


Figure 49. PROTEL HEH Response Function for the isotropic case for channel 10. The nominal response occurs near 30 MeV. The contamination is significant above 100 MeV, and corrections for contamination need to be made.

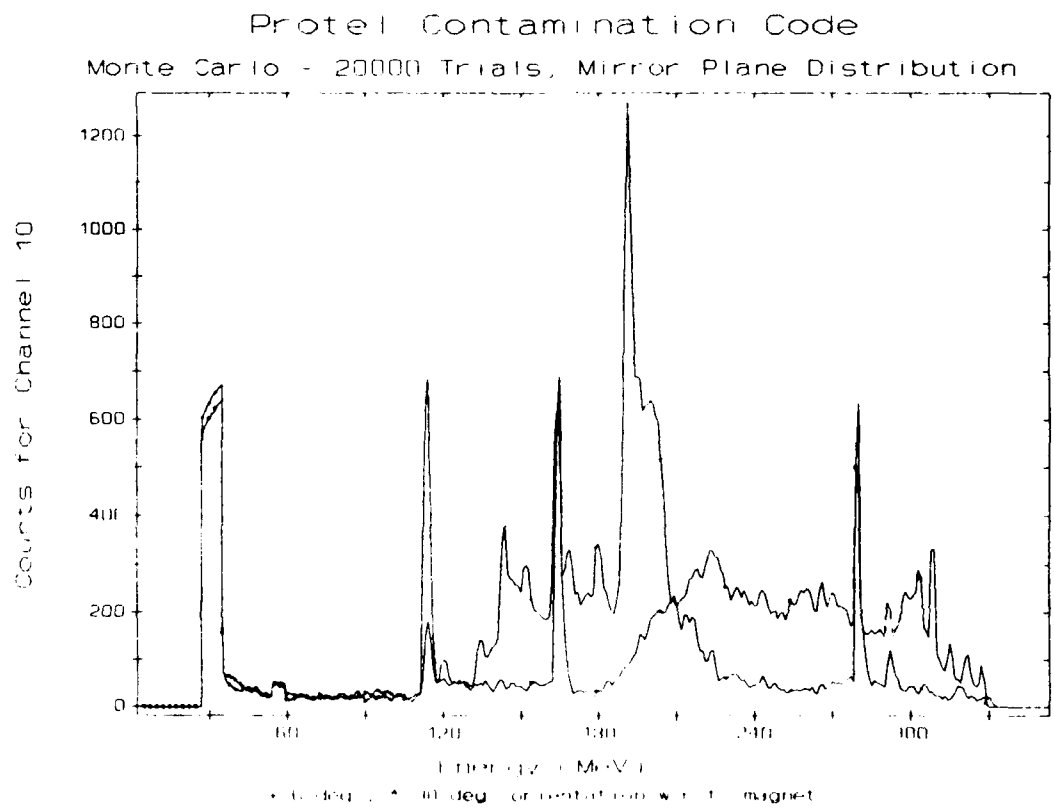


Figure 50. Response Function for Mirror Plane Case, for two orientations of the mirror plane with respect to the PROTEL electron deflection magnet.

4.1.3.2 Contamination Counts

Predictions from the Protel Contamination Code have been produced in tabular form, and also in graphical form and have been made available to researchers for use in the evaluation of the performance of the PROTEL HEH. In Table 5 the response function was used to compute the fraction of counts due to contamination for the PROTEL HEH head for power law spectra and an isotropic distribution. The results indicate that the contamination is severe for flat and relatively flat spectra.

Table 5

FRACTION OF PROTEL HEH COUNTS DUE TO CONTAMINATION

Isotropic Distribution

POWER LAW SPECTRUM E^q

CHAN	q = 0	-1	-2	-3	-4	-5	-6	-7	-8	-9	-10
1	.9889	.7414	.1358	.0482	.0355	.0289	.0241	.0203	.0172	.0147	.0125
2	.9751	.6176	.1057	.0385	.0263	.0198	.0154	.0121	.0095	.0076	.0060
3	.9534	.5284	.1672	.1174	.1035	.0949	.0882	.0826	.0778	.0736	.0697
4	.9513	.5189	.0982	.0365	.0231	.0164	.0122	.0093	.0071	.0056	.0044
5	.9686	.6816	.2003	.0891	.0685	.0603	.0560	.0539	.0533	.0537	.0550
6	.9651	.7011	.2839	.1722	.1459	.1327	.1233	.1157	.1093	.1037	.0987
7	.9646	.7099	.2448	.0954	.0623	.0484	.0394	.0329	.0278	.0237	.0203
8	.9752	.8121	.3666	.1191	.0604	.0416	.0320	.0260	.0220	.0194	.0178
9	.9705	.8183	.4487	.2143	.1427	.1156	.0999	.0884	.0793	.0718	.0654
10	.9775	.8722	.5502	.2312	.1085	.0677	.0488	.0370	.0287	.0224	.0177
11	.9691	.8539	.5671	.2970	.1771	.1299	.1061	.0907	.0793	.0702	.0628
12	.9792	.9085	.6966	.3901	.1955	.1142	.0786	.0590	.0460	.0365	.0293
13	.9729	.8991	.7126	.4566	.2738	.1829	.1383	.1128	.0956	.0827	.0725
14	.9816	.9356	.8095	.5843	.3608	.2243	.1556	.1191	.0968	.0811	.0692
15	.9838	.9493	.8583	.6791	.4535	.2761	.1733	.1186	.0879	.0687	.0555
16	.9851	.9598	.8993	.7769	.5904	.3917	.2401	.1464	.0930	.0623	.0439

4.2 Dosimeter

4.2.1 Motivation

This section describes the modeling of the CRRES dosimeters for the following angular distributions: the isotropic distribution, the mirror plane distribution and the $\sin^N \alpha$ pitch angle distribution. The mirror plane distribution is the limiting case in which charged particles (in this case, protons) trapped in the earth's magnetic field are at their "mirror points". The latter are the points at which the pitch angle (the angle between the magnetic field vector and the proton's velocity vector) is 90 degrees. The mirror points represent the northern or southern extremes of their motion relative to the geomagnetic field. The angular distribution of mirroring particles is uniform in the mirror plane, and is sometimes referred to as a "delta function" in the mirror plane. The software models for these angular distributions will be used as an aid to analyze the data produced by the CRRES Dosimeters, which, in turn, will be used to model the proton distribution in the radiation belts.

The design of the CRRES Dosimeters is based on the Space Radiation Dosimeters successfully used on the DMSP 7 satellite [Gussenhoven, et. al., 1986]. Modifications of the original DMSP design were made because of the different operational environment and the orbit of the CRRES satellite. A

description of the CRRES Dosimeters may be found in *Morel, et. al.* [1989]. An overall description of the CRRES Satellite and Experiments can be found in *Gussenhoven, et. al.* [1987]. Each of the CRRES Dosimeter detectors consists of a hemispherical aluminum housing, which is used to exclude charged particles with energies below a certain threshold limit. At the center of the hemispheric shell is a silicon disk-shaped particle detector which measures the energy deposited in its active region by high energy ions, and reports the counts and dose as follows: there are three ranges (channels) to which the instruments respond, viz, LOLET (energy depositions of 0.5 - 1 MeV), HILET (energy depositions of 1 - 10 MeV), and star events (energy depositions greater than 20 MeV). In this report, we will only be concerned with the LOLET and HILET channels, and with protons in the mirror plane particle distribution limit.

4.2.2 Methodology

The approach used to model the CRRES Dosimeters, in this study, is to compute the path length distribution, and use it to compute the counts and dose for a variety of mirror plane proton flux distributions. The path length distribution represents a "histogram" of the possible path lengths which a charged particle (proton), from the mirror plane distribution, can take through the detector, and is a function of the angle between the magnetic field vector and the normal to the top surface of the detector. If normalized to 1, the path length distribution represents the probability that a particle passing straight through the detector will have a given path length.

The path length distribution depends only on the detector geometry and on the angular particle distribution. Using code based upon the Janni Energy - Range tables, the path length distribution is used to compute the counts and dose which would be observed for a given proton energy spectrum.

4.2.2.1 Physical Assumptions

The CRRES Dosimeters are a set of four disk shaped silicon particle detectors, each of which is mounted at the center of a hemispheric aluminum shell. For simplicity in computation, only the active portion of the detectors is modeled. The hemispherical shell is used to set the lower energy limits of charged particles which will arrive at the detector. The physical and geometrical parameters of the detectors are presented in Table 6.

Table 6. Physical and Geometric Parameters of the CRRES Dosimeter Detectors				
Detector #	Detector Area [cm ²]	Detector Thickness [microns]	Thickness of Al Hemisphere [gm/cm ²]	Minimum Proton Energy Required to Penetrate Aluminum Hemisphere [MeV]
1	0.00815	403	0.55	20
2	0.051	434	1.55	35
3	0.051	399	3.05	51
4	1.000	406	5.91	75

A summary of the notation used in this report is provided in the following table:

Table 7. Notation		
Symbol	Description	Units
D	Thickness of Detector	microns
R	Radius of Detector	cm
λ	Angle between magnetic field lines and normal to detector surface	
γ	Angle in mirror plane (measured from the projection of the normal to detector surface onto the mirror plane)	
B	Magnetic Field Vector	
n	Unit vector normal to detector top surface	

The detector geometry for the mirror plane case is illustrated in Figure 51.

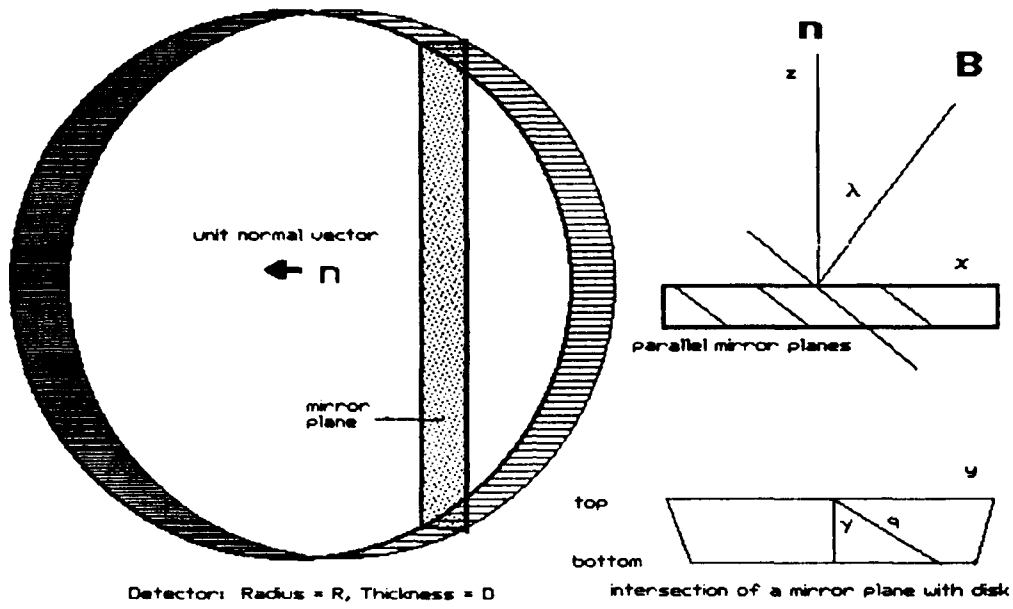


Figure 51. Detector Geometry

The mirror plane geometry is defined by λ , the angle between the magnetic field vector \mathbf{B} and the normal to the detector surface \mathbf{n} . Each plane perpendicular to \mathbf{B} is a mirror plane. For each point, either on the detector top surface, or within the volume of the detector, there is a single mirror plane upon which the point lies. In the coordinate system used here, the vector \mathbf{n} points towards the positive z -axis, and the x -axis lies in the plane defined by \mathbf{B} and \mathbf{n} . The y -axis is perpendicular to both \mathbf{B} and \mathbf{n} . The angle γ is defined as the angle in the mirror plane between the velocity vector and the projection of the vector $-\mathbf{n}$ onto the mirror plane.

4.2.2.2 Path Length Distribution Computations

The problem is, therefore, to determine the path length distribution, as a weighted sum, of the contributions from different directions as determined by the geometry of the detector and of the particle angular distribution. Monte Carlo methods were used to compute the path length distributions. A full Monte Carlo computation was numerically impractical, because it would require the selection of large numbers of points lying outside the detector, and would require a determination for each trial whether

the ray selected would actually penetrate the detector. It is, therefore, desirable to compute the contributions due to the following possible cases:

- (1) A proton enters the top of the detector, and exits the bottom or the side of the detector.
- (2) A proton enters the side of the detector, and exits through either the side or the bottom.

These Monte Carlo computations will be briefly described below for the Mirror Plane case.

Case 1.

The Monte Carlo program picks random points P on the top surface of the detector. In the mirror plane passing through P , a value of γ was selected randomly according to the proper probability distribution. A trial value of q was computed using the equation $q = D/\sin \lambda \cos \gamma$. The vector q from P , in the direction defined by λ and γ , was computed. If the resulting point $Q = (x', y', z')$ satisfied the condition $x'^2 + y'^2 \leq R^2$, then a counter, corresponding to an interval (bin) for the value of q (top-to-bottom), is incremented. Otherwise, the quadratic equation in q ,

$$(1 - \sin^2 \lambda \cos^2 \gamma) q^2 + 2(x \cos \gamma \cos \lambda + y \sin \gamma) q + (x^2 + y^2 - R^2) = 0 \quad (29)$$

which implements the conditions $x'^2 + y'^2 = R^2$, $0 \leq z' < D$, is solved, and the counter (top-to-side case), corresponding to q , is incremented.

Case 2.

For the Monte Carlo computation, points are randomly selected in the y - z plane, $-R < y < R$, $0 < z < D$; x was computed from the equation $x = -\sqrt{(R^2 - y^2)}$, and γ was computed from a uniform distribution on the interval $-\pi/2 \leq \gamma \leq \pi/2$. First, a trial value of q was computed using the equation $q = z / \sin \lambda \cos \gamma$. If $x'^2 + y'^2 \leq R^2$, then the side-bottom counter was incremented for the interval containing q . If the trial fails, then q is computed using the equation,

$$q = \frac{-2(x \cos \gamma \cos \lambda + y \sin \gamma)}{1 - \sin^2 \lambda \cos^2 \gamma} \quad (30)$$

and the side-side counter was incremented, provided that $z'' > 0$ and q was in the proper range.

To combine the Case 1 and Case 2 Monte Carlo results into a single path length distribution, it is necessary to determine the relative flux contributions entering from the top and from the side. As seen from the side, the area of the detector is $2 D R$. If we multiply the area by $\cos \lambda$, we obtain the projected area as seen from protons in the mirror plane incident on the detector. We wish to normalize the computation with respect to the top surface area of the detector, which is given by πR^2 . The Case 2 contribution is obtained from the normalized Case 2 distribution by multiplying the latter by $2 D \cos \lambda / \pi R$. Similarly, the projected area of the top surface as seen from protons entering the detector from the top must be multiplied by $\sin \lambda$. It is also necessary to take into account, that for any value of λ , there is always a contribution to the side-side component corresponding to $\gamma = \pm\pi/2$, while for $\lambda \approx 0$, the side to side contribution is present for each value of γ . Therefore, the total contribution is given by:

$$f(\lambda) = 2 D (1/\pi + \cos \lambda (1 - 1/\pi))/R S(\lambda) + \sin \lambda T(\lambda)$$

where S and T are the contributions from the side and from the top, respectively. The function $f(\lambda)$ will then represent the path length distribution (relative to unit area).

4.2.3 Results

The actual mirror plane path length distributions were computed for values of λ from 0 to 90 degrees at one degree intervals. Figures 52 and 53 represent the mirror plane path length distributions for detectors 1 and 4 for $\lambda = 60^\circ$. For comparison, the infinite slab mirror plane approximation path length distribution is also provided on the same graphs using the same normalization (area under the curve). Note the close agreement for Figure 53; for Figure 52 the differences are due to edge effects. The infinite slab path length distribution is zero until the minimum possible path length which occurs at $D/\sin \lambda$.

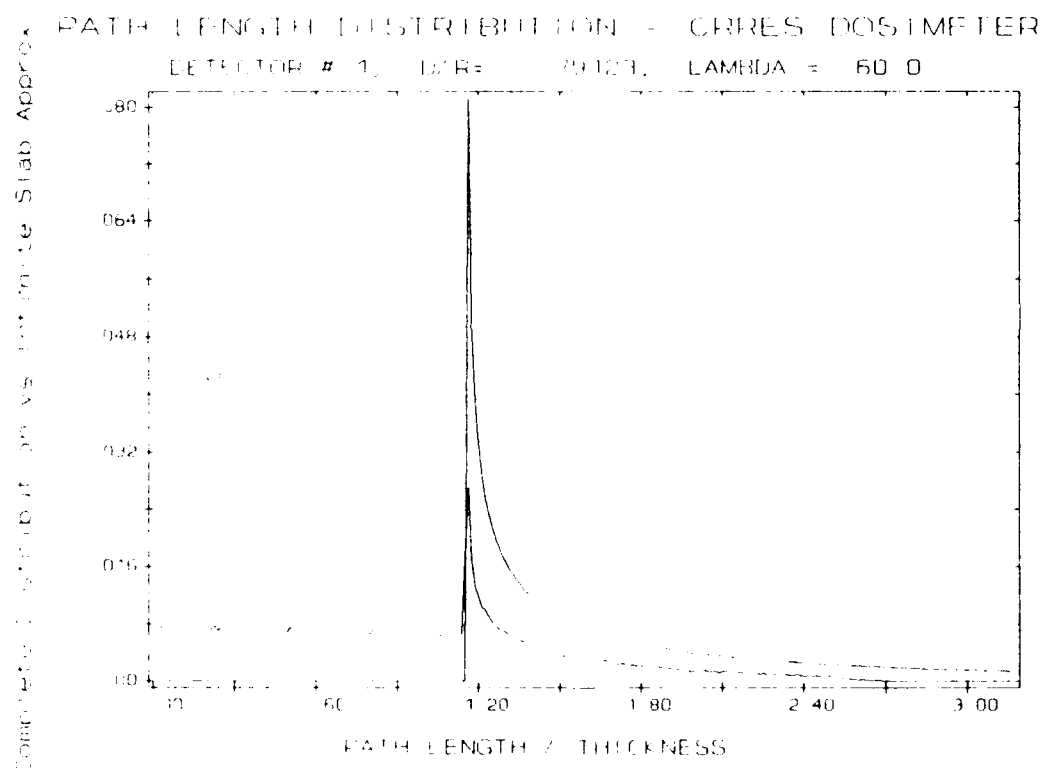


Figure 52. Path Length Distribution for Detector 1 for $\lambda = 60$ degrees compared with Infinite Slab Path Length Distribution (smooth curve).

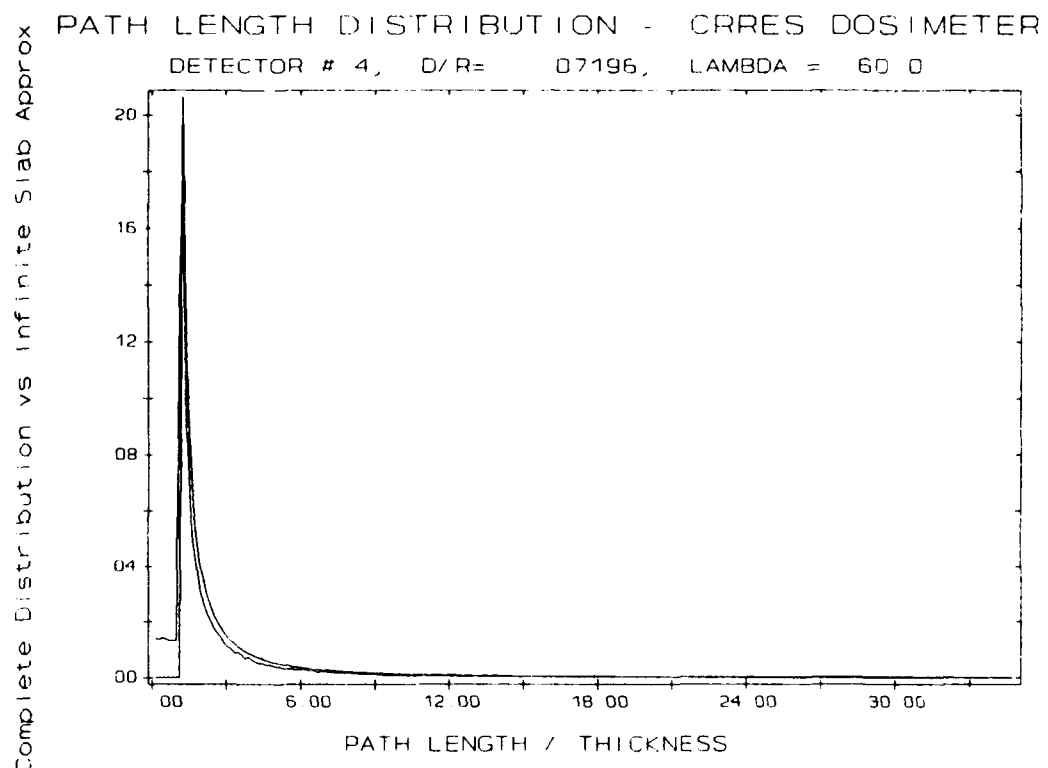


Figure 53. Path Length Distribution for Detector 4, $\lambda = 60$ degrees.

To compute the flux and dose response function, for each incident energy value, the energy loss is computed for each path length value, and the corresponding computed count and dose contribution is weighted by the normalized path length distribution value.

4.3 References

Gussenhoven, M. S., Mullen, E. G., Filz, R. C., Hanser, F. A., Lynch, K. A., "Space Radiation Dosimeter SSJ* for the Block 5D/Flight 7 DMSP Satellite: Calibration and Data Presentation", AFGL-TR-86-0065, 1986, ADA172178.

Gussenhoven, M. S., Mullen, E. G., Sagalyn, R. C. (editors), "CRRES/SPACERAD Experiment Descriptions", AFGL-TR-85-0017, 1987, ADA160504.

Hein, C. A., Private Communication, Feb. 1990.

Janni, J., "Proton Range Energy Tables, 1 KeV - 10 GeV in: Atomic Data and Nuclear Data Tables", Vol. 27, Pp. 147-529, Academic Press, New York, 1982.

Lynch, K., Boughan, E., Fischi, D., Hardy, D., Riehl, K., "PROTEL: Design, Fabrication, Calibration, Testing and Satellite Integration of a Proton Telescope", AFGL-TR-89-0045, Environmental Papers, No. 337, 1989, ADA214564.

Morel, P. R., et. al., "Fabricate, Calibrate and Test a Dosimeter for Integration into the CRRES Satellite", GL-TR-89-0152, April 1989, ADA213812.

Redus, R., Filz, R., Swider, W., Violet, M., Private Communication, 1990.